DEVELOPMENT OF TISSUE BASED BIOMATERIALS FOR ARTICULAR CARTILAGE INJURIES

A Dissertation Presented to the

Faculty of the Graduate School

at the University of Missouri

In Partial Fulfillment

of the Requirements for the

Degree Doctor of Philosophy

---

by

COLTEN L. SNIDER

Dr. Sheila A. Grant, Dissertation Supervisor

December 2020

The undersigned, appointed by the Dean of the Graduate School, have examined the dissertation entitled

DEVELOPMENT OF TISSUE BASED BIOMATERIALS FOR ARTICULAR CARTILAGE INJURIES

Presented by Colten L. Snider
A candidate for the degree of Doctor of Philosophy
And hereby certify that in their opinion it is worthy of acceptance.

_____
Dr. Sheila Grant
Department of Biomedical, Biological, and Chemical Engineering

_____
Dr. Raghuraman Kannan
Department of Radiology

_____
Dr. Ferris Pfeiffer
Department of Biomedical, Biological, and Chemical Engineering

_____
Dr. Adam Schrum
Department of Molecular Microbiology and Immunology

DEDICATIONS

I would like to dedicate this dissertation to my family. Without your unwavering support throughout my life's journey thus far, I would not be in this position today.

ACKNOWLEDGMENTS

I am forever indebted to Dr. Sheila Grant for her inviting me to learn as an undergraduate in her lab and for her encouragement to pursue a graduate school. All of her support in my work and her mentorship has been an invaluable asset in my life. I would also like to thank all of my committee members for their insight and input into my work.

I would like to thank all of my colleagues in the lab. Dave Grant has also been an excellent mentor not only in pursuit of research but also in the pursuit of life and a career. Sarah Smith helped me grow as an undergraduate researcher allowing me to get experience with her projects. Janae Bradley, Chris Glover, Hilary Schmidt, Lauren Parr, and Aaron Wood all made my introduction into graduate school a smooth transition creating a fun and positive atmosphere to work in. Mitch Bellrichard, I don't know what I'm going to do without all of the world's knowledge only a desk away. I also really appreciate the opportunity that Brian Buntaine and Charlie Hanford afforded me working with them in technology transfer at the university.

I would like to thank my funding sources including the Coulter Translational Partnership Program at the University of Missouri, Food for the Twenty-First Century Grant, and MU Department of Bioengineering.

Finally, I would like to thank all my family members for always being an encouraging and supportive light. I wouldn't have such peace in my life without them. To my parents, Greg Snider and Denise Hancock, their drive and commitment to not only being the best parents but also their drive and commitment to quality in the pursuit of career and life are only but a few core values I have adopted in my journey.

Table of Contents

LIST OF FIGURES

Figure

LIST OF TABLES

Table

DEVELOPMENT OF TISSUE BASED BIOMATERIALS FOR ARTICULAR CARTILAGE INJURIES

Colten L. Snider

Dr. Sheila Grant, Dissertation Supervisor

ABSTRACT

Multiple biomaterials have been developed in this work. Decellularized porcine diaphragm extracellular matrix was homogenized and supplemented with various biomodulatory agents. It was developed as an injectable material with possible applications in mitigation of posttraumatic osteoarthritis (PTOA). Optimizing polycaprolactone and lecithin electrospun nanofibers for increased reproducibility was studied. A neutral pH liquid porcine collagen type I solution was developed for two separate projects including development of collagen microspheres (CMs) and 3D printed scaffolds. The main focus of this dissertation is on the development of CMs. The CMs were fabricated by emulsifying the liquid collagen solution in a water-in-oil emulsion. Characterization of the CMs through electron microscopy, Fourier transform infrared spectroscopy analysis, differential scanning calorimetry, and biocompatibility analysis were conducted. The CMs were then investigated as a potential targeted PTOA mitigating agents by conjugating targeting antibodies on CMs to bind to damaged articular cartilage. CMs were also laden with mesenchymal stem cell and studied in culture over 2 weeks. The targeted CMs successfully bound to damaged cartilage and were able to mitigate reactive oxygen species production from interleukin-1beta

stimulated human chondrocyte cells with addition of anti-inflammatory agent, curcumin. Finally, use of the developed liquid collagen as a potential bioink for 3D printing was investigated.

Chapter One

LITERATURE REVIEW

1.1 PTOA effects on articular cartilage

Osteoarthritis (OA) is a joint degenerative disease affecting the entire joint structure wherein disorder occurs in the articular cartilage, calcified cartilage, subchondral cortical and trabecular bone, joint capsular tissues, and synovium [1]. Over time, bone-on-bone articulation arises, which can be debilitating to people who suffer from this disease hampering everyday activities. The articular cartilage is a specialized extracellular matrix mainly composed of type II collagen, helping to aid articulation and ease regular impacts imposed on the joint [2]. Articulation is eased through a boundary layer of lubricin found at the interface of the synovial fluid and articular cartilage surface [3, 4]. Impacts imposed on the joint are eased through the meshwork of the ECM with a composition of many large and small proteoglycans along with aggrecan [5, 6]. OA progression over time can be difficult to determine with factors like age, sex, genetics, ethnicity, activity level, trauma, and alignment [7]. Post-traumatic OA (PTOA) is a joint degenerative disease that arises from joint trauma leading to the same outcome of OA [8].

1.1.1 Structure of the articular cartilage

For the relative thickness of the articular cartilage, ~2-4 mm, it is a quite complex structure composed of multiple different regions [2]. Articular cartilage's

main purpose is to aid and ease the articulation of joints and to help transmit forces imposed with a low coefficient of friction. The extracellular matrix (ECM) of the articular cartilage is composed of multiple collagens and proteoglycans. Approximately 60% of the articular cartilage, dry weight, is comprised of collagen with 90-95% of the collagen being type II collagen [9, 10]. Other collagens found in the articular cartilage being I, IV, V, VI, IX, and XI [2, 11]. Other non-collagenous proteins and molecules found in the articular cartilage include aggrecan, hyaluronic acid, decorin, biglycan, fibromodulin, fibronectin, laminin, and multiple integrins [2]. It is an avascular tissue with specialized cells found throughout called chondrocytes.

Chondrocytes receive most of their nutrition through synovial fluid filling the space in the joint, which hydrates the cartilage. Recent work by Bergholt et al. suggests 6 different zonal regions composing the articular cartilage with two individual mineralized zones underneath [12]. Zone 1 correlates to the articular surface while zone 6 integrating with the mineralized bone. The relative orientation of the collagen within the articular cartilage changes from the articular surface to the subchondral bone. Collagen fibers run parallel to the surface just below the interface in zone 1 and 2. These zones help protect the underlying layers and are also a major contributor to the tensile properties of the tissue which help to resist shear, tensile, and compressive forces generated through articulation [2]. Zones 3 – 5 is the region of articular cartilage responsible for absorbing compressive forces with thicker collagen fibers found in this region compared to zones 1 and 2. In this region, collagen begins to transition from a

parallel organization relative to the articular cartilage surface in zone 3 to an oblique angle in the middle to lower region of zone 3 transitioning into zone 4, and a perpendicular organization in zone 5. Chondrocytes also transition from a spherical orientation to a columnar orientation in this region. Zone 6 is also responsible for absorbing compressive forces. It is the last region of protection before mineralized bone. This region has the highest resistance to compression as the largest collagen fiber diameters are found here [2]. Chondrocyte cells have a flat morphology along the surface of the articular cartilage. As the chondrocytes go deeper into the cartilage they begin to take on a more columnar morphology. This is associate with the forces applied to the cartilage. Sheer, tensile, and compressive forces are all alleviated by having cellular and collagen orientation parallel to the surface. Zone 1 has a high glycosaminoglycan (GAG) and water content with a low collagen content with collagen content increasing the further into the cartilage with the highest content in zone 5 along with the most vertical orientation of collagen in this region too. Zone 4 and zone 6 have almost identical footprints in terms of collagen, GAG, and water content.

1.1.2 Incidence of PTOA

Symptomatic OA is defined as pain, aching, stiffness, and disability in a joint along with radiographic evident OA through the use of magnetic resonance imaging or other imaging devices [13]. About 27 million people in the United States aged 25 or older have a clinical diagnosis of OA [14]. PTOA is largely a lower extremity issue with most PTOA occurring in the ankle, knee, and hip [15].

Approximately 12% of all symptomatic OA are PTOA cases [15, 16]. Direct costs of treating PTOA are estimated to exceed $3 billion annually, and 10% of all cases of knee OA arise from a PTOA event [15, 16]. People who injure their meniscus and/or their anterior cruciate ligament (ACL) commonly develop PTOA as well. It is estimated that 13% of isolated ACL injuries and up to 48% with ACL and meniscal injuries develop PTOA [15, 17]. In cases of ankle OA, studies have suggested up to 78% are PTOA related [15, 16, 18, 19]. PTOA of the hip accounts for 2% of all OA cases. Within the military population, the number of hip PTOA cases increases to 20% [20].

1.1.3 Biochemical Progression of PTOA

A mechanical impact or load on the articular cartilage is the most common impetus for the progression of PTOA. Cells in the underlying ECM that are in the direct line of impact will immediately necrose [21]. Not only is there cell necrosis but also a release of fibronectin and alarmins, which signal intracellular pathways that activate and synthesize procatabolic and proinflammatory mediators [22-25]. Common alarmins released after an impact include nucleic acids, high mobility group box 1(HMGB1) protein, and S100A8/9 which are all termed damage-associated molecular patterns (DAMP) [25, 26]. These DAMPs will bind to various receptors like toll-like receptors 2 and 4 (TLR2/4) and receptors for advanced glycation end products (RAGE), which mainly activates signaling cascades like nuclear factor-kappa B (NF-kB) and to a lesser extent mitogen-activated protein kinases (MAPK) pathways [27-30]. The downstream products of

these pathways include multiple MMPs, ROS, NO, collagenase with selectivity towards type II collagen, and the release of other interleukins and cytokines from surrounding cells [24, 26, 29-31]. Specifically, the cascade of the NF-kβ signaling pathway leads to detrimental effects on the articular environment. This pathway leads to the secretion of metalloproteinases (MMP)-1, -2, -3, -7, -8, -9, -13, and -14 and a disintegrin and metalloproteinase with thrombospondin motifs (ADAMTS)-1, -3, -4 and -5 which results in cartilage breakdown [32-34]. Catabolic chondrocytes begin to express cytokines and chemokines like tumor necrosis factor (TNF)-α, interleukin (IL)-1β, IL-6, IL-8, and receptor activator of NF-kβ ligand (RANKL), which perpetuates and enhances articular damage [32, 35, 36]. This pro-catabolic response contributes to chondrocyte apoptosis, articular cartilage degradation, and instability in the joint. This prolonged effect leads to apoptosis of cells, not only in the region surrounding the impact but eventually through the entire tissue and causes loss of ECM [37, 38].

ROS and NO begin to accumulate after mechanical impact and both are known to drive chondrocyte cells into an enhanced metabolic state [39-41]. With chondrocytes already synthesizing procatabolic and proinflammatory products, the enhanced metabolic activity leads to further cartilage degradation. ROS has been shown to enhance activation of procatabolic pathways like nuclear factor-kB (NF-kB), and mitogen-activated protein kinases (MAPK) like extracellular signal-regulated kinase 1/2 (Erk 1/2), p38 cascade, and c-Jun N-terminal kinases (JNK) [21, 42, 43].

After mechanical stress has been imposed on the articular cartilage, chondrocytes surrounding the impact site may not immediately necrose but their homeostatic regulation is altered. These chondrocytes will release a multitude of procatabolic factors. Two major procatabolic factors include interleukin-1β (IL-1β) and TNF-α which activate the NF-kB pathway [21, 44]. Both IL-1β and TNF-α have been identified as stimulators of HMGB-1 release from chondrocyte cells in osteoarthritic articular cartilage [45]. IL-1β is more closely linked with cartilage destruction while TNF-α has been linked to the perpetuation of the inflammatory cascade [46, 47]. Not only do these two proinflammatory mediators lead to induction of the NF-kB signaling pathway but they also act as a positive feedback loop to perpetuate the release of more procatabolic factors [46]. IL-1β receptor and IL-1 receptor type 1 found on the surface of chondrocytes increase after chondrocytes have reached a dysregulated state [48, 49]. Likewise, TNF-α receptors and TNF receptor 1 are also increased on the surface of dysregulated cells [50]. Studies have shown that the expression of collagen type II, aggrecan, and proteoglycans are all suppressed by IL-1β [51-54]. TNF-α has also been shown to suppress the synthesis of proteoglycans and collagen type II [55, 56]. Other work has also shown a synergistic effect of the presence of both IL-1β and TNF-α. Henderson et al showed that a dual injection of both IL-1β and TNF-α created more cartilage degradation rather than an individual injection of either factor [57].

1.1.4 Current Treatment Techniques

Current repair techniques can vary between various joint locations. This review is intended to focus on treatments for the knee. While currently there are no definitive techniques to treat the development and progression of PTOA, some palliative approaches are utilized for mitigating pain, improving function, improving range of motion, and slowing progression. Diagnosable, symptomatic PTOA may present in less than a year but can take up to 10-20 years to present signs and symptoms [58]. An advantage of PTOA as compared to traditional OA is that a defined traumatic event initiates progression. Proactive management of the injury can begin immediately if a person seeks treatment after the traumatic event. Proactivity utilizing various management techniques can slow the progression of PTOA, which may reduce the likelihood and need for more invasive measures. Physical therapy, medications, surgery, and alternative strategies are all utilized in the management of PTOA. Generally, treatments begin with non-invasive techniques to slow PTOA's progression but usually invasive surgeries are utilized after all avenues in management have been explored.

Physical therapy is typically the first line of treatment to manage the pain associated with the injury. The primary goals of physical therapy are to reduce short- and long-term symptoms, improve mobility/function, help stabilize the joint, and reduce the need for medications [59, 60]. An exercise regimen is designed around these main foci, which match with the patient's exercise ability. An exercise program including a variety of aerobic, resistance, and balance based

exercises are generally adopted in combination [61]. Physical modalities can also be used in conjunction with exercise therapies. Thermotherapy can be utilized to heat or cool the affected area after the treatment program to improve pain, walking tolerance, and improve physical function [62]. Therapeutic ultrasound is used to heat deep tissues by transmitted sound waves in a pulsed manner to improve pain and function [63]. Transcutaneous electrical nerve stimulation, interferential current, neuromuscular electrical stimulation, and electromagnetic field treatment are all options to reduce pain and improve the function of the joint [64].

Oral or topical nonsteroidal anti-inflammatory drugs (NSAIDs) are often taken in conjunction during physical therapy. Common first-line pharmacologic agents include acetaminophen, selective and nonselective cyclooxygenase-2 (COX-2) inhibitors, ibuprofen, diclofenac, naproxen, celecoxib, and diclofenac, which have been shown to reduce pain and improve the function of the joint [65, 66]. If patients have an inadequate response to pain relief with the first-line treatments of physical therapy and pharmacological agents, more advanced pharmacologic treatments like tramadol or duloxetine are prescribed [66].

The next phase of treatment includes direct injection of therapeutic agents into the intra-articular space. Injections are usually performed with a lateral and medial mid patellar approach. This measure can also be used before the prescription of more advanced pharmacologic agents. Corticosteroids are typically injected to treat joint inflammation, effusion, and pain. Injections of corticosteroids are not recommended more than once every three months [67].

These injections also do not provide long term relief and require an iterative approach to maintain their benefit [67]. From 2007 to 2015 the use of physical therapy as a primary treatment of osteoarthritis reduced in favor of injection therapies like glucocorticoids [68]. Dhawan et al. noted that four times more patients received glucocorticoid injections over physical therapy before having total knee replacement surgery [69]. Deyle et al concluded that patients who performed physical therapy with an osteoarthritis diagnosis had less pain and functional disability at 1 year as compared to patients who had a glucocorticoid injection [59].

Depending upon how much the damage to the articular cartilage has manifested, hyaluronic acid (HA) injections may be a possibility. HA is found in synovial fluid and is a high molecular weight glucosamine derived from synoviocytes, fibroblasts, and chondrocytes [70]. HA increases the lubricity of the joint and demonstrates pain reliving ability [71]. Contention on the use of HA has been debated for many years with a mixed consensus due to its efficacy relative to other options [72].

Platelet-rich plasma (PRP) injections are also utilized. PRP is an autologous treatment derived from the patient which includes potentially useful growth factors. There is evidence that PRP may help with pain and function [70]. The addition of leukocytes with PRP appears to also improve pain and function [73].

Surgical intervention is the last case scenario for treatment of PTOA. If all previous treatment modalities are unable to mitigate pain and improve function of

the joint, surgery will be performed. Generally, arthroscopic procedures are attempted first followed by invasive surgery.

Osteochondral autograft transfer is an option to treat small defects of approximately less than 2 cm^2 [74, 75]. In this procedure, non-weight bearing portions of the articular cartilage are harvested and used to fill the damaged region of the articular cartilage. It has been noted that difficulty in this procedure arrises mostly from matching the thickness of the damaged region with the harvested cartilage to create a smooth articulating surface [76, 77]. There are conflicting reports of the outcomes of this procedure. Three publications found statistically improved scoring metrics by patients in follow-ups at 19.3, 28.7, and 24 months respectively [78-80]. One publication by Bently et al. found high failure rates with a 1.7-year follow-up [81].

Osteochondral allograft transplantation is also used. In this scenario, donor tissue is harvested and used to fill the damaged region of the articular cartilage. This may be particularly useful for patients who are not good candidates for removal of healthy articular cartilage or increased trauma associated with an autograft. Again mixed reports of efficacy have been published. One publication reported reoperation rates as high as 86% [82].

Autologous chondrocyte implantation is another option. This technique requires two procedures. The first procedure requires a biopsy of the articular cartilage to harvest the patient's chondrocyte cells. The cells are then cultured. After the cells have been cultured a second procedure is carried out to fill the

defect with the cultured chondrocyte cells and then sealed with a periosteal graft [83].

Patients who are younger and more active will usually have a procedure to debride the damaged area to smooth the articulating surface and to regain articulation and ease the pain. With debridement, damage to the articular cartilage is relatively minimal with lesions less than 15 mm in diameter [84]. Microfracture is also often associated with debridement of articular cartilage. Microfracture is a method of creating small osteochondral lesions in the debridement region to stimulate the development of fibrocartilage from the underlying subchondral bone. This ultimately leaves tissue integrated with the articular cartilage but allows for smoother articulation and protection of the cartilage but may not be as resistant to degradation relative to native articular cartilage [85].

If a more severe case of PTOA has occurred in a patient, such as a misalignment of the knee joint, then an osteotomy may need to be performed. This procedure will salvage as much of the native tissue as possible and reshape the surface of either the tibial or femoral head to improve articulation of the joint.

Finally, if the other procedures have been exhausted, a joint replacement is required. A unicompartmental knee arthroplasty (UKA) or total knee arthroplasty (TKA) can be performed to replace the joint. A UKA is commonly used for patients with either tibial or femoral PTOA. Patients younger than 65 generally have an increased risk of revision of UKA due to progression of PTOA to the opposing compartment, resulting in loosening of components, instability, or

dislocation [86]. TKA is a recommended procedure for patients with end-stage multicompartment PTOA. Usually, TKA is a last resort for patients younger than 65 and who can no longer manage pain from PTOA**.**

1.2 Biomaterials

Biomaterials are a genre of developed materials intended for use within the body in support of a lacking facet in a biological system. The material typically supports the lacking biologic system either by aiding/reducing time to recovery or fully replacing the system. An example of a material aiding recovery would be biodegradable sutures closing an open wound, whereas a total knee replacement is a material replacing the traditional biologic system. Biomaterials can be classified as either synthetic or natural materials. Examples of synthetic materials include polymer-based materials such as polypropylene and expanded polytetrafluoroethylene used in hernia meshes. Examples of natural materials include auto-, allo-, or xenografts, which have been utilized for use in anterior cruciate ligament (ACL) reconstruction. Traditionally natural biomaterials have a reduced inflammatory host response [87]. Other natural biomaterials can be derived from full tissues like diaphragm, bone, dermis, endometrium, or in the building blocks of full tissues like collagens, fibrin, elastin, hyaluronan or even found in other species like chitosan, silk, agarose, or alginate [88]. With collagen being the most commonly found protein in the body, it serves as an excellent material due to its interaction with almost every biological system [89].

1.2.1 Biocompatibility

Biocompatibility is the core tenant of developing a material to be implanted within the body. D.F.Williams points out that first-generation materials were chosen on the basis that they were non-toxic, non-immunogenic, non-thrombogenic, non-carcinogenic, and non-irritant [90]. Essentially the material was more or less inert within the body creating a minimal host response. But that was soon to be recognized as a non-standing theory as factors like reactions of the same materials interacting differently in separate locations of the body, recognition of advantages by inciting specific reactions to particular tissues, and materials that can degrade over time may also be advantageous in certain situations like biodegradable sutures. Since the initial concept of biocompatibility, many biologic phenomena have been identified that factor into what makes a material biocompatible. Immediately after integrating a biomaterial with tissue, a host immune response is triggered. Current research supports the idea that it is more important to have the biomaterial actively engaging the biologic environment than for the biomaterial to remain inert [91]. Having the material designed to actively engage with its environment allows the direction of the host-response at the implanted site which can improve recovery time, integration of the material with the surrounding environment, and reduce the opportunity for chronic inflammation and foreign body reactions. There are different techniques in which to direct the host response. Surface modifications, incorporation of bioactive materials, and emulation of biomaterials to their implanted site are all techniques in which biomaterials have been designed to direct the host response [91]. This

is especially valuable and notable in tissue-engineered scaffolds. Natural materials typically elicit a less severe host response due to acceptance of the natural materials relative to synthetic materials [87]. Usually, tissue-engineered scaffolds are designed to integrate the native tissue within the scaffold. This will eventually lead to a degradation of the scaffold material with a concurrent replacement with native tissue. Therefore a modern perspective of biocompatibility is defined as a biomaterial that is implanted within the body to improve a biological element without deleterious effects by either acting in an inert fashion or acting in such a way to stimulate a reparative response from the body to support or improve the element. However, biocompatibility does not serve as a singular event. Biocompatibility is a continuous journey beginning with *in vitro* work that progresses *in vivo* and eventually leading to clinical trials. Biocompatibility has to be maintained throughout this process.

1.2.2 Collagen

Collagen is the most commonly found protein in the body and is used in a wide range of biological systems like bone, cartilage, connective tissues, organs, and skin [89]. There are at least 28 types of collagen all with different applications [92]. They can be subdivided into two major categories, fibrillar and non-fibrillar. Type I collagen composes 80% of all collagens in the body. Type I collagen is also fibrillar collagen composed of three polypeptide chains two of which are α1 subunits and one α2 subunit [93]. The subunits have a characteristic X-Y-Glycine repeating sequence with X and Y usually correlating to

proline [94]. Post-translationally, the proline residue in the Y position is modified to hydroxyproline [95]. Hydrogen bonding is involved in the assembly and stabilization of the two α1 and one α2 subunits forming the triple helix, collagen microfibril. Specifically, hydrogen bonding is formed by N-H groups from the glycine which act as donors while the C=O groups of the residue in the X position acts as the acceptors, N─H···O═C [95-97]. Water mediated hydrogen bonding is also involved in the process of stabilization. Collagen fibril formation occurs from the aggregation of microfibrils into an oriented, periodic structure. Crosslinks form the basis for stabilization of the collagen fibrils[98]. Crosslinks occur between microfibrils through lysine and hydroxylysine residues. For human type I collagen, work has shown there to be 38 lysine residues in α1 subunits and 31 in α2 subunits [99]. In this process lysyl oxidase deaminates lysine and hydroxylysine residues forming aldehydic forms of lysine and hydroxylysine. There have been quite a few pathways identified forming these crosslinks but one of the most well-studied was first observed by Fujimoto [100]. Generally, aldehyde groups react with the ε-amino group from lysine and hydroxylysine to form crosslinks [99, 101].

1.2.2.1 Collagen Microspheres

Collagen microspheres (CMs) are a specifically manufactured biomaterial derived from collagen and shaped into a spherical form. CMs are generally on the order of a few microns to a few hundred microns. A few different techniques have been developed to manufacture CMs. The most common techniques to

manufacture CMs are by micropipetting and emulsion. In the micropipetting technique, collagen is pipetted onto a parafilm lined Petri dish and placed in a 37°C environment until the collagen has gelated [102, 103]. This technique is not without its limitations. Creating a large cohort of CMs can be difficult as it requires multiple pipetting cycles to produce CMs, which can be time consuming and laborious. Also, CMs produced with this method are large with CM diameters ranging from 300 μm to 1,000 μm. This leaves no flexibility in size manipulation below 300 μm. If injectability is the intent of manufacturing CMs then the micropipetting technique is not a viable method. The other alternative to micropipetting is an emulsion. An emulsion is a method of manufacturing CMs by immersing collagen into an oil-based solution and adding a high shear rate. This shear force creates individual droplets of collagen within the oil solution. Gelation of collagen through heating or chemical crosslinking is usually used to crosslink the individual collagen droplets to form a CM. A drawback of manufacturing CMs by emulsion is its high shear rate. If CMs are intended to be loaded with cells for specific applications the micropipetting technique may be favored over emulsion due to the much more delicate nature of manufacturing through micropipetting.

Chan et al. originally reported the method of micropipetting CMs. In their work, they encapsulated human mesenchymal stem cells (MSCs) within CMs and were able to show maintenance of an hMSC phenotype while hMSCs were encapsulated [104]. They also observed the development of vasculature two days after hMSC-CMs were subcutaneously implanted into NOD/SCID mice [104]. Other works with micropipetted CMs include development for damaged

articular cartilage and nucleus pulposus [102, 103, 105]. One such study by Cheng et al. was able to develop zonal regions of articular cartilage through the stacking of osteogenic and chondrogenic CM subunits to reproduce a chondrogenic layer, calcified cartilage zone, and an underlying osteogenic layer over 5 weeks with rabbit MSCs [105].

As mentioned previously, CMs manufactured through emulsion can be on the order of tens of microns. This makes them more applicable for injection therapies. Some work with emulsion reports the use of chemical crosslinking to form stable CMs. Some of the reported chemical crosslinkers include EDC/NHS, WSC, HMIDC, and glutaraldehyde [106-110]. Other work has described the use of no chemical crosslinkers [111-113]. Loading of CMs with bioactive agents to elicit a particular biologic response is an important factor in aiding the recovery of a lacking biologic system. Mathieu et al. reports the addition of TGF-B3 to CMs [113]. In this work, MSCs were added to the TGF-B3 loaded CMs and observed adherence of the MSCs to the CMs. MSCs chondrogenically differentiated and the MSC-CM clusters formed a tissue resembling cartilage with collagen II and aggrecan expression although cells became hypertrophic and calcification became an issue with the clusters. Mumcuoglu et al. also reports BMP-2 loaded CMs tuned for long-term release as a possible hard tissue regeneration tool [110].

1.2.2.2 3D Printing Collagen

While the use of collagen-based ink for 3D printing is a relatively young discipline, the advantages are very clear. Using a tissue-based material like collagen, the most prominent structural protein in the body, to print constructs allows the construction of more personalized materials that are specific to an individual patient's needs. Many factors of printing with tissue ink like diameter, stiffness, and porosity can be tuned to affected tissue sites to promote quicker integration times of native tissue. Cells can also be integrated within the collagen matrix to provide a personalized, living tissue. Materials printed with cells integrated within the printed matrix are termed bioinks. However, the printing of collagen-based tissues is not trivial. Methods of modifying either the collagen solution or the solution the collagen is printed into have been investigated to improve printing reproducibility, resolution, and fidelity.

Many different collagen-based inks have been prepared for printing. With collagen inks, there are a few different methods to either fibrilize or crosslink the printed tissue to form a rigid structure. With most collagen inks today, they are prepared in such a way that when introduced into a new solution that has an increased temperature or pH it triggers fibrilization of the collagen, which forms the structure [114]. Preparation of these collagen inks can involve the neutralization of collagen with pH neutral solutions like cellular media or phosphate-buffered saline. Other works that crosslink collagen inks include chemical crosslinkers, such as genipin, thrombin used in collagen/fibrin inks, calcium chloride used in collagen/alginate inks, and ultraviolet light [115-118]. Of

the collagen inks, additives can be introduced to direct specific events when the scaffold is applied to the targeted site. One such study by Kim et al studied the use of a collagen type I and tricalcium phosphate ink loaded with human adipose-derived stem cells (hASCs) [115]. They were able to demonstrate differentiation of the hASCs through the osteogenic lineage in situ leading to potential applications in bone tissue regeneration.

Others have investigated the use of different solutions to print collagen inks into, these are called “printing baths.” Printing into water alone can be challenging due to the inherent unpredictability of collagen through reproducibility, resolution, and fidelity. The use of thermoreversible support baths are of particular interest due to the difficulty in printing collagen directly into a fluid like water or cellular media. Initial work by Hinton et al in 2015 developed freeform reversible embedding of suspended hydrogels (FRESH) thermoreversible support bath solution. The solution is composed of gelatin microparticles [119]. By printing into a solution of gelatin microparticles this allows the bath to act as a rigid material at low shear stresses and act as a fluid at high shear stresses. At the extrusion site of the needle tip, the collagen ink is injected into the bath and held stable whereas the needle tip easily moves through the bath solution to create the printed material. Senior et al also developed suspended layer additive manufacturing (SLAM) [120]. This technique is similar to the FRESH support bath solution but agarose microparticles compose the bath solution rather than gelatin. These solutions are not without their drawbacks. To remove the printed material from the FRESH solution the

whole solution has to be heated to the liquid transition temperature of gelatin and then undergo washing to remove gelatin from the scaffold. While this is a relatively easy process as the transition temperature is around 37°C and at 37°C, this will not negatively impact a collagen-based material, remnant gelatin is a large concern with the FRESH process. The agarose transition temperature is much higher at around 90°C so melting the agarose is not an option since at 90°C collagen-based materials will denature at such temperatures. Therefore washing the collagen materials is the only option to remove the agarose from the scaffold. Remnant agarose is much more of a concern with the SLAM technique relative to using the FRESH technique.

The core of developing a collagen ink material is in its ability to be utilized in specific applications. Many different applications of collagen bioinks have been utilized today. Cartilage, skin, bone, cornea, heart valve, and neuron regeneration have all been investigated as possible avenues for collagen printed bioink scaffolds. Of course, each application will utilize cells specific to that region's native cell type like the integration of chondrocyte cells for cartilaginous printed scaffolds. One of the more unique applications of collagen ink being 3D printed is Lee et al [121]. Their work used FRESH printing of collagen ink focused on the reproduction of a functional heart. They were able to achieve a functional scaled ventricle model with synchronized contractions along with a functional tri-leaflet heart valve and reproduction of an anatomically scaled heart using CT imaging.

1.3 Conclusions

This work describes the fabrication of multiple biomaterial scaffolds utilizing extracellular matrix, polycaprolactone, and type I collagen with potential uses for orthopedic applications.

1.4 References

1. Goldring, M.B. and S.R. Goldring, *Articular cartilage and subchondral bone in the pathogenesis of osteoarthritis.* Annals of the New York Academy of Sciences, 2010. **1192**(1): p. 230-237.

2. Sophia Fox, A.J., A. Bedi, and S.A. Rodeo, *The Basic Science of Articular Cartilage: Structure, Composition, and Function.* Sports Health, 2009. **1**(6): p. 461-468.

3. Jones, A.R., et al., *Binding and localization of recombinant lubricin to articular cartilage surfaces.* Journal of orthopaedic research, 2007. **25**(3): p. 283-292.

4. Gleghorn, J.P., et al., *Boundary mode lubrication of articular cartilage by recombinant human lubricin.* Journal of Orthopaedic Research, 2009. **27**(6): p. 771-777.

5. Lu, X. and V. Mow, *Biomechanics of articular cartilage and determination of material properties.* Medicine+ Science in Sports+ Exercise, 2008. **40**(2): p. 193.

6. Laasanen, M., et al., *Biomechanical properties of knee articular cartilage.* Biorheology, 2003. **40**(1, 2, 3): p. 133-140.

7. O'Neill, T.W., P.S. McCabe, and J. McBeth, *Update on the epidemiology, risk factors and disease outcomes of osteoarthritis.* Best practice & research Clinical rheumatology, 2018. **32**(2): p. 312-326.

8. Kramer, W.C., K.J. Hendricks, and J. Wang, *Pathogenetic mechanisms of posttraumatic osteoarthritis: opportunities for early intervention.* International journal of clinical and experimental medicine, 2011. **4**(4): p. 285.

9. Mow, V.C., A. Ratcliffe, and A.R. Poole, *Cartilage and diarthrodial joints as paradigms for hierarchical materials and structures.* Biomaterials, 1992. **13**(2): p. 67-97.

10. Eyre, D., *Articular cartilage and changes in arthritis: collagen of articular cartilage.* Arthritis Research & Therapy, 2001. **4**(1): p. 30.

11. Luo, Y., et al., *The minor collagens in articular cartilage.* Protein & cell, 2017. **8**(8): p. 560-572.

12. Bergholt, M.S., et al., *Raman Spectroscopy Reveals New Insights into the Zonal Organization of Native and Tissue-Engineered Articular Cartilage.* ACS Central Science, 2016. **2**(12): p. 885-895.

13. Oliveria, S.A., et al., *Body weight, body mass index, and incident symptomatic osteoarthritis of the hand, hip, and knee.* Epidemiology, 1999: p. 161-166.

14. Neogi, T., *The epidemiology and impact of pain in osteoarthritis.* Osteoarthritis and cartilage, 2013. **21**(9): p. 1145-1153.

15. Thomas, A.C., et al., *Epidemiology of posttraumatic osteoarthritis.* Journal of athletic training, 2017. **52**(6): p. 491-496.

16. Brown, T.D., et al., *Posttraumatic osteoarthritis: A first estimate of incidence, prevalence, and burden of disease.* Journal of Orthopaedic Trauma, 2006. **20**(10): p. 739-744+747-748.

17. Oliestad, B., et al., *Knee osteoarthritis after anterior cruciate ligament injury.* Am J Sports Med, 2009. **37**(7): p. 1434-1443.

18. Saltzman, C.L., et al., *Epidemiology of ankle arthritis: report of a consecutive series of 639 patients from a tertiary orthopaedic center.* The Iowa orthopaedic journal, 2005. **25**: p. 44.

19. Valderrabano, V., et al., *Etiology of ankle osteoarthritis.* Clinical Orthopaedics and Related Research®, 2009. **467**(7): p. 1800.

20. Cross, J.D., et al., *Battlefield orthopaedic injuries cause the majority of long-term disabilities.* JAAOS-Journal of the American Academy of Orthopaedic Surgeons, 2011. **19**: p. S1-S7.

21. Riegger, J. and R.E. Brenner, *Pathomechanisms of Posttraumatic Osteoarthritis: Chondrocyte Behavior and Fate in a Precarious Environment.* International Journal of Molecular Sciences, 2020. **21**(5): p. 1560.

22. Ding, L., J.A. Buckwalter, and J.A. Martin, *DAMPs synergize with cytokines or fibronectin fragment on inducing chondrolysis but lose effect when acting alone.* Mediators of Inflammation, 2017. **2017**.

23. Anderson, D.D., et al., *Post-traumatic osteoarthritis: Improved understanding and opportunities for early intervention.* Journal of Orthopaedic Research, 2011. **29**(6): p. 802-809.

24. Ding, L., et al., *A single blunt impact on cartilage promotes fibronectin fragmentation and upregulates cartilage degrading stromelysin-1/matrix metalloproteinase-3 in a bovine ex vivo model.* Journal of Orthopaedic Research, 2014. **32**(6): p. 811-818.

25. Aulin, C., et al., *Increased alarmin levels after knee injuries suggests contribution to osteoarthritis development and potential therapeutic possibilities.* Osteoarthritis and Cartilage, 2020. **28**: p. S84.

26. Rosenberg, J.H., et al., *Damage-associated molecular patterns in the pathogenesis of osteoarthritis: potentially novel therapeutic targets.* Molecular and cellular biochemistry, 2017. **434**(1-2): p. 171-179.

27. Iqbal, S., et al., *Lubricin/Proteoglycan 4 binds to and regulates the activity of Toll-Like Receptors In Vitro.* Scientific reports, 2016. **6**: p. 18910.

28. Vogl, T., et al., *Mrp8 and Mrp14 are endogenous activators of Toll-like receptor 4, promoting lethal, endotoxin-induced shock.* Nature medicine, 2007. **13**(9): p. 1042-1049.

29. Schelbergen, R.F., et al., *Alarmins S100A8 and S100A9 elicit a catabolic effect in human osteoarthritic chondrocytes that is dependent on Toll‐like receptor 4.* Arthritis & Rheumatism, 2012. **64**(5): p. 1477-1487.

30. Millerand, M., F. Berenbaum, and C. Jacques, *Danger signals and inflammaging in osteoarthritis.* Clin Exp Rheumatol, 2019. **37**(Suppl 120): p. 48-56.

31. Liu-Bryan, R. and R. Terkeltaub, *Chondrocyte innate immune myeloid differentiation factor 88–dependent signaling drives procatabolic effects of the endogenous toll‐like receptor 2/toll‐like receptor 4 ligands low molecular weight hyaluronan and high mobility group box chromosomal protein 1 in mice.* Arthritis & Rheumatism, 2010. **62**(7): p. 2004-2012.

32. Rigoglou, S. and A.G. Papavassiliou, *The NF-κB signalling pathway in osteoarthritis.* The International Journal of Biochemistry & Cell Biology, 2013. **45**(11): p. 2580-2584.

33. Goldring, M.B. and K.B. Marcu, *Cartilage homeostasis in health and rheumatic diseases.* Arthritis Research & Therapy, 2009. **11**(3): p. 224.

34. Sebastian, A., et al., *Comparative Transcriptomics Identifies Novel Genes and Pathways Involved in Post-Traumatic Osteoarthritis Development and Progression.* International journal of molecular sciences, 2018. **19**(9): p. 2657.

35. Ulivi, V., et al., *p38/NF-kB-dependent expression of COX-2 during differentiation and inflammatory response of chondrocytes.* Journal of Cellular Biochemistry, 2008. **104**(4): p. 1393-1406.

36. B Marcu, K., et al., *NF-κB signaling: multiple angles to target OA.* Current drug targets, 2010. **11**(5): p. 599-613.

37. Chen, C.T., et al., *Chondrocyte necrosis and apoptosis in impact damaged articular cartilage.* Journal of Orthopaedic Research, 2001. **19**(4): p. 703-711.

38. Riegger, J., et al., *Antioxidative therapy in an ex vivo human cartilage trauma-model: Attenuation of trauma-induced cell loss and ECM-destructive enzymes by N-acetyl cysteine.* Osteoarthritis and cartilage, 2016. **24**(12): p. 2171-2180.

39. Wolff, K.J., et al., *Mechanical stress and ATP synthesis are coupled by mitochondrial oxidants in articular cartilage.* Journal of Orthopaedic Research, 2013. **31**(2): p. 191-196.

40. Coleman, M.C., et al., *Targeting mitochondrial responses to intra-articular fracture to prevent posttraumatic osteoarthritis.* Science translational medicine, 2018. **10**(427).

41. Lee, R., et al., *The effect of mechanical stress on cartilage energy metabolism.* Biorheology, 2002. **39**(1, 2): p. 133-143.

42. Son, Y., et al., *Mitogen-activated protein kinases and reactive oxygen species: how can ROS activate MAPK pathways?* Journal of signal transduction, 2011. **2011**.

43. Pantano, C., et al., *Redox-sensitive kinases of the nuclear factor-κB signaling pathway.* Antioxidants & redox signaling, 2006. **8**(9-10): p. 1791-1806.

44. Goldring, M.B., et al., *Roles of inflammatory and anabolic cytokines in cartilage metabolism: Signals and multiple effectors converge upon MMP-13 regulation in osteoarthritis.* European Cells and Materials, 2011. **21**: p. 202-220.

45. Terada, C., et al., *Gene expression and localization of high-mobility group box chromosomal protein-1 (HMGB-1) in human osteoarthritic cartilage.* Acta Medica Okayama, 2011. **65**(6): p. 369-377.

46. Lai, Y., et al., *ADAMTS-7 forms a positive feedback loop with TNF-α in the pathogenesis of osteoarthritis.* Annals of the rheumatic diseases, 2014. **73**(8): p. 1575-1584.

47. Goldring, M.B., *Articular cartilage degradation in osteoarthritis.* HSS journal, 2012. **8**(1): p. 7-9.

48. Kapoor, M., et al., *Role of proinflammatory cytokines in the pathophysiology of osteoarthritis.* Nature Reviews Rheumatology, 2010. **7**: p. 33.

49. Martel-Pelletier, J., et al., *The interleukin-1 receptor in normal and osteoarthritic human articular chondrocytes. Identification as the type I receptor and analysis of binding kinetics and biologic function.* Arthritis & Rheumatism: Official Journal of the American College of Rheumatology, 1992. **35**(5): p. 530-540.

50. Alaaeddine, N., et al., *Osteoarthritic synovial fibroblasts possess an increased level of tumor necrosis factor-receptor 55 (TNF-R55) that mediates biological activation by TNF-alpha.* The Journal of rheumatology, 1997. **24**(10): p. 1985-1994.

51. Chadjichristos, C., et al., *Sp1 and Sp3 transcription factors mediate interleukin-1β down-regulation of human type II collagen gene expression in articular chondrocytes.* Journal of Biological Chemistry, 2003. **278**(41): p. 39762-39772.

52. Shakibaei, M., et al., *Curcumin protects human chondrocytes from IL-1β-induced inhibition of collagen type II and β1-integrin expression and activation of caspase-3: an immunomorphological study.* Annals of Anatomy-Anatomischer Anzeiger, 2005. **187**(5-6): p. 487-497.

53. Schulze-Tanzil, G., et al., *Effects of curcumin (diferuloylmethane) on nuclear factor-kB signaling in interleukin-1b-stimulated chondrocytes.* Ann NY Acad Sci, 2004. **1030**: p. 578-86.

54. Stöve, J., et al., *Interleukin-1β induces different gene expression of stromelysin, aggrecan and tumor-necrosis-factor-stimulated gene 6 in human osteoarthritic chondrocytes in vitro.* Pathobiology, 2000. **68**(3): p. 144-149.

55. Séguin, C.A. and S.M. Bernier, *TNFα suppresses link protein and type II collagen expression in chondrocytes: Role of MEK1/2 and NF-κB signaling pathways.* Journal of cellular physiology, 2003. **197**(3): p. 356-369.

56. Saklatvala, J., *Tumour necrosis factor α stimulates resorption and inhibits synthesis of proteoglycan in cartilage.* Nature, 1986. **322**(6079): p. 547-549.

57. Henderson, B. and E. Pettipher, *Arthritogenic actions of recombinant IL-1 and tumour necrosis factor alpha in the rabbit: evidence for synergistic interactions between cytokines in vivo.* Clinical and experimental immunology, 1989. **75**(2): p. 306.

58. Punzi, L., et al., *Post-traumatic arthritis: overview on pathogenic mechanisms and role of inflammation.* RMD open, 2016. **2**(2): p. e000279.

59. Deyle, G.D., et al., *Physical Therapy versus Glucocorticoid Injection for Osteoarthritis of the Knee.* New England Journal of Medicine, 2020. **382**(15): p. 1420-1429.

60. Sun, E., et al., *Association of Early Physical Therapy With Long-term Opioid Use Among Opioid-Naive Patients With Musculoskeletal Pain.* JAMA Network Open, 2018. **1**(8): p. e185909-e185909.

61. Deyle, G.D., et al., *A multicentre randomised, 1-year comparative effectiveness, parallel-group trial protocol of a physical therapy approach compared to corticosteroid injections.* BMJ Open, 2016. **6**(3): p. e010528.

62. Denegar, C.R., et al., *Preferences for heat, cold, or contrast in patients with knee osteoarthritis affect treatment response.* Clinical interventions in aging, 2010. **5**: p. 199-206.

63. Rutjes, A.W.S., et al., *Therapeutic ultrasound for osteoarthritis of the knee or hip.* Cochrane Database of Systematic Reviews, 2010(1).

64. Zeng, C., et al., *Electrical stimulation for pain relief in knee osteoarthritis: systematic review and network meta-analysis.* Osteoarthritis and Cartilage, 2015. **23**(2): p. 189-202.

65. Bannwarth, B., *Acetaminophen or NSAIDs for the treatment of osteoarthritis.* Best Practice & Research Clinical Rheumatology, 2006. **20**(1): p. 117-129.

66. Nelson, A.E., et al., *A systematic review of recommendations and guidelines for the management of osteoarthritis: The Chronic Osteoarthritis Management Initiative of the U.S. Bone and Joint Initiative.* Seminars in Arthritis and Rheumatism, 2014. **43**(6): p. 701-712.

67. Arroll, B. and F. Goodyear-Smith, *Corticosteroid injections for osteoarthritis of the knee: meta-analysis.* Bmj, 2004. **328**(7444): p. 869.

68. Khoja, S.S., G.J. Almeida, and J.K. Freburger, *Recommendation Rates for Physical Therapy, Lifestyle Counseling, and Pain Medications for Managing Knee Osteoarthritis in Ambulatory Care Settings: A Cross-Sectional Analysis of the National Ambulatory Care Survey (2007–2015).* Arthritis Care & Research, 2020. **72**(2): p. 184-192.

69. Dhawan, A., et al., *An Epidemiologic Analysis of Clinical Practice Guidelines for Non-Arthroplasty Treatment of Osteoarthritis of the Knee.* Arthroscopy: The Journal of Arthroscopic & Related Surgery, 2014. **30**(1): p. 65-71.

70. Raeissadat, S.A., et al., *Knee osteoarthritis injection choices: platelet-rich plasma (PRP) versus hyaluronic acid (a one-year randomized clinical*

trial). Clinical Medicine Insights: Arthritis and Musculoskeletal Disorders, 2015. **8**: p. CMAMD. S17894.

71. Wang, C.-T., et al., *Therapeutic effects of hyaluronic acid on osteoarthritis of the knee: a meta-analysis of randomized controlled trials.* JBJS, 2004. **86**(3): p. 538-545.

72. Bannuru, R.R., et al., *Therapeutic trajectory of hyaluronic acid versus corticosteroids in the treatment of knee osteoarthritis: A systematic review and meta‐analysis.* Arthritis Care & Research, 2009. **61**(12): p. 1704-1711.

73. Riboh, J.C., et al., *Effect of leukocyte concentration on the efficacy of platelet-rich plasma in the treatment of knee osteoarthritis.* The American journal of sports medicine, 2016. **44**(3): p. 792-800.

74. Yanke, A.B. and B.J. Cole, *Joint Preservation of the Knee: A Clinical Casebook*. 2019: Springer.

75. Baumann, C.A., et al., *Articular Cartilage: Structure and Restoration*, in *Joint Preservation of the Knee*. 2019, Springer. p. 3-24.

76. Gomoll, A.H., et al., *Treatment of chondral defects in the patellofemoral joint.* The journal of knee surgery, 2006. **19**(04): p. 285-295.

77. Bentley, G., et al., *A prospective, randomised comparison of autologous chondrocyte implantation versus mosaicplasty for osteochondral defects in the knee.* The Journal of bone and joint surgery. British volume, 2003. **85**(2): p. 223-230.

78. Emre, T., et al., *Autologous osteochondral transplantation (mosaicplasty) in articular cartilage defects of the patellofemoral joint: retrospective analysis of 33 cases.* Musculoskeletal surgery, 2017. **101**(2): p. 133-138.

79. Nho, S.J., et al., *Magnetic resonance imaging and clinical evaluation of patellar resurfacing with press-fit osteochondral autograft plugs.* The American journal of sports medicine, 2008. **36**(6): p. 1101-1109.

80. Astur, D.C., et al., *Autologous osteochondral transplantation for treating patellar chondral injuries: evaluation, treatment, and outcomes of a two-year follow-up study.* JBJS, 2014. **96**(10): p. 816-823.

81. Bentley, G., et al., *Minimum ten-year results of a prospective randomised study of autologous chondrocyte implantation versus mosaicplasty for symptomatic articular cartilage lesions of the knee.* The Journal of bone and joint surgery. British volume, 2012. **94**(4): p. 504-509.

82. Spak, R.T. and R.A. Teitge, *Fresh osteochondral allografts for patellofemoral arthritis: long-term followup.* Clinical Orthopaedics and Related Research®, 2006. **444**: p. 193-200.

83. Gillogly, S.D. and R.M. Arnold, *Autologous chondrocyte implantation and anteromedialization for isolated patellar articular cartilage lesions: 5-to 11-year follow-up.* The American journal of sports medicine, 2014. **42**(4): p. 912-920.

84. O'Loughlin, P.F., B.E. Heyworth, and J.G. Kennedy, *Current concepts in the diagnosis and treatment of osteochondral lesions of the ankle.* The American Journal of Sports Medicine, 2010. **38**(2): p. 392-404.

85. Carey, J.L., *Fibrocartilage following microfracture is not as robust as native articular cartilage: commentary on an article by Aaron J. Krych, MD, et al.:"Activity levels are higher after osteochondral autograft transfer mosaicplasty than after microfracture for articular cartilage defects of the knee. A retrospective comparative study".* JBJS, 2012. **94**(11): p. e80.

86. W-Dahl, A., et al., *Unicompartmental knee arthroplasty in patients aged less than 65: combined data from the Australian and Swedish Knee Registries.* Acta orthopaedica, 2010. **81**(1): p. 90-94.

87. Brown, B.N. and S.F. Badylak, *Extracellular matrix as an inductive scaffold for functional tissue reconstruction.* Translational Research, 2014. **163**(4): p. 268-285.

88. Ratner, B.D., et al., *Biomaterials science: an introduction to materials in medicine*. 2004: Elsevier.

89. Uzman, A., *Molecular Cell Biology (4th edition) Harvey Lodish, Arnold Berk, S. Lawrence Zipursky, Paul Matsudaira, David Baltimore and James Darnell; Freeman & Co., New York, NY, 2000, 1084 pp., list price $102.25, ISBN 0-7167-3136-3.* Biochemistry and Molecular Biology Education, 2001. **29**(3): p. 126-128.

90. Williams, D.F., *On the mechanisms of biocompatibility.* Biomaterials, 2008. **29**(20): p. 2941-2953.

91. Franz, S., et al., *Immune responses to implants–a review of the implications for the design of immunomodulatory biomaterials.* Biomaterials, 2011. **32**(28): p. 6692-6709.

92. Lin, K., et al., *Advanced Collagen-Based Biomaterials for Regenerative Biomedicine.* Advanced Functional Materials, 2019. **29**(3): p. 1804943.

93. Shoulders, M.D. and R.T. Raines, *Collagen structure and stability.* Annual review of biochemistry, 2009. **78**: p. 929-958.

94. Gordon, M.K. and R.A. Hahn, *Collagens.* Cell and tissue research, 2010. **339**(1): p. 247.

95. Bella, J., *Collagen structure: new tricks from a very old dog.* Biochemical Journal, 2016. **473**(8): p. 1001-1025.

96. Rich, A. and F. Crick, *The molecular structure of collagen.* Journal of molecular biology, 1961. **3**(5): p. 483-IN4.

97. Ramachandran, G.N., *Structure of collagen at the molecular level.* Treatise of collagen, 1967. **1**: p. 103-183.

98. Akeson, W., et al., *Collagen cross-linking alterations in joint contractures: changes in the reducible cross-links in periarticular connective tissue collagen after nine weeks of immobilization.* Connective Tissue Research, 1977. **5**(1): p. 15-19.

99. Scott, I., M. Yamauchi, and M. Sricholpech, *Lysine post-translational modifications of collagen.* Essays in biochemistry, 2012. **52**: p. 113-133.

100. Fujimoto, D., K.-y. Akiba, and N. Nakamura, *Isolation and characterization of a fluorescent material in bovine achilles tendon collagen.* Biochemical and biophysical research communications, 1977. **76**(4): p. 1124-1129.

101. Li, Y., *The mechanism of collagen self-assembly: Hydrophobic and electrostatic interactions*. 2009: University of Florida.

102. Li, Y.Y., et al., *Mesenchymal stem cell-collagen microspheres for articular cartilage repair: Cell density and differentiation status.* Acta Biomaterialia, 2014. **10**(5): p. 1919-1929.

103. Yuan, M., K.W. Leong, and B.P. Chan, *Three-dimensional culture of rabbit nucleus pulposus cells in collagen microspheres.* The Spine Journal, 2011. **11**(10): p. 947-960.

104. Chan, B.P., et al., *Self-assembled collagen–human mesenchymal stem cell microspheres for regenerative medicine.* Biomaterials, 2007. **28**(31): p. 4652-4666.

105. Cheng, H.-w., et al., *In vitro generation of an osteochondral interface from mesenchymal stem cell–collagen microspheres.* Biomaterials, 2011. **32**(6): p. 1526-1535.

106. Chowdhury, D.K. and A.K. Mitra, *Kinetics of in vitro release of a model nucleoside deoxyuridine from crosslinked insoluble collagen and collagen–gelatin microspheres.* International journal of pharmaceutics, 1999. **193**(1): p. 113-122.

107. Yao, L., F. Phan, and Y. Li, *Collagen microsphere serving as a cell carrier supports oligodendrocyte progenitor cell growth and differentiation for neurite myelination in vitro.* Stem cell research & therapy, 2013. **4**(5): p. 109.

108. Yang, C. and J. Wang, *Preparation and characterization of collagen microspheres for sustained release of steroidal saponins.* Materials Research, 2014. **17**(6): p. 1644-1650.

109. Nagai, N., et al., *Preparation and characterization of collagen microspheres for sustained release of VEGF.* Journal of Materials Science: Materials in Medicine, 2010. **21**(6): p. 1891-1898.

110. Mumcuoglu, D., et al., *Collagen I derived recombinant protein microspheres as novel delivery vehicles for bone morphogenetic protein-2.* Materials Science and Engineering: C, 2018. **84**: p. 271-280.

111. Matsuhashi, A., et al., *Fabrication of fibrillized collagen microspheres with the microstructure resembling an extracellular matrix.* Soft Matter, 2015. **11**(14): p. 2844-2851.

112. Liu, J., et al., *Chondrocytes behaviors within type I collagen microspheres and bulk hydrogels: an in vitro study.* RSC Advances, 2015. **5**(67): p. 54446-54453.

113. Mathieu, M., et al., *Induction of mesenchymal stem cell differentiation and cartilage formation by cross-linker-free collagen microspheres.* Eur Cell Mater, 2014. **28**: p. 82-96.

114. Yoon, H., et al., *Development of cell-laden 3D scaffolds for efficient engineered skin substitutes by collagen gelation.* RSC advances, 2016. **6**(26): p. 21439-21447.

115. Kim, W. and G. Kim, *Collagen/bioceramic-based composite bioink to fabricate a porous 3D hASCs-laden structure for bone tissue regeneration.* Biofabrication, 2019. **12**(1): p. 015007.

116. Skardal, A., et al., *Bioprinted amniotic fluid-derived stem cells accelerate healing of large skin wounds.* Stem cells translational medicine, 2012. **1**(11): p. 792-802.

117. Yang, X., et al., *Collagen-alginate as bioink for three-dimensional (3D) cell printing based cartilage tissue engineering.* Materials Science and Engineering: C, 2018. **83**: p. 195-201.

118. Chen, C., et al., *Collagen/heparin sulfate scaffolds fabricated by a 3D bioprinter improved mechanical properties and neurological function after*

spinal cord injury in rats. Journal of Biomedical Materials Research Part A, 2017. **105**(5): p. 1324-1332.

119. Hinton, T.J., et al., *Three-dimensional printing of complex biological structures by freeform reversible embedding of suspended hydrogels.* Science Advances, 2015. **1**(9): p. e1500758.

120. Senior, J.J., et al., *Fabrication of Complex Hydrogel Structures Using Suspended Layer Additive Manufacturing (SLAM).* Advanced Functional Materials, 2019. **29**(49): p. 1904845.

121. Lee, A., et al., *3D bioprinting of collagen to rebuild components of the human heart.* Science, 2019. **365**(6452): p. 482.

Chapter Two

INTRODUCTION TO RESEARCH

2.1 Significance of Research

Current techniques to mitigate progression of PTOA are lacking. Pain management and articular function are the focus of treatment today without addressing the progressive degradation of PTOA [1]. The regeneration of native articular tissue is another aspect of PTOA not addressed today. Some treatments like microfractures and autologous chondrocyte implantation, and osteochondral grafting help to stimulate regeneration of tissue at damaged sites albeit with mixed results [2, 3]. With microfracturing, the regenerated tissue does cover the damage it also is not ideal as the tissue formed is not as stable and can degrade more quickly which becomes a problem in the future for patients [4]. The ability to mitigate catabolic factors that progress PTOA over time is essential if establishment of new native articular tissues are to be successfully achieved [5]. The significance of this work is to develop a targeted injectable based therapeutic to mitigate progression of PTOA and a delivery technique of autologous stem cells to regenerate native cartilage after mitigation of PTOA progression. CMs provide an easily injectable material that can be loaded with known PTOA mitigating, anti-inflammatory, or cells and can be conjugated with targeting antibodies that can bind to damaged cartilage regions.

2.2 Research Objectives

Fabrication of a novel liquid collagen solution that fibrilizes when introduced into ionic solutions or introduced into physiologic temperatures was the genesis of this work. Exploiting the unique fibrilizing characteristics of the liquid collagen was of peak interest. Fabrication of this liquid collagen into CMs and the ability to 3D print with it as well were the most appreciable for the material and were further investigated in the following chapters.

The main objective of this work was to develop, characterize, and optimize a technique to fabricate CMs that are suitable for intraarticular injection for treatment of PTOA. Initial work was performed to determine best techniques to fabricate uniform CMs with collagen fibril formation. To achieve uniform CMs multiple techniques of fabrication were investigated such as water in oil emulsion, water in water emulsion, and probe sonication. Water in oil emulsion was tapped due to its ease of reproducibility. Multiple oils and surfactants were studied to see how the liquid collagen interacted. Chemical crosslinking while in emulsion was also evaluated to conjugate nanoparticles such as gold. Gold nanoparticles are known free radicle scavengers that reduce reactive oxygen species [6, 7]. Light microscopy was used to observe the CMs fabricated. Scanning electron microscopy (SEM), polarized light microscopy, and FTIR analysis was used to determine fibril formation of the of the collagen within the CMs. Fibril formation provides evidence of a stable collagen structure at physiologic temperatures and also emulates a native tissue network [8]. Work then progressed into general *in vitro* testing to help determine biocompatibility of CMs. A WST-1 assay was

utilized to determine biocompatibility of CMs and identify if length of emulsion also played a role in biocompatibility. Finally, more application-based testing of CMs as a PTOA treatment were investigated. Specific binding of CMs loaded with anti-inflammatory agents is of peak interest. Conjugation of collagen type II antibodies (CIIMAb) to CMs was investigated using fluorescent imaging. Ex vivo studies of CIIMAb-CMs exposed to damaged porcine cartilage were performed to verify specific binding of CIIMAb-CMs to damaged cartilage sites. Testing to determine CMs proclivity to mitigate PTOA progression through ROS mitigation was examined. *In vitro* work exposing chondrocyte cells to procatabolic factors observed in a PTOA environment were studied with anti-inflammatory loaded CMs.

A secondary objective of this work was to develop and characterize a technique to 3D print with the liquid collagen solution. Significant work on optimizing the parameters of printing the material were investigated along with solutions in which the liquid collagen could be printed into were also of interest. The goal of this work was to print reproducible collagen scaffolds. A BioX extrusion based 3D printer by Cellink was utilized in this work along with a custom built printer. As mentioned previously, initial work to determine optimal extrusion rate and printing speed were tested through visual inspection under a microscope to examine collagen dimeters. Rates that provided uniform diameters were chosen due to making the most reproducible scaffold. Various printing solutions were also investigated. Printing into agarose microparticles provides better support and resolution of printed scaffolds but also include more washing

to remove agarose off of the scaffold. Printing parameters also have to be adjusted depending on each solution printed into. In vitro work was also performed with the printed scaffolds. It became evident crosslinking of the scaffolds prior to in vitro work would be necessary to maintain the structural integrity of the scaffold. Genipin crosslinking was not only used to chemically crosslink the scaffolds but to also conjugate gold nanoparticles. Work was also performed to coat the collagen scaffolds with laminin to aid cellular attachment. Biocompatibility analysis was performed with the printed scaffolds.

2.3 References

1. Schenker, M.L., R.L. Mauck, and S. Mehta, *Pathogenesis and prevention of posttraumatic osteoarthritis after intra-articular fracture.* Journal of the American Academy of Orthopaedic Surgeons, 2014. **22**(1): p. 20-28.

2. Bentley, G., et al., *Minimum ten-year results of a prospective randomised study of autologous chondrocyte implantation versus mosaicplasty for symptomatic articular cartilage lesions of the knee.* The Journal of bone and joint surgery. British volume, 2012. **94**(4): p. 504-509.

3. Spak, R.T. and R.A. Teitge, *Fresh osteochondral allografts for patellofemoral arthritis: long-term followup.* Clinical Orthopaedics and Related Research®, 2006. **444**: p. 193-200.

4. Goyal, D., et al., *Evidence-based status of microfracture technique: a systematic review of level I and II studies.* Arthroscopy: The Journal of Arthroscopic & Related Surgery, 2013. **29**(9): p. 1579-1588.

5. Anderson, D.D., et al., *Post-traumatic osteoarthritis: Improved understanding and opportunities for early intervention.* Journal of Orthopaedic Research, 2011. **29**(6): p. 802-809.

6. Smith, S.E., et al., *Homogenized porcine extracellular matrix derived injectable tissue construct with gold nanoparticles for musculoskeletal tissue engineering applications.* Journal of Biomaterials and Nanobiotechnology, 2017. **8**(02): p. 125.

7. BarathManiKanth, S., et al., *Anti-oxidant effect of gold nanoparticles restrains hyperglycemic conditions in diabetic mice.* Journal of nanobiotechnology, 2010. **8**(1): p. 16.

8. Gevorkian, S.G., et al., *Stabilization and anomalous hydration of collagen fibril under heating.* PLoS One, 2013. **8**(11): p. e78526.

Chapter Three

IN VITRO INVESTIGATION OF A SUPPLEMENTED INJECTABLE GOLD NANOPARTICLE PORCINE EXTRACELLULAR MATRIX

3.1 Abstract

An injectable homogenized porcine diaphragm tissue scaffold (HT) was developed in this work. HT was conjugated with 20 nm gold nanoparticles (AuNP) and supplemented with curcumin and hyaluronic acid. It is proposed the injectable scaffold will present therapeutic applications for post-traumatic osteoarthritis (PTOA). PTOA is a progressive articular degenerative disease that degrades articular cartilage and stimulates apoptosis in chondrocyte cells found in articular cartilage. The porcine diaphragm tissue was homogenized using a blade homogenizer and AuNPs were conjugated using EDC/NHS chemical crosslinking. Injection force testing, thermal stability, release rate, and scanning electron microscopy with energy-dispersive X-ray spectroscopy were utilized to characterize the supplemented HT scaffolds. *In vitro* testing with L929 murine fibroblasts, equine synovial fibroblasts, and HCH human chondrocytes were used to study the supplemented HT scaffolds biocompatibility, reactive oxygen species (ROS) reduction, and chondroprotective ability. Conjugation of 20 nm AuNPs to HT was successful using EDC/NHS crosslinking. Injection force of the scaffolds were sufficiently low enough to be a viable injectable therapeutic. *In vitro* work provided evidence of good biocompatibility with a propensity to reduce

intracellular ROS and an ability to mitigate apoptosis of chondrocyte cells stimulated with IL-1β, a known apoptosis inducing cytokine.

List of Figure Abbreviations

HT = homogenized tissue scaffold

LHT = lyophilized homogenized tissue scaffold

Au = 20 nm gold nanoparticles

Cu = curcumin

HA = hyaluronic acid

3.2 Introduction

The use of tissue derived scaffolds for therapeutic applications are becoming increasing popular due to reduced immunogenicity relative to some synthetic therapies and the advantage of native *in vivo* biodegradability mechanisms to remove and replace tissue derived scaffolds over time [1]. Tissue derived scaffolds require the removal of cellular remnants while maintaining the native tissue microstructure which is vital to biocompatibility [2]. Removal of cellular remnants ensures minimal host response while an intact cellular microenvironment plays important roles in cell cycle progression, cell fate decision, and migration of cells in terms of biomechanical cues [2, 3]. Biomechanics of the microenvironment not only play an important role, but cellular biochemical interactions play a critical role. Tissue scaffold microenvironments are inherently encumbered with cytokines, growth factors, and integrins that can stimulate recruitment and migration of cells along with cues for repair and regeneration in the region of implementation [4-8].

Homogenization of acellular tissue allows for more flexibility in terms of therapeutic applications [9]. Homogenized tissue is amendable for injections with the added benefit of maintaining the biochemical advantages and conforming to the shape of its environment. One advantageous application would be to utilize an injectable material for the treatment of post traumatic osteoarthritis (PTOA).

PTOA is a disease wherein a traumatic event propagates the degradation of articular cartilage over time [10]. Articular cartilage is the cartilage found on the end of bones in the joint space to aid articulation of joints and ease the impact

placed on the joint. To date, no cure has been identified to stop the degradation of articular cartilage. Temporary therapies that ease pain and aid articulation are used today. Over time the articular cartilage fully degrades leaving bone-on-bone articulation which can be debilitating to patients, greatly reducing quality of life. The progression of PTOA begins with immediate necrosis of chondrocyte cells after a direct, traumatic impact. This impact also affects chondrocyte cells surrounding the impacted region. These surrounding chondrocyte cells become dysregulated and hypertrophic releasing cytokines like interleukin-1β (IL-1β) that further dysregulate the cells, degrade the articular cartilage matrix, and eventually lead to apoptosis of cells [11-15].

Hyaluronic acid (HA) is a naturally occurring glycosaminoglycan found in the body. HA is well known for its lubricating ability found in the synovial fluid of the joint and in articular cartilage. It can increase the viscosity of the fluid and aids in compression absorption of the articular cartilage by drawing water into the tissue [16]. HA has also been shown to play a role in tissue regeneration and manipulating the inflammatory response [17].

Curcumin is a naturally derived component of turmeric that has been used in many therapeutic applications [18-20]. Curcumin is known for its anti-inflammatory and free radical scavenging ability [21]. Work performed by Shakibaei et al demonstrated curcumins interaction with osteoarthritic human chondrocyte cells. They observed a downregulation of known osteoarthritic pathway NF-kB through incubation with curcumin with IL-1β and tumor necrosis factor-α stimulated chondrocyte cells [22].

Gold nanoparticles (AuNPs) also possess a number of advantageous properties in support of aiding PTOA. Research with AuNPs have shown a reduction in inflammation through free radical scavenging [9, 23-25]. Research has also shown encouragement of cellular migration and attachment which is believed to be achieved through the surface energy of the AuNPs [26]. Also, manipulation of the degradation rate of the scaffold may be possible due to conjugated AuNPs blocking collagenase degradation [27].

This work describes the use of decellularized homogenized porcine diaphragm extracellular matrix tissue (HT) supplemented with curcumin, HA, and conjugated AuNPs. Material characteristics of the homogenized matrix was characterized to determine injectability, thermal stability, scanning electron microscopy along with energy dispersive X-ray spectroscopy to verify evidence of AuNP conjugation, and analysis of how curcumin releases from the scaffold. *In vitro* analysis was also performed with murine fibroblast cells, equine synovial fibroblast cells and human chondrocyte cells to determine the biocompatibility, free radical scavenging, and chondroprotective ability of the supplemented HT.

3.3 Materials and Methods

3.3.1 HT Scaffold Preparation

3.3.1.1 Harvesting Tissue and Tissue Decellularization

Porcine diaphragm tissue was harvested from the University of Missouri School of Medicine after euthanasia. Once the tissue was removed from the donor, this tissue was subsequently placed in a Tris buffer solution for transfer. To decellularize the diaphragm tissue, tissues were placed in a 1% (v/v) tributyl phosphate Tris buffer solution and agitated on a shaker table at 225 rpm for 24 hours. After the initial wash two 24-hour washes in DI H_2O followed by a 24-hour wash in 70% (v/v) ethyl alcohol were carried out. All tissues were then stored in 70% (v/v) ethyl alcohol at 4°C.

3.3.1.2 Tissue Homogenization

A blade homogenizer was used for tissue homogenization. Diaphragm tissue was manually cut into small pieces using a scalpel to aid homogenization prior to using the blade homogenizer. Approximately 1 gram of wet tissue was added to 15 ml of phosphate buffered saline (PBS). The tissue/PBS solution was placed on ice 15 minutes prior to homogenization. The tissue/PBS solution remained on ice during homogenization to keep the solution cool. To homogenize, the blade homogenizer was set to setting 5 and immersed into the tissue/PBS solution for 1 minute and taken out of the solution for 1 minute. This was cycled 5 times to make a prepared HT solution. The HT was stored at 4°C for later testing.

3.3.1.3 Preparation of Homogenized Construct

20 nm gold nanoparticles (AuNPs) were purchased from Ted Pella (Redding, CA). AuNPs are at a stock concentration of $7.0x10^{11}$ particles/ml. In this work this stock concentration is considered a "1X" concentration with "4X" being 4 times the amount of AuNPs per ml. 1-ethyl-3-[3-dimethylainopropyl] carbodiimide (EDC)/ N-hydroxysuccinimide (NHS) crosslinking was utilized to conjugate AuNPs to the HT. AuNPs were functionalized with 15 uM 2-mercaptoethylamine (MEA). To prepare the crosslinking solution, 5 mM NHS was dissolved in dimethylformamide (DMF) and 2 mM EDC was dissolved in a 0.1 M 2-(N-Morpholino) ethanesulfonic acid (MES) in 0.5 M NaCl. The HT was added to the crosslinking solution along with functionalized AuNPs and placed on a shaker table at 225 rpm for 1 hour. After 1 hour, the tissue constructs were washed with PBS three times by centrifugation at 5,000 rpm.

Addition of either curcumin or HA was performed after crosslinking of AuNPs to the tissue. Curcumin was purchased from Sigma Aldrich and HA was purchased from Lifecore Biomedical (MW=700kDa, Chaska, MN). HA was rehydrated from a lyophilized powder with sterile PBS to their respective concentrations. 15% (w/v) HA was used in all cell studies. Curcumin was dissolved in 1 N sodium hydroxide (NaOH). 4% (w/v) curcumin concentration was used in cell work unless otherwise stated.

3.3.1.4 Sterilization

Samples were sterilized using a 0.1% (v/v) peracetic acid solution with 1 M NaCl. Samples were placed on a shaker table at 225 rpm for 24 hours. After 24 hours, the samples were centrifuged at 5,000 rpm for 5 minutes to remove the supernatant and washed with sterile PBS three times.

3.3.2 Scanning Electron Microscopy

A FEI Quanta 600 FEG Environmental scanning electron microscope (SEM) and energy-dispersive x-ray spectroscopy (EDS) (Hillsboro, OR) was used for imaging and elemental analysis. Samples were placed in a fixative solution provided by the University of Missouri Electron Microscopy Core of 100 nM sodium cacodylate, 2% glutaraldehyde, and 2% paraformaldehyde overnight and rinsed three times with H_2O. Samples were placed on carbon tape.

3.3.3 Injection Force

An Instron 5900R Universal Testing machine (Norwood, MA) was used in compression mode to determine maximum extrusion force of HT through a 22-gauge cannula. A constant rate of displacement (0.167 mm/s) was used to determine force of extrusion for 30 mm intervals. Force was determined every 0.1 seconds.

3.3.4 Release Rate

A UV-Vis spectrophotometer was used to determine the release of curcumin from a 50 µl centrifuged pellet of HT. The HT was incubated in 6% (v/v) curcumin for 24 hours and washed 3 times with PBS prior to being tested. Samples were then incubated at 37°C in 1 ml of PBS. 1 ml PBS was removed and replaced at 0, 1, 2, 6, and 9 day of incubation to determine the release profile.

3.3.5 Cell Culture

3.3.5.1 L929 Fibroblast Cells

L929 murine fibroblast cells (ATCC, Manassas,VA) were cultured in Eagle's minimum essential medium (EMEM, ATCC, Manassas, VA) with 10 % (v/v) horse serum (ATCC, Manassas,VA) and 200 U/ml penicillin streptomycin (ATCC, Manassas,VA) cultured at 37°C with 5% CO_2. Assays were performed up to 20 subcultivations with subculturing performed weekly. Media was exchanged every 3 days when performing an assay. All culturing of cells were performed under sterile conditions using a biologic safety cabinet.

3.3.5.2 HCH Chondrocyte Cells

HCH human chondrocyte cells (Promocell GmbH, Heidelberg, DE) were cultured in human chondrocyte media (Promocell GmbH, Heidelberg, DE) supplemented with 0.1 ml/ml fetal calf serum (Promocell GmbH, Heidelberg, DE) cultured at 37°C with 5% CO_2. Assays were performed up to 20 subcultivations

with subculturing performed weekly. Media was exchanged every 3 days when performing an assay. All culturing of cells were performed under sterile conditions using a biologic safety cabinet.

3.3.5.3 Synovial Fibroblast Cells

Equine synovial fibroblast cells provided from D.B. Fox's lab group at the University of Missouri were cultured at 37°C with 5% CO_2 with DMEM supplemented with 10% fetal bovine serum, 0.008% Hepe's buffer, 0.008% non-essential amino acids, 0.002% penicillin 100 I.U./mL streptomycin 100 ug/mL, amphoterocin B 25 ug/mL, 0.002% L-ascorbate, and 0.01% L-glutamine. Cells were assayed at their 4^{th} passage. All culturing of cells were performed under sterile conditions using a biologic safety cabinet.

3.3.6 Cell Viability Assay

A WST-1 assay kit (Roche, Indianapolis, IN) was used to determine cellular viability of both L929 murine fibroblast and HCH chondrocyte cells. $3x10^4$ cells/well were added to a 96-well plate for culture. Cells were incubated for 24 hours prior to addition of HT. 50 µl centrifuged pellets of HT was incubated in relevant cellular media 24 hours prior to addition with cells. Media was exchanged every 3 days. The WST-1 reagent was added to each well per manufactures protocol and incubated for 4 hours. 450 nm absorbance value with a cutoff of 650 nm was evaluated using a Cytation 5 (BioTek, Winooski, VT).

3.3.7 ROS Assay

An OxiSelect ROS assay kit (Cell Biolabs, San Diego, CA) was used to determine ROS activity per sample group with L929 fibroblast, synovial fibroblast, and HCH chondrocyte cells. $3x10^4$ cells/well were plated onto a 96-well plate for culture with media being changed every 3 days. Cells were incubated for 24 hours to become confluent. After 24 hours, cells were washed with DPBS two times and then 1X 2', 7'-Dichlorodihydrofluorescin diacetate (DCF-DA) diluted in media was added to each well for 1 hour. Cells were then washed with DPBS two times to remove the DCF-DA. 50 µl centrifuged pellets of HT was incubated in relevant cellular media 24 hours prior to addition with cells. Cell media and HT was then added to the well plate. The HT and cells were incubated together for 12 hours. After 12 hours cells were lysed using a cell lysis buffer provided in the assay kit. A Cytation 5 (BioTek, Winooski, VT) was used to determine the fluorescent intensity at 480 nm excitation and 530 nm emission. The concentration of DCF was determined by linear regression using a provided DCF standard.

3.3.8 Apoptosis Assay

An HT TiterTACS assay kit (Trevigen, Gaithersburg, MD) was used to determine apoptosis of HCH chondrocyte cells under stimulation of IL-1β. $4x10^4$ cells/well were incubated for 24 hours in a 96-well plate to become confluent. Cells were then exposed to 10 ng/ml IL-1β for 24 hours. Cells were then washed twice with DPBS and fixed with 3.7% (v/v) formaldehyde at room temperature for

7 minutes. Cells were washed with DPBS twice and incubated for 20 minutes in methanol, washed with DPBS and incubated with proteinase k for 15 minutes. Samples were washed with dH_2O then TACS-nuclease was then added to positive control groups or experimental groups were incubated for 30 minutes. H_2O_2 was added for 5 minutes to quench endogenous peroxidase activity and washed with dH_2O. Cells were then labeled with 1x TdT labeling buffer for 5 minutes and then incubated in the cell incubator for 1 hour with the provided labeling reaction mix. After 1 hour, a 1x TdT stop buffer was added for 5 minutes at room temperature. Samples were washed with PBS twice. Finally, cells were incubated with Strep-HRP and TACS-Sapphire for 10 minutes and 30 minutes respectively at room temperature and washed with 0.1% (v/v) tween-20/PBS after the Strep-HRP incubation. 0.2 N HCl was added and samples were measured with an absorbance of 450 nm with a 650 nm cutoff using a Cytation 5 (BioTek, Winooski, VT).

3.3.9 Statistical Analysis

Statistical analysis was performed using GraphPad Prism 8 software. A one way analysis of variance with pairwise Tukey test was performed with $p \leq 0.05$ unless denoted otherwise in figure description. The mean with error bars representing standard deviation were utilized in this work.

3.4 Results

3.4.1 Electron Microscopy

Conjugation of 4x 20 nm AuNPs to HT was analyzed using SEM and EDS analysis techniques. Samples of HT conjugated with AuNPs and HT conjugated with AuNPs incubated in 6% curcumin were observed to determine if the AuNPs were indeed conjugated to the HT. Figure 3.1A is an image of the HT conjugated with AuNPs. There are small white spots scattered throughout the tissue which are the AuNPs. Figure 3.1B is a backscattered image showing the AuNP spots more prominently. The red box is the spot used for EDS analysis. Figure 3.1C shows the EDS spectra. There is a clear peak of Au at 2.120 keV confirming the presence of AuNPs. Figure 3.1D provides evidence of the tissues porous microstructure maintained through the process of homogenization and

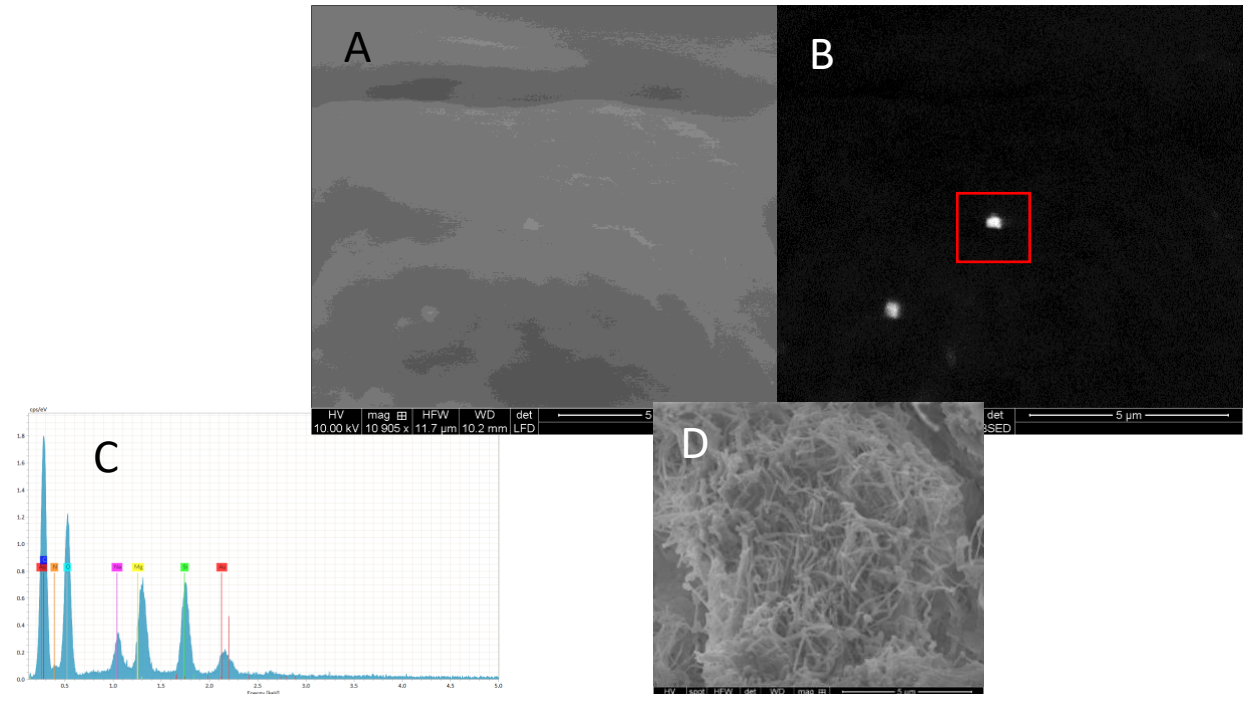

Figure 3.1. SEM and EDS analysis of HT conjugated with 20 nm AuNPs. (A) Scattering electron image on the surface of HT with conjugated AuNPs. (B) Backscattered electron image of AuNPs, red box shows spot where EDS spectra was acquired. (C) EDS spectra of HT. (D) Scattering electron image on the surface of HT.

conjugation of AuNPs. Similarly, for the HT conjugated with AuNPs and incubated in curcumin, Figure 3.2A shows AuNPs scattered throughout the tissue with Figure 3.2B, the backscatter image providing a clearer view of the AuNPs in the tissue. Finally, the red box shows where the EDS spectra was taken, and an Au peak can again be identified at 2.120 keV.

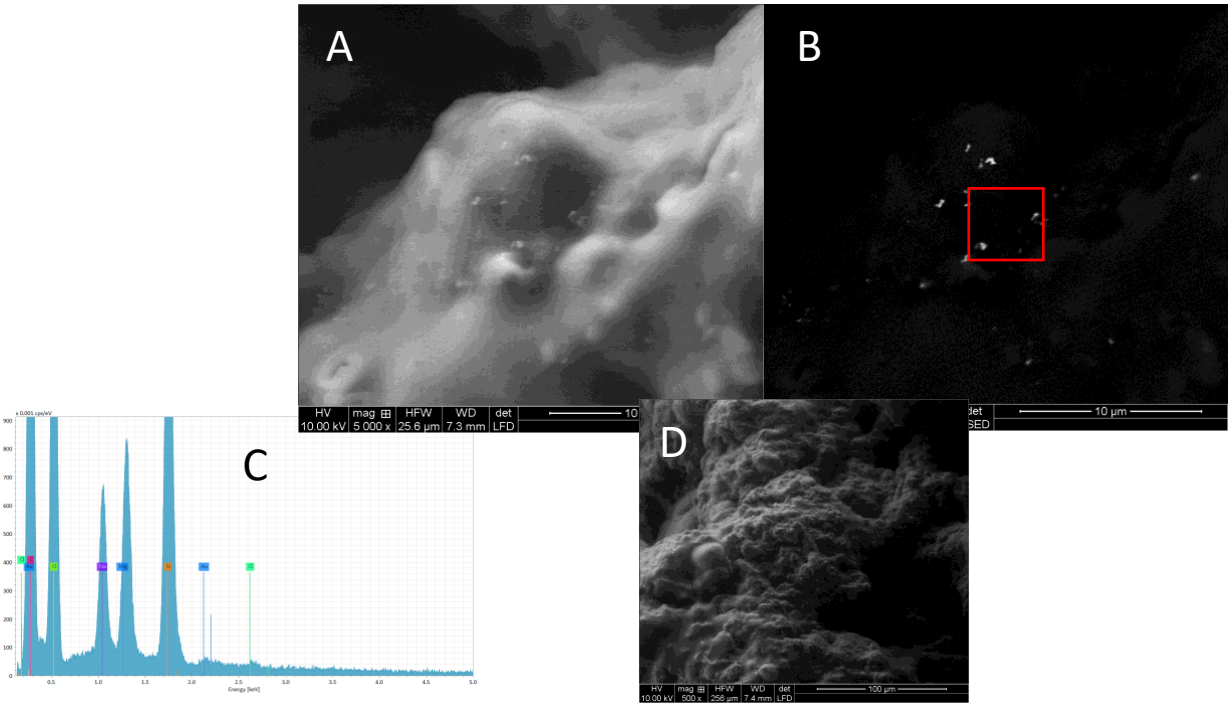

Figure 3.2. SEM and EDS analysis of HT conjugated with 20 nm AuNPs and supplemented with 6% curcumin. (A) Scattering electron image on the surface of HT with conjugated AuNPs. (B) Backscattered electron image of AuNPs, red box shows spot where EDS spectra was acquired. (C) EDS spectra of HT with curcumin. (D) Scattering electron image on the surface of HT with curcumin.

3.4.2 Injection Force Study

To determine injectability of the HT, maximum compressive force was analyzed. 6% homogenized porcine diaphragm tissue was added to various concentrations of HA to determine the effect of HA on the injectability. The data is summarized in Table 3.1. All concentrations of HA were well below 1 N of force required to inject. The sample that required the most force was the PBS sample

with no HA which required 0.75 N. The sample that required the least force was the 25% HA sample.

Table 3.1 Max extrusion force data for HT supplemented with multiple concentrations of HA ejected through a 22-gauge cannula.

	Max Compressive Force (N)	Standard Deviation (±)
PBS	0.75	0.07
10% HA	0.70	0.06
15% HA	0.60	0.06
20% HA	0.63	0.11
25% HA	0.57	0.24

3.4.3 Release Rate of Curcumin

The release of curcumin from the HT into its environment was analyzed using a UV-Vis spectrophotometer at 420 nm over 9 days. Figure 3.3 demonstrates the release profile. The bulk of curcumin is released in the span of 2-days in incubation with minimal release post 2-days. The AuNP & curcumin sample appears to have a slower release over time with an increased release of curcumin between day 6 and day 8. HT was used as the control along with HT conjugated with AuNPs.

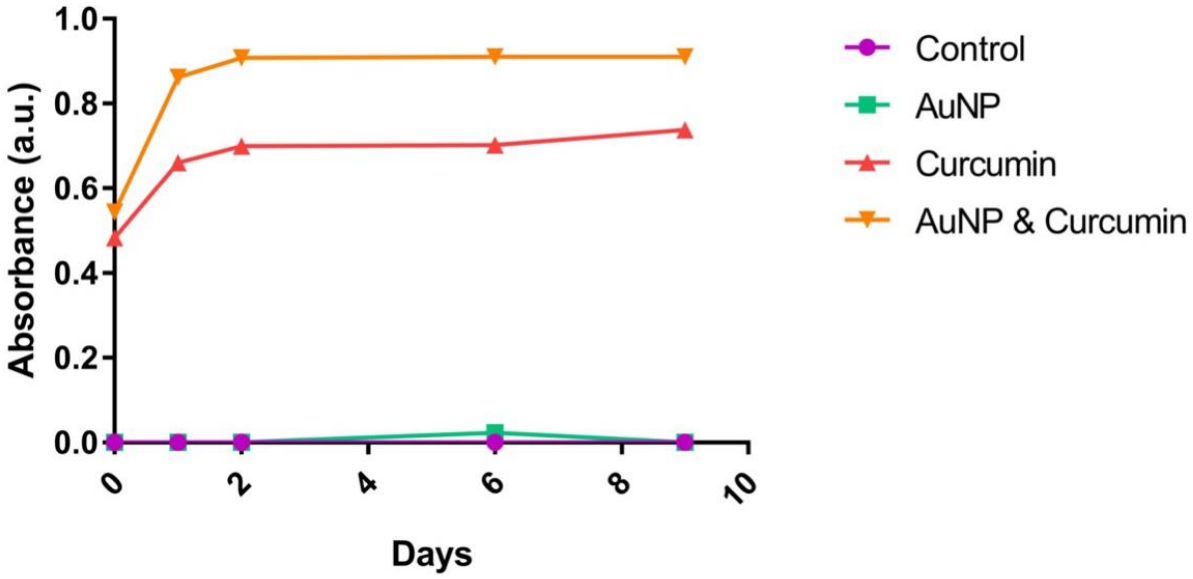

Figure 3.3. Release of 4% curcumin from HT and also HT supplemented with 20 nm AuNPs was observed using UV-Vis spectroscopy. As a baseline, HT and HT supplemented with 20 nm AuNPs were also tested.

3.4.4 Differential Scanning Calorimetry

Differential scanning calorimetry was used to determine the denaturization temperature of the HT. Figure 3.4 shows the results of the study. The crosslinked control denatured at 37°C. Conjugation of AuNPs increased the denaturization temperature of the tissue to 39°C and the addition of curcumin further increased the denaturization temperature creating a more stable scaffold. Increasing concentrations of curcumin also increased the stability of the scaffolds. 2% curcumin increased the denaturization point to 46°C, 4% curcumin correlated to 48°C, and 6% curcumin denaturizations temperature was at 50°C.

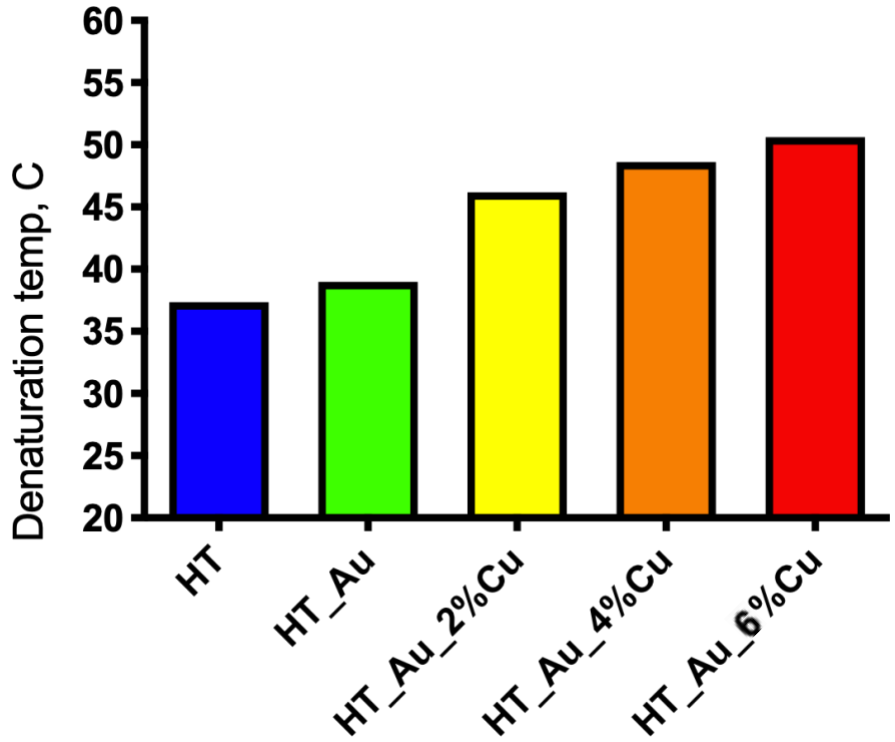

Figure 3.4. DSC analysis on HT supplemented with 20 nm AuNP and multiple concentrations of curcumin.

3.4.5 L929 Fibroblast Studies

3.4.5.1 WST-1 Assay

A WST-1 cellular viability study was used to determine how the HT interacted with murine L929 fibroblast cells over 3 days. Results can be observed in Figure 3.5. The addition of AuNPs to the HT increased cellular activity. The addition of curcumin with AuNPs further increased the overall viability. The 4% curcumin with AuNPs performed the best in this study.

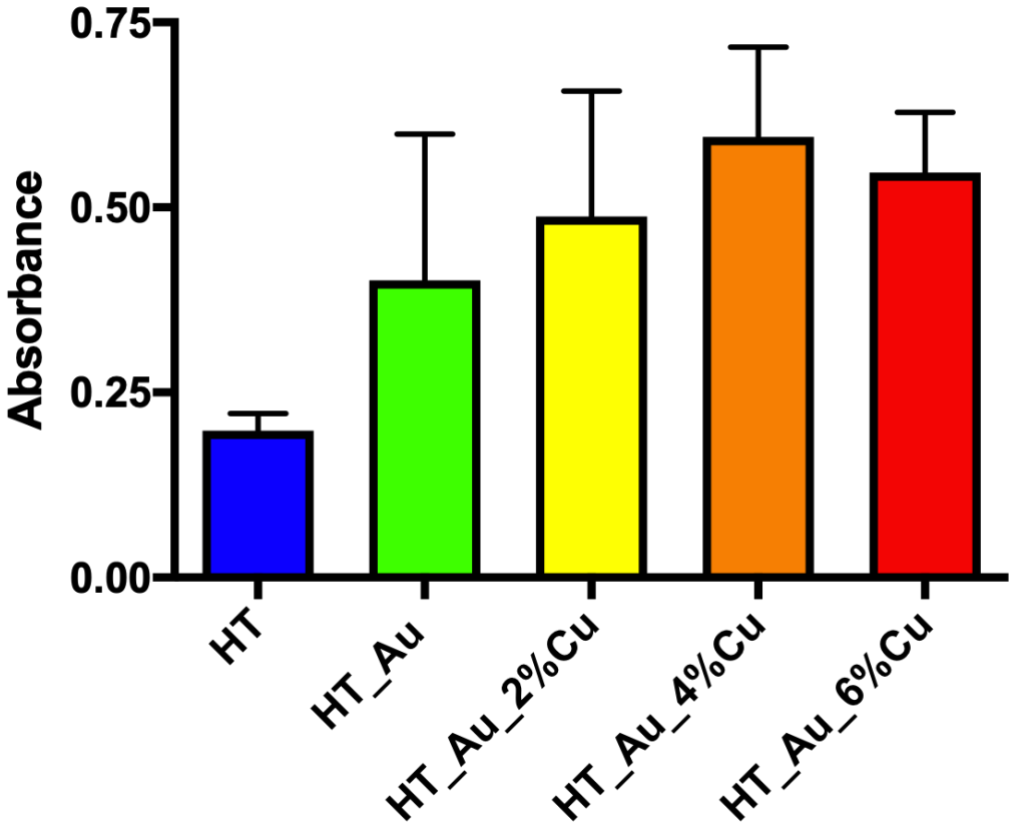

Figure 3.5. 3-day WST-1 assay analyzing cellular viability of L929 fibroblast cells with HT supplemented with 4x 20 nm AuNPs and various concentrations of curcumin. (n=3)

3.4.5.2 ROS Assay

An OxiSelect ROS assay was used to determine ROS production by the L929 fibroblast cells. 4% curcumin was chosen due to the previous WST-1 study. From Figure 3.6, both HT with AuNPs and HT with 4% curcumin + AuNPs performed better than the control sample. Curcumin did appear to have a large effect on ROS production. In the case of using 6% curcumin it in fact decreased ROS production. A significant reduction in ROS was observed with the combinatorial use of 1x AuNPs and curcumin.

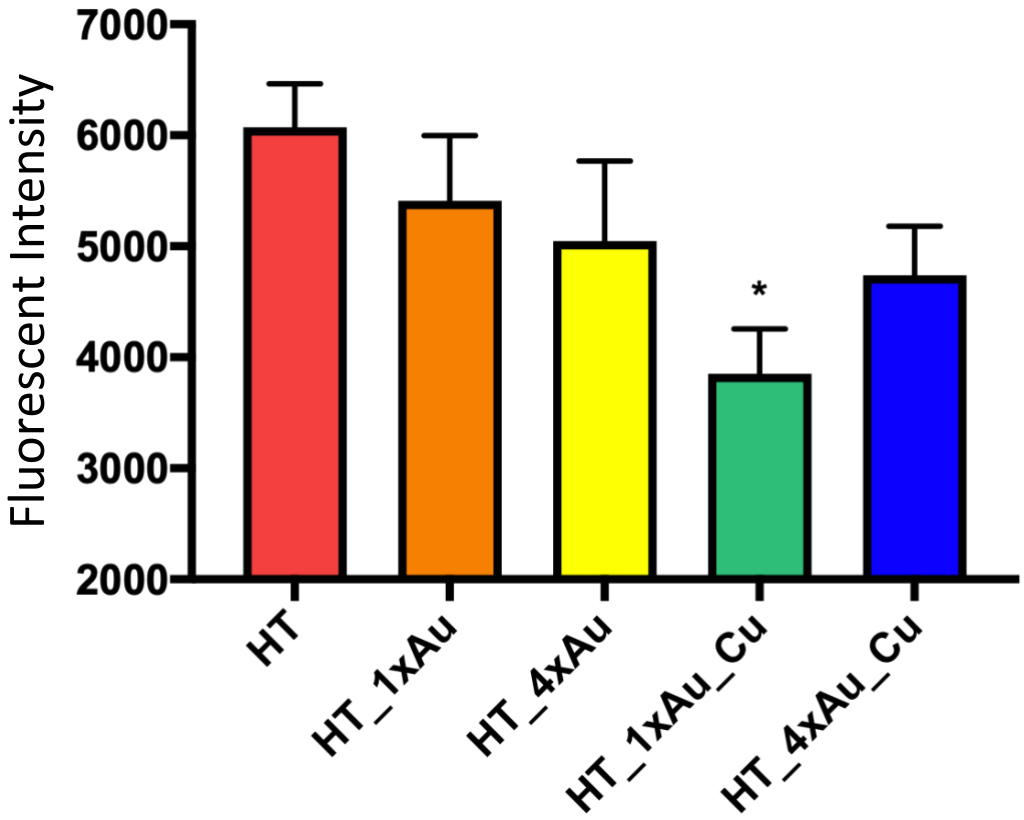

Figure 3.6. ROS assay analyzing ROS production by L929 fibroblast cells with HT supplemented with 1x and 4x 20 nm AuNPs and with 4% curcumin. * = P ≤ 0.05 compared to HT; (n=4)

3.4.6 Synovial Fibroblast Study

3.4.6.1 ROS Assay

Another OxiSelect ROS assay was used to examine ROS production from equine synovial fibroblast cells when introduced to the HT. A comparison in ROS production between lyophilized samples and non-lyophilized samples was studied along with AuNP conjugation in Figure 3.7. From the previous study 1x AuNPs performed the best so it was used exclusively for this study. When comparing samples without AuNPs the lyophilized samples outperformed the non-lyophilized sample with 4% lyophilized samples performing the best. The 7% lyophilized with 4x AuNPs performed the best of all groups. An overall decrease

in ROS can be observed with AuNP lyophilized samples decreasing ROS with increased tissue concentration.

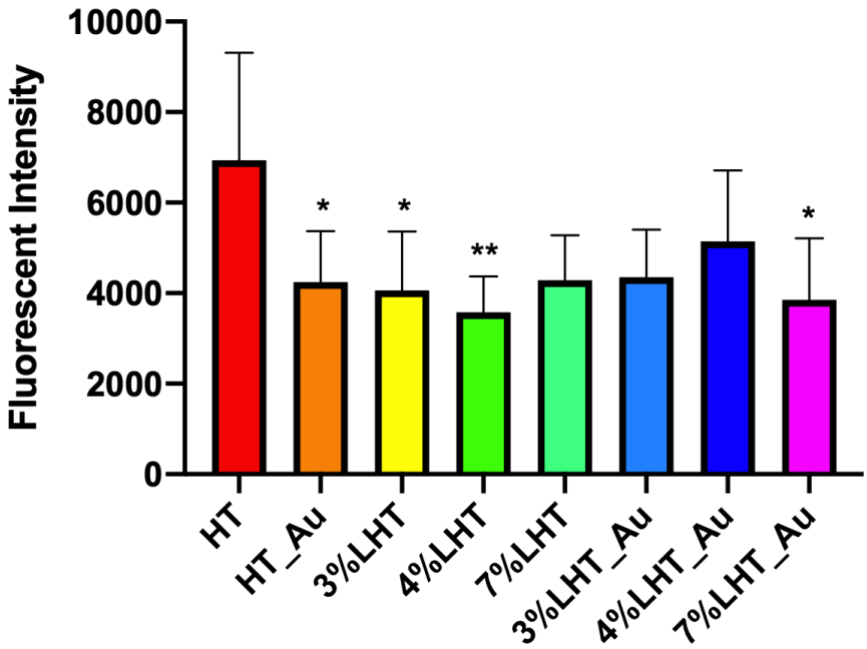

Figure 3.7. ROS assay analyzing ROS production by equine synovial fibroblast cells with HT and various concentrations of LHT supplemented with 4x 20 nm AuNPs. * = P ≤ 0.05 compared to HT; ** = P ≤ 0.01 compared to HT; (n=5)

3.4.7 HCH Human Chondrocyte Studies

3.4.7.1 WST-1 Assay

A cell viability study was performed to determine how human chondrocyte cells interacted with the homogenized scaffolds in Figure 3.8. The interaction was studied at 3, 5, and 10-day time points. At 3-days the scaffolds with 4x AuNPs appeared to be the most metabolically active relative to all other groups. At 5-days, the 1x AuNPs homogenized scaffolds appeared to stimulate chondrocyte activity relative to the other groups. The 4x AuNP scaffolds had a reduced viability at 5-days as well. At 10-days, the samples with curcumin were the most metabolically active. The 1x AuNP with curcumin performed the best at 10-days followed by the 4x AuNP with curcumin.

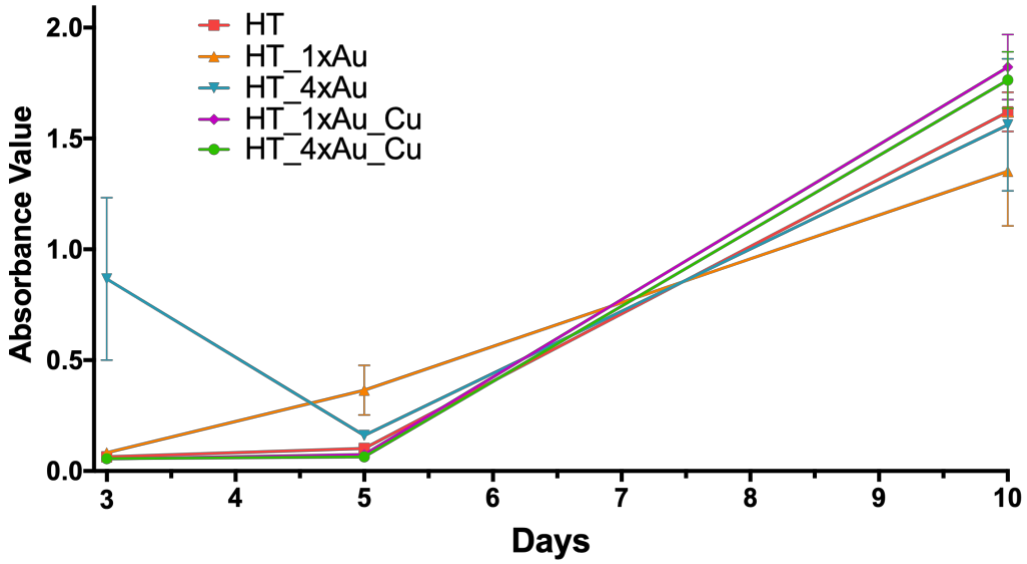

Figure 3.8. 3, 5, 10-day WST-1 assay analyzing cellular viability of HCH human chondrocyte cells with HT supplemented with 1x and 4x 20 nm AuNPs and 4% curcumin. (n=5)

Another cell viability study examined the addition of HA to the HT as shown in Figure 3.9. 3 and 6-day time points were used in this study with chondrocyte cells. At 3 days the HT supplemented with HA had the highest cell viability. While at 6-days a significant increase in the HT supplemented with HA and AuNPs was observed. Correlating the change in viability between 3 and 6-days from the HT supplemented with AuNPs and the significant increase in viability with the HT supplemented with HA and AuNPs, the combinatorial use of AuNPs with the HA may be helping to elicit such an increase in viability. Each of the samples displayed an increase in cellularity over time, with the HT_Au_HA sample displaying a 1516% change from the 3 to 6 day as well as a significant change as compared to the control. The HT_Au group also displayed a 1304% increase from 3 to 6 days while the HT and HT_HA groups had a 163% and 136% increase respectively.

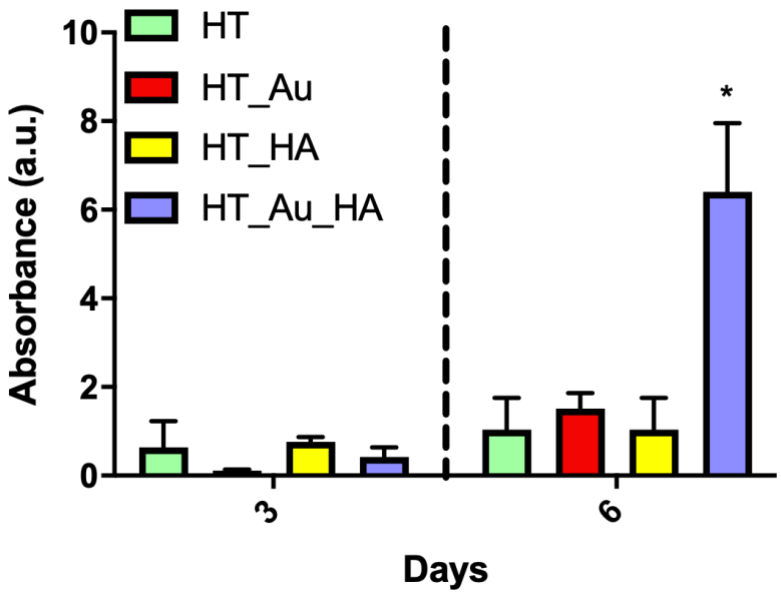

Figure 3.9. 3 and 6-day WST-1 assay analyzing cellular viability of HCH human chondrocyte cells with HT supplemented with 4x 20 nm AuNPs and 15% HA. * = P ≤ 0.05 compared to all other groups; (n=4)

3.4.7.2 ROS Assay

An ROS assay was performed to study how the homogenized scaffolds performed by reducing intracellular ROS when introduced to human chondrocyte cells in Figure 3.10. 4x AuNPs, 6% (w/v) curcumin, and hyaluronic acid were all studied. There was a synergistic correlation with ROS production and the addition of AuNPs, HA and curcumin to the chondrocyte cells. Each AuNPs, HA, and curcumin individually lowered overall ROS relative to the control sample. Each permutation of additives also lowered ROS. The lowest ROS was produced when AuNPs, HA, and curcumin were all added to the homogenized scaffold.

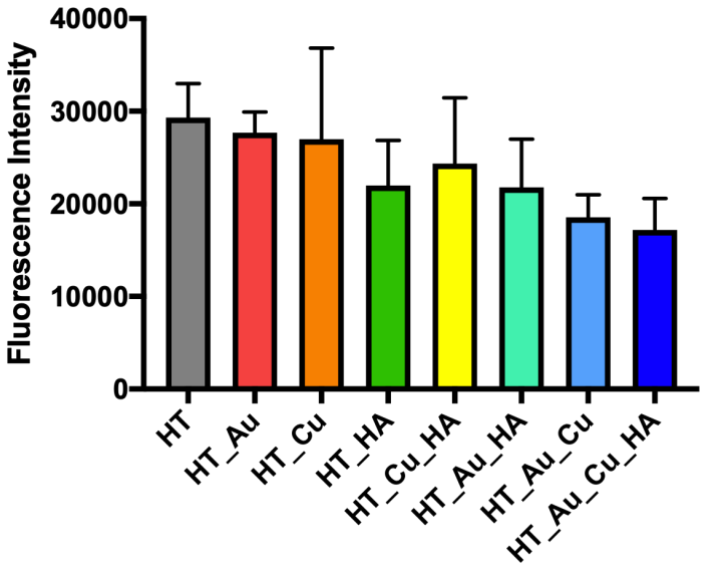

Figure 3.10. ROS assay analyzing ROS production by HCH human chondrocyte cells with HT supplemented with 4x 20 nm AuNPs, 4% curcumin, and 15% HA. (n=5)

3.4.7.3 Apoptosis Assay

Finally, a HT TiterTACS assay kit was used to observe how the homogenized scaffolds affected apoptosis of human chondrocyte cells when stimulated by IL-1β (10 ng/ml) as shown in in Figure 3.11. Cells were incubated with IL-1β for 24 hours prior to addition of homogenized scaffolds. The same AuNP, HA, and curcumin homogenized scaffold from the previous ROS assay was used due to its synergistic reduction in ROS. A reduction in apoptosis was

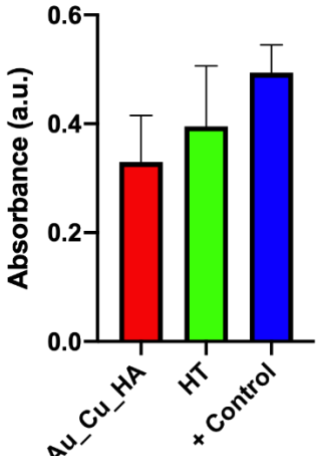

Figure 3.11. Apoptosis assay analyzing the chondroprotective ability of HT supplemented with 4x 20 nm AuNPs, 4% curcumin, and 15% HA. (n=3)

observed with the combinatorial addition of AuNP, HA, and curcumin relative to the crosslinked and uncrosslinked homogenized scaffold.

3.5 Discussion

Porcine diaphragm tissue was decellularized and homogenized using a blade homogenizer. The HT was then conjugated with 20 nm AuNPs using EDC/NHS chemistry. Additives such as curcumin and HA were also integrated after AuNP conjugation. The injectable material was characterized using SEM/EDS analysis to confirm AuNP conjugation to the HT, injectability studies to verify its ease of injectability, release profile of curcumin, thermal stability, and viscoelastic analysis. *In vitro* analysis was also utilized to determine the biocompatibility, reduction in ROS, and chondroprotective effectiveness of the HT.

A balance of a stable scaffold and host remodeling of the scaffold is advantageous and is generally the goal of biologic scaffolds. Heavily crosslinked scaffolds can prevent remodeling by preventing cellular integration and can create a chronic host response[28]. A porous scaffold provides an open conformation for cellular integration allowing for host remodeling. Thus SEM and EDS analysis were utilized to verify the conjugation of AuNPs to the HT using EDC/NHS chemistry and also observing the tissue structure. Backscattered electron images, Figure 3.1B & 3.2B, both show AuNPs conjugated to the tissue scaffolds. EDS analysis, Figure 3.1C & 3.2C, are EDS spectra from their respective red box in Figure 3.1B & 3.2B. Figure 3.1C & 3.2C have clear Au

peaks at 2.120 KeV confirming the presence of AuNPs within the scaffolds. Figure 3.1D provides evidence of the HT having an open porous extracellular matrix structure appearing to be minimally altered in the decellularization and crosslinking process.

DSC analysis was also utilized to determine the extent of crosslinking in altering the overall thermal stability and structure of the HT scaffolds as shown in in Figure 3.4. The addition of AuNPs to the scaffolds increased the thermal stability of all scaffolds supplemented with Au. Samples supplemented with curcumin also increased thermal stability with 2%, 4%, and 6% curcumin with AuNPs increasing stability with increased concentrations of curcumin. Conjugation of AuNPs to HT will not only covalently crosslink AuNPs to the HT but the use of EDC/NHS crosslinking will also crosslink the HT. However, by correlating Figure 3.1D to these results, an open microstructure has been maintained while increasing the stability of the scaffold. Possessing increased thermal stability creates a scaffold more resistant to degradation resulting in a more stable scaffold that can slow down *in vivo* enzymatic degradation allowing more time for tissue recapitulation [29-34].

Extrusion force is an important factor for clinicians when injecting therapeutics. If the force required to inject a therapeutic is too high it could further injure the patient. Table 3.1 shows the maximum compressive force required to extrude the HT integrated with various concentrations of HA. A commonly used 22-gauge cannula for orthopedic injections was used in this study [35, 36]. All of the HA compositions required less than 1 N of force to extrude. A study by Kim et

al developed a collagen/HA injectable composite filler which required 10-12 N of force to extrude through a 27-gauge cannula [37]. Another study by Cao et al developed an injectable HA composite requiring 2 N of force to extrude through a 26-gauge cannula [38]. In comparison, our HT injectable required less force than either published HA composite making it well suited for injection.

Since modulating inflammatory response is a key factor in mitigating the progression of PTOA, we incorporated curcumin in the homogenized tissue as an anti-inflammatory agent. Understanding how a biomodulatory agent like curcumin releases into its environment can be important in identifying how it interacts within the environment. A release profile of 6% (w/v) curcumin was determined by UV-Vis spectroscopy as shown in Figure 3.3. Most of the curcumin released over a 2-day time period, but more curcumin appeared to be loaded into HT conjugated with AuNPs relative to HT alone. It is possible that the curcumin adsorbed onto the surface of the AuNPs increasing the loading capacity of the homogenized tissue. To achieve a longer release rates, curcumin may need to be conjugated to the homogenized tissue and then released as the tissue is slowly broken down via enzymatic degradation. This is an important factor to keep in mind when translating this injectable therapy into *in vitro* or *in vivo* work; an increased therapeutic load of curcumin with the conjugated tissue could adversely alter biologic effects *in situ;* thus, zero-order, sustainable release profiles are needed.

Cellular viability studies were conducted in order to examine the effects of AuNPs and curcumin on biocompatibility of the HT. Initial work with murine L929

fibroblast cells was conducted to obtain an understanding of how the HT interact with the cells. A 3-day WST-1 assay was utilized to determine the biocompatibility of the HT supplement with AuNPs and curcumin as shown in Figure 3.5. Prior work by Smith et al provided evidence that a 4x 20 nm AuNP concentration maintained biocompatibility, improved cellular migration, and reduced ROS in L929 fibroblast cells so that concentration was used in this study [9]. Crosslinked tissue scaffolds served as the control in this study to determine the benefit of conjugating AuNPs and supplementing with curcumin. As can be observed, the addition of AuNPs increased the viability of the scaffolds. The viability of the scaffolds were further increased with increasing concentrations of curcumin. A 4% curcumin with AuNPs had the highest overall biocompatibility of all studied groups. This may be due to the cells being attracted to the higher surface energy of the AuNPs [26] and then combined with a natural anti-inflammatory agent, curcumin, resulted in enhanced biocompatibility. It was concluded that the supplementation of both AuNPs and curcumin had a superior effect on cellular viability relative to the unsupplemented scaffold.

There has been published research about the cytotoxicity of AuNPs [39-41]. For example, it has been reported that the uptake of AuNPs by cells can lead to cell death [42, 43]. However, in our studies, we did not observe cytotocixity. By conjugating AuNPs to the homogenized tissue and through the judicious selection of AuNP size, we are able to prevent cellular uptake of the free AuNPs and thus mitigating the concern of cell death.

To determine if the AuNPs and curcumin had an anti-inflammatory effect, which could then enhance biocompatibility, we performed ROS assays. In this study, we again utilized L929 fibroblast cells and examined ROS production with the introduction of the supplemented HT as shown in Figure 3.6. Again, the control was a crosslinked tissue scaffold. In this study a 1x AuNP concentration decreased ROS relative to the control scaffold while the 4x AuNP concentration demonstrated a further decrease in ROS concentration as compared to the control. A reduction in ROS was observed with the addition of curcumin to the 1x AuNP HT that resulted in a significant difference as compared to the control. The addition of curcumin to the 4x AuNP HT resulted in only a slight decrease in ROS production as compared to 4x AuNP HT. Both the curcumin and AuNPs appeared to play a role in the reduction of ROS production, but it is possible that it may be cell dependent or processing dependent.

A second ROS study was then performed with more cellular relevant cells that would be involved during a PTOA event. Equine synovial fibroblast cells were used to study ROS production with the scaffolds as shown in Figure 3.7. In addition, this study examined how lyophilization of the HT and various concentrations of tissue could affect ROS production. A significant reduction in ROS was observed through conjugation of 4x AuNPs. There was also a significant reduction of ROS with the 3% lyophilized, 4% lyophilized, and 7% lyophilized + AuNPs relative to HT only. Interestingly, while 3% and 4% lyophilized with AuNPs did demonstrate a reduction compared to HT only, it was not significant. This may be due to 7% lyophilized tissue having enough volume

of tissue (and thus AuNPs) to provide a therapeutic dose of AuNPs while the 3% and 4% lyophilized tissue did not.

Like the synovial fibroblast cells, human chondrocyte cells were used to provide a more physiologically relevant examination as to how the HT would perform in an articular environment. Two WST-1 assays were employed to examine how the scaffolds performed with the chondrocyte cells. The first assay examined 1x & 4x AuNP concentrations with and without 6% (w/v) curcumin over a 10-day period as shown in Figure 3.8. At 3-days the 4x AuNP scaffold appeared to have significantly better viability than all other scaffolds. At 5-days, the 4x AuNP scaffolds regressed in viability but still maintain high viability. The 1x AuNPs showed a steady, strong increase in cellular viability over time. At 10-days, the scaffolds with curcumin demonstrated good viability with the highest cellular viability being achieved with the 1x AuNP with curcumin. Overall, the HT with AuNPs and with/without curcumin demonstrated good viability with the synovial fibroblast cells. No cytotoxic effects were observed.

With HA being a major component of the synovium and found throughout the articular cartilage, HA was added to the HT to determine how it interacted with chondrocytes at 3 and 6 days in Figure 3.9. At 3-days the HT with HA performed slightly better than the other scaffolds, but there was no statistical significant difference. However, at 6-days the 4x AuNP + HA HT significantly increased cell viability. A large increase in viability was also observed by the AuNP HT. These results indicate that there may be a synergistic, complementary effect between the AuNPs and HA, that the cells are adapting and binding to the

AuNPs in this more cell friendly HA environment. Additionally it is possible that there is a delayed metabolic response from the chondrocyte cells between day 3 and day 6 two time points. The results of the WST studies demonstrate the biocompatibility of utilizing AuNPs, curcumin, and HA although concentration of the AuNPs and curcumin will affect the viability of the cells.

High levels of ROS production are a hallmark of PTOA [44-46]. ROS production in PTOA is derived from chondrocyte cells after a mechanical stress has been imparted on the articular cartilage with the production of ROS leading to cellular apoptosis and breakdown of articular cartilage [47, 48]. To determine the ROS mitigating potential of the HT, another ROS assay was used to study the interaction of human chondrocyte cells stimulated with IL-1β as shown in Figure 3.10. IL-1β is used to stimulate a simulated osteoarthric state by the chondrocyte cells 24-hours prior to adding the HT [49-51]. For this study a permutation of all groups including AuNP, curcumin, and HA were all observed. Each HT group supplemented with either AuNP, curcumin, or HA reduced ROS production relative to the control group. Interestingly the combination of AuNP & HA along with AuNP & curcumin both further reduced ROS in comparison to the individual supplementations of AuNP, curcumin, or HA. The supplementation of AuNP, curcumin, and HA together demonstrated the highest reduction of ROS. Explanation for this observation is that there appears to be synergetic, complementary effect with these supplements when taken in combination. However, optimizing of the amounts of each supplement needs to be determine in order to achieve the optimal effects.

The apoptosis assay was performed to in order to examine the chondro-protective ability of the scaffolds in preventing programmed cell death of the chondrocytes as shown in Figure 3.11. IL-1β was incubated with chondrocyte cells 24-hours prior to addition of the HT to simulate an osteoarthric chondrocyte cell environment. Leveraging the results from the previous ROS study, the HT supplemented with AuNPs, curcumin, and HA were compared to HT unsupplemented. A reduction in chondrocytic apoptosis by the fully supplemented HT can be observed relative to the unsupplemented scaffold. The unsupplemented scaffold also appeared to have some chondroprotective ability in comparison to the positive control as well. This study provided evidence that the addition of HT to damaged chondrocyte cells may aid in protecting cells from programmed cell death. Examining the results of the ROS assay and apoptosis assay using the chondrocyte cells, there is evidence that by introducing the HT supplemented with AuNPs, curcumin, and HA have the ability to reduce intracellular ROS and also prevent chondrocyte cells from programmed cell death. These two factors are necessary in mitigating PTOA progression. By mitigating cellular apoptosis, chondrocyte cells have the ability to survive the catabolic PTOA environment. By reducing intracellular ROS, the chondrocyte cells have the opportunity to return to their homeostatic regulation mechanisms which may possibly regulate and maintain articular cartilage.

3.6 Conclusions

We have demonstrated an injectable homogenized porcine diaphragm tissue scaffold supplemented with AuNPs, curcumin, and HA that may have applications in mitigating progression of PTOA. Conjugation of AuNPs to the HT were successful with further validation of the scaffold by injectability studies, release rate, and thermal stability studies. In vitro analysis was validated using cell viability, ROS, and apoptosis studies with murine fibroblast, equine synovial fibroblast, and human chondrocyte cells. HT supplement with AuNPs, curcumin, and HA have the best potential of being utilized for PTOA application with the ROS mitigating and chondroprotection results.

3.7 References

1. Yi, S., et al., *Extracellular matrix scaffolds for tissue engineering and regenerative medicine.* Current stem cell research & therapy, 2017. **12**(3): p. 233-246.

2. Rana, D., et al., *Development of decellularized scaffolds for stem cell-driven tissue engineering.* Journal of tissue engineering and regenerative medicine, 2017. **11**(4): p. 942-965.

3. Gallie, D.R., W.J. Lucas, and V. Walbot, *Visualizing mRNA expression in plant protoplasts: factors influencing efficient mRNA uptake and translation.* The Plant Cell, 1989. **1**(3): p. 301-311.

4. Brown, B.N., et al., *Macrophage polarization: an opportunity for improved outcomes in biomaterials and regenerative medicine.* Biomaterials, 2012. **33**(15): p. 3792-3802.

5. Valentin, J.E., et al., *Macrophage participation in the degradation and remodeling of extracellular matrix scaffolds.* Tissue Engineering Part A, 2009. **15**(7): p. 1687-1694.

6. Calve, S., S.J. Odelberg, and H.-G. Simon, *A transitional extracellular matrix instructs cell behavior during muscle regeneration.* Developmental biology, 2010. **344**(1): p. 259-271.

7. Vorotnikova, E., et al., *Extracellular matrix-derived products modulate endothelial and progenitor cell migration and proliferation in vitro and stimulate regenerative healing in vivo.* Matrix Biology, 2010. **29**(8): p. 690-700.

8. Ott, H.C., et al., *Perfusion-decellularized matrix: using nature's platform to engineer a bioartificial heart.* Nat Med, 2008. **14**(2): p. 213-221.

9. Smith, S.E., et al., *Homogenized porcine extracellular matrix derived injectable tissue construct with gold nanoparticles for musculoskeletal tissue engineering applications.* Journal of Biomaterials and Nanobiotechnology, 2017. **8**(02): p. 125.

10. Goldring, M.B. and S.R. Goldring, *Articular cartilage and subchondral bone in the pathogenesis of osteoarthritis.* Annals of the New York Academy of Sciences, 2010. **1192**(1): p. 230-237.

11. Kapoor, M., et al., *Role of proinflammatory cytokines in the pathophysiology of osteoarthritis.* Nature Reviews Rheumatology, 2010. **7**: p. 33.

12. Gouze, J.N., et al., *Interleukin-1β down-regulates the expression of glucuronosyltransferase I, a key enzyme priming glycosaminoglycan biosynthesis: Influence of glucosamine on interleukin-1β–mediated effects in rat chondrocytes.* Arthritis & Rheumatism: Official Journal of the American College of Rheumatology, 2001. **44**(2): p. 351-360.

13. Stöve, J., et al., *Interleukin-1β induces different gene expression of stromelysin, aggrecan and tumor-necrosis-factor-stimulated gene 6 in human osteoarthritic chondrocytes in vitro.* Pathobiology, 2000. **68**(3): p. 144-149.

14. Shakibaei, M., et al., *Curcumin protects human chondrocytes from IL-1β-induced inhibition of collagen type II and β1-integrin expression and activation of caspase-3: an immunomorphological study.* Annals of Anatomy-Anatomischer Anzeiger, 2005. **187**(5-6): p. 487-497.

15. Chadjichristos, C., et al., *Sp1 and Sp3 transcription factors mediate interleukin-1β down-regulation of human type II collagen gene expression in articular chondrocytes.* Journal of Biological Chemistry, 2003. **278**(41): p. 39762-39772.

16. Holmes, M., M. Bayliss, and H. Muir, *Hyaluronic acid in human articular cartilage. Age-related changes in content and size.* Biochemical Journal, 1988. **250**(2): p. 435-441.

17. Shaharudin, A. and Z. Aziz, *Effectiveness of hyaluronic acid and its derivatives on chronic wounds: a systematic review.* Journal of wound care, 2016. **25**(10): p. 585-592.

18. Belkacemi, A., et al., *Challenges associated with curcumin therapy in Alzheimer disease.* Expert reviews in molecular medicine, 2011. **13**.

19. Hanai, H., et al., *Curcumin maintenance therapy for ulcerative colitis: randomized, multicenter, double-blind, placebo-controlled trial.* Clinical Gastroenterology and Hepatology, 2006. **4**(12): p. 1502-1506.

20. Singh, S. and A. Khar, *Biological effects of curcumin and its role in cancer chemoprevention and therapy.* Anti-Cancer Agents in Medicinal Chemistry (Formerly Current Medicinal Chemistry-Anti-Cancer Agents), 2006. **6**(3): p. 259-270.

21. Bharti, A.C., et al., *Curcumin (diferuloylmethane) down-regulates the constitutive activation of nuclear factor–κB and IκBα kinase in human multiple myeloma cells, leading to suppression of proliferation and induction of apoptosis.* Blood, 2003. **101**(3): p. 1053-1062.

22. Shakibaei, M., et al., *Suppression of NF-κB activation by curcumin leads to inhibition of expression of cyclo-oxygenase-2 and matrix*

metalloproteinase-9 in human articular chondrocytes: Implications for the treatment of osteoarthritis. Biochemical Pharmacology, 2007. **73**(9): p. 1434-1445.

23. Ionita, P., F. Spafiu, and C. Ghica, *Dual behavior of gold nanoparticles, as generators and scavengers for free radicals.* Journal of materials science, 2008. **43**(19): p. 6571-6574.

24. Cozad, M.J., S.L. Bachman, and S.A. Grant, *Assessment of decellularized porcine diaphragm conjugated with gold nanomaterials as a tissue scaffold for wound healing.* Journal of Biomedical Materials Research Part A, 2011. **99**(3): p. 426-434.

25. Grant, S., et al., *A comparative study of the remodeling and integration of a novel AuNP-tissue scaffold and commercial tissue scaffolds in a porcine model.* Journal of Biomedical Materials Research Part A, 2013. **101**(10): p. 2778-2787.

26. Christenson, E.M., et al., *Nanobiomaterial applications in orthopedics.* Journal of Orthopaedic Research, 2007. **25**(1): p. 11-22.

27. Grant, S.A., et al., *Assessment of the biocompatibility and stability of a gold nanoparticle collagen bioscaffold.* Journal of Biomedical Materials Research Part A: An Official Journal of The Society for Biomaterials, The Japanese Society for Biomaterials, and The Australian Society for Biomaterials and the Korean Society for Biomaterials, 2014. **102**(2): p. 332-339.

28. Delgado, L.M., et al., *To cross-link or not to cross-link? Cross-linking associated foreign body response of collagen-based devices.* Tissue Engineering Part B: Reviews, 2015. **21**(3): p. 298-313.

29. Yannas, I., et al., *Correlation of in vivo collagen degradation rate with in vitro measurements.* Journal of biomedical materials research, 1975. **9**(6): p. 623-628.

30. Weadock, K.S., et al., *Physical crosslinking of collagen fibers: comparison of ultraviolet irradiation and dehydrothermal treatment.* Journal of biomedical materials research, 1995. **29**(11): p. 1373-1379.

31. Lee, C., A. Grodzinsky, and M. Spector, *The effects of cross-linking of collagen-glycosaminoglycan scaffolds on compressive stiffness, chondrocyte-mediated contraction, proliferation and biosynthesis.* Biomaterials, 2001. **22**(23): p. 3145-3154.

32. Pek, Y., et al., *Degradation of a collagen–chondroitin-6-sulfate matrix by collagenase and by chondroitinase.* Biomaterials, 2004. **25**(3): p. 473-482.

33. Haugh, M.G., M.J. Jaasma, and F.J. O'Brien, *The effect of dehydrothermal treatment on the mechanical and structural properties of collagen-GAG scaffolds.* Journal of Biomedical Materials Research Part A: An Official Journal of The Society for Biomaterials, The Japanese Society for Biomaterials, and The Australian Society for Biomaterials and the Korean Society for Biomaterials, 2009. **89**(2): p. 363-369.

34. Charulatha, V. and A. Rajaram, *Influence of different crosslinking treatments on the physical properties of collagen membranes.* Biomaterials, 2003. **24**(5): p. 759-767.

35. Jackson, D.W., N.A. Evans, and B.M. Thomas, *Accuracy of needle placement into the intra-articular space of the knee.* JBJS, 2002. **84**(9): p. 1522-1527.

36. Monseau, A.J. and P.S. Nizran, *Common injections in musculoskeletal medicine.* Primary Care: Clinics in Office Practice, 2013. **40**(4): p. 987-1000.

37. Kim, Z.-H., et al., *A composite dermal filler comprising cross-linked hyaluronic acid and human collagen for tissue reconstruction.* J Microbiol Biotechnol, 2015. **25**(3): p. 399-406.

38. Cao, W., et al., *The preparation and biocompatible evaluation of injectable dual crosslinking hyaluronic acid hydrogels as cytoprotective agents.* Journal of Materials Chemistry B, 2019. **7**(28): p. 4413-4423.

39. Malugin, A. and H. Ghandehari, *Cellular uptake and toxicity of gold nanoparticles in prostate cancer cells: a comparative study of rods and spheres.* Journal of Applied Toxicology: An International Journal, 2010. **30**(3): p. 212-217.

40. Goodman, C.M., et al., *Toxicity of gold nanoparticles functionalized with cationic and anionic side chains.* Bioconjugate chemistry, 2004. **15**(4): p. 897-900.

41. Pan, Y., et al., *Gold nanoparticles of diameter 1.4 nm trigger necrosis by oxidative stress and mitochondrial damage.* small, 2009. **5**(18): p. 2067-2076.

42. Khlebtsov, N. and L. Dykman, *Biodistribution and toxicity of engineered gold nanoparticles: a review of in vitro and in vivo studies.* Chemical Society Reviews, 2011. **40**(3): p. 1647-1671.

43. Chithrani, B.D., A.A. Ghazani, and W.C. Chan, *Determining the size and shape dependence of gold nanoparticle uptake into mammalian cells.* Nano letters, 2006. **6**(4): p. 662-668.

44. O'Grady, K.P., et al., *Drug-free ROS sponge polymeric microspheres reduce tissue damage from ischemic and mechanical injury.* ACS biomaterials science & engineering, 2017. **4**(4): p. 1251-1264.

45. Halliwell, B., *Free radicals and other reactive species in disease.* e LS, 2001.

46. Sarban, S., et al., *Plasma total antioxidant capacity, lipid peroxidation, and erythrocyte antioxidant enzyme activities in patients with rheumatoid arthritis and osteoarthritis.* Clinical biochemistry, 2005. **38**(11): p. 981-986.

47. Henrotin, Y., P. Bruckner, and J.-P. Pujol, *The role of reactive oxygen species in homeostasis and degradation of cartilage.* Osteoarthritis and cartilage, 2003. **11**(10): p. 747-755.

48. Afonso, V., et al., *Reactive oxygen species and superoxide dismutases: role in joint diseases.* Joint bone spine, 2007. **74**(4): p. 324-329.

49. Johnson, C.I., D.J. Argyle, and D.N. Clements, *In vitro models for the study of osteoarthritis.* The Veterinary Journal, 2016. **209**: p. 40-49.

50. Sylvester, J., et al., *Interleukin-1 induction of aggrecanase gene expression in human articular chondrocytes is mediated by mitogen-activated protein kinases.* Cellular Physiology and Biochemistry, 2012. **30**(3): p. 563-574.

51. Novakofski, K.D., C.J. Torre, and L.A. Fortier, *Interleukin-1α,-6, and-8 decrease Cdc42 activity resulting in loss of articular chondrocyte phenotype.* Journal of Orthopaedic Research, 2012. **30**(2): p. 246-251.

Chapter Four

INVESTIGATING PARAMETERS OF PCL/LECITHIN ELECTROSPUN NANOFIBERS FOR IMPROVED REPRODUCIBILITY

4.1 Introduction

Articular cartilage injuries such as osteoarthritis (OA) is a joint degenerative disease wherein the articular cartilage on the end of bones progressively degrade over the lifespan of a patient and eventually can lead to bone-on-bone articulation rendering the patient unable to functionally use the degraded joint [1]. Articular cartilage is a tissue found on the surface of bones in joint spaces which allows for easy articulation of the joint and also acts as a shock absorber when forces are applied to the joint. The articular cartilage is mainly composed of type II collagen and aggrecan proteins while chondrocyte cells are interspersed through the tissue with a volume of 1% to 3% which help to maintain the cartilage [2]. To date, there has been no treatment method to mitigate the progression of OA. The use of injectable lubricating agents like hyaluronic acid and pain relievers are the current methods of palliative treatment [3]. After complete loss of the articular cartilage or loss of functional use of the joint, more invasive measures need to be taken such as partial or total knee replacement surgery.

One possible treatment method is the use of articular cartilage coverings (ACC). ACC have been researched over the last several years as a method to

mitigate OA progression [4-6]. A biocompatible covering over the top of the damaged cartilage could alleviate direct articulation over the surface of the cartilage allowing for prolonged structural integrity and longevity of usefulness of the joint. Much of the work on ACCs has involved the combination of ACCs in conjunction with microfracture and autologous chondrocyte injection techniques. Microfracturing is a method of perforating the subchondral bone beneath the articular cartilage. Perforating the bone allows for infiltration of bone marrow into the articular cartilage which delivers blood, cytokines, growth factors, mesenchymal stem cells, and other progenitor cells that have shown to induce tissue repair [7]. The short fall of microfracture is its long-term efficacy. Tissue formed by microfracture is not as stable as the native articular cartilage tissue. In one such study by Kreuz et al, clinical evaluation of microfractued tissue at 18 months had marked improved scoring relative to pre-operation but at 36 months the clinical scoring had a significant decrease relative to the 18 month scoring [8]. Work by Erggelet et al studied the covering of microfractured cartilage with a poly-glycolic acid (PGA) in an 6-month sheep study. They were able to demonstrate that by covering the microfractured region with PGA, a more native-like articular cartilage was regenerated relative to microfracture alone which showed more signs of fibrotic cartilage development [4].

ACC typically have a mesh-like quality and can be developed using several methods such as electrospinning. Electrospinning is a quick and effective method of producing a thin scaffold composed of nanofibers. Briefly, electrospinning is a technique to produce polymeric nanofibers by applying a

large voltage to a polymer solution. This voltage positively charges the polymer solution which draws the solution to a negatively charged collecting plate. Once the electrostatic forces have been overcome, the polymer solution will stretch from the source in the form of nanofibers and will collect onto the collection plate. As the nanofibers are drawn to the collection plate, the solvent used to dissolve the polymer evaporates leaving a nanowoven polymer scaffold.

Polycaprolactone (PCL) is an FDA approved polymer and is commonly used in tissue engineering applications due to its biocompatibility and biodegradability *in vivo* [9-11]. PCL has been used in a wide range of applications like vascular reconstruction, bone regeneration, and craniofacial defects [10-12]. It is a commonly electrospun polymer. In one study by Townsend et al, they developed a PCL/polylactide-co-caprolactone scaffold encapsulated with ceragenin-131 or arginylglycyl aspartic acid which was electrospun onto 3D printed PCL rings intended for tracheal defect patches [13].

A drawback of using PCL in biologic applications is the polymers' inherent hydrophobicity. An alternative material that could be utilized is soy lecithin. Soy lecithin is a classic amphiphilic molecule with initial isolation dating back to 1845 [14]. It is commonly used as a food emulsifier but has also been used in biomedical applications. For example, lecithin may have applications in enhanced wound healing [15]. It has also been used as a stabilizing agent for antitumor drugs [16]. The inherent hydrophobicity of PCL can be reduced by integrating lecithin into PCL electrospinning solutions. Zhang et al showed

through contact angle analysis that by incorporating lecithin into PCL electrospun fibers, the scaffold became fully wetted creating a hydrophilic surface [17].

Previous work in our lab was performed with a lecithin/PCL scaffold by Matson et al [18]. Reproducibility of electrospun lecithin/PCL scaffolds has been a common issue particularly in the summer months due to high humidity levels. This chapter focuses on isolating issues leading to the reproducibility of electrospun lecithin/PCL scaffolds through SEM analysis.

4.2 Materials and methods

4.2.1 Scaffold Preparation

To prepare the lecithin/PCL scaffold, 1.2 g of PCL was mixed with 0.8 g lecithin. The PCL & lecithin was subsequently dissolved in 5 ml of a $CHCl_3$/DMF (7:3, volume ratio). The mixture was then covered using parafilm and placed on a stir plate at 50°C and 200 rpm for 1 hour to allow the PCL to dissolve and become homogenous. After the solution was homogenous, it was filled into a 10 ml syringe. The syringe was placed on a syringe pump and either polypropylene (PP) or polytetrafluoroethylene (PTFE) tubing was attached to the syringe and an 18-gauge cannula was attached on the opposing end. The cannula was placed in the cannula holder which was positively charged in the electrospinning chamber. Flow rate of the solution is specified on the images shown in the figures.

4.2.2 Electrospinning Chamber Preparation

The electrospinning setup was enclosed in a plexiglass chamber in a horizontal configuration. Compressed air was supplied into the chamber to reduce the ambient humidity of the chamber to less than 4%. The working distance between the cannula tip and the collection plate was 18 cm. The voltage ranged from 15 kV to 18 kV and is specified on the images shown in the figures.

4.2.3 SEM Characterization

An FEI Quanta 600 FEG environmental scanning electron microscope (SEM) (Hillsboro, OR) was used to image the electrospun scaffolds and observe the surface morphology. ImageJ was used to quantify the fiber diameter of each scaffold.

4.3 Results

4.3.1 Tubing Characterization

Upon visual inspection of the tubing used to pump the lecithin/PCL solution from the syringe to the end of the cannula, a non-uniform inner diameter

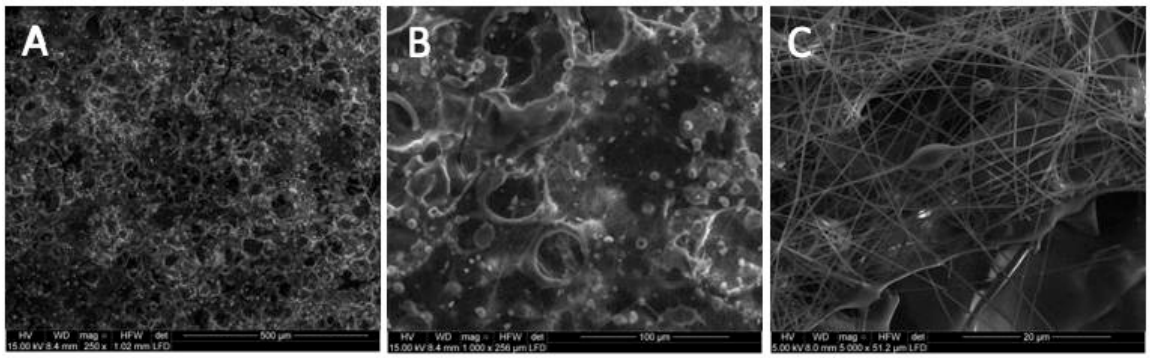

Figure 4.1. SEM Micrographs of lecithin/PCL electrospun scaffold at 1 ml/hr at 18 kV with polypropylene tubing. (A) 250x; (B) 1,000x; (C) 5,000x

was apparent. It appeared that the solvent used to dissolve the PCL was also dissolving the PP tubing. Figure 4.1 are SEM images of the electrospun lecithin/PCL scaffold using the PP tubing. The scaffold has some developed fibers, but a majority of the scaffold is a matted material with non-evaporated solvent unusable for in vivo applications. Figure 4.2 are SEM images of the lecithin/PCL scaffold using the PTFE tubing. Visually these images are much different than Figure 4.1. Both scaffolds in Figure 4.1 and Figure 4.2 were flowed at 1 ml/hr and 18 kV. The scaffold created using PTFE tubing is composed completely of nanofibers with no remnants of other non-evaporated materials.

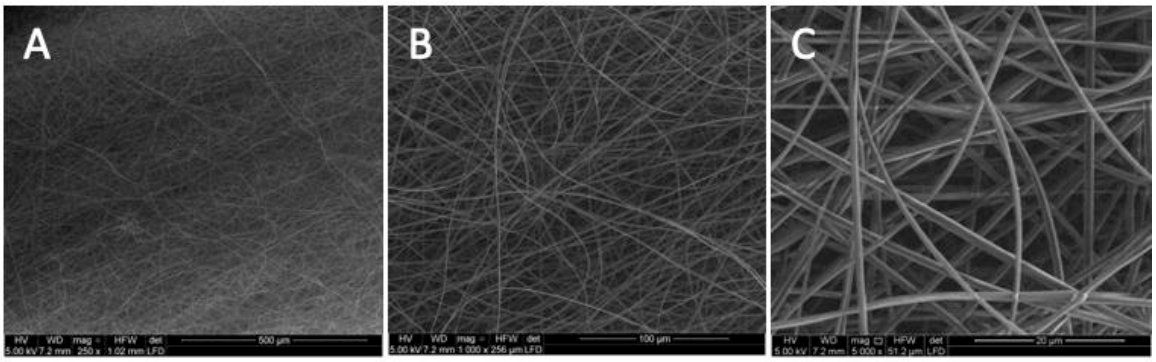

Figure 4.2. SEM Micrographs of lecithin/PCL electrospun scaffold at 1 ml/hr at 18 kV with polytetrafluoroethylene tubing. (A) 250x; (B) 1,000x; (C) 5,000x

4.3.2 Humidity Characterization

Humidity can play a large factor in fiber formation during the electrospinning process. With the summer months in Missouri, humidity can reach over 85% daily. Humidity in the electrospinning chamber is regularly over 20%. To determine if humidity was another factor in creating nanofibers, compressed air with ~0% humidity was flowed into the chamber. Electrospinning was started once the ambient humidity in the chamber was reduced to less than 4%. Figure 4.3 is an image of the lecithin/PCL scaffold at 3 ml/hr and 17 kV with

no humidity control. Figure 4.4 is the scaffold at the same flow rate and kV with less than 4% humidity. Figure 4.3 does not have a uniform nanowoven structure;

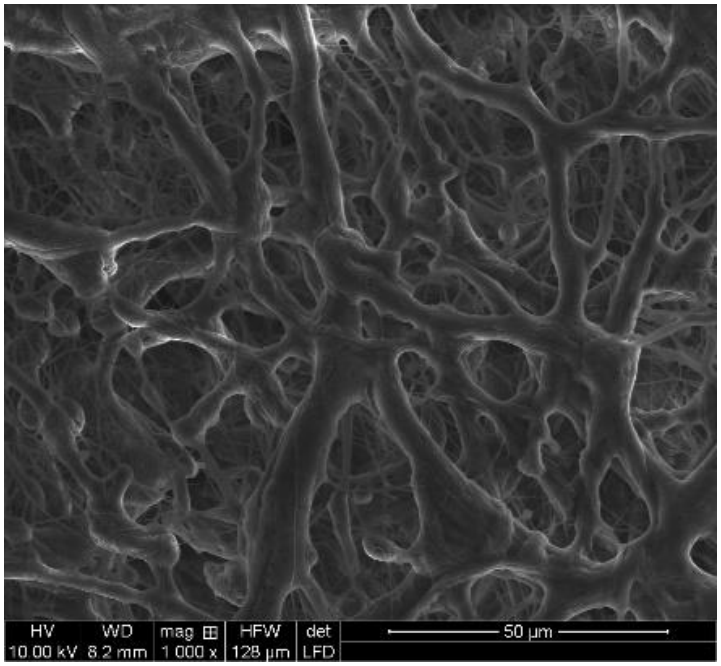

Figure 4.3. An SEM micrograph of a lecithin/PCL scaffold at 3ml/hr at 17 kV with no humidity control.

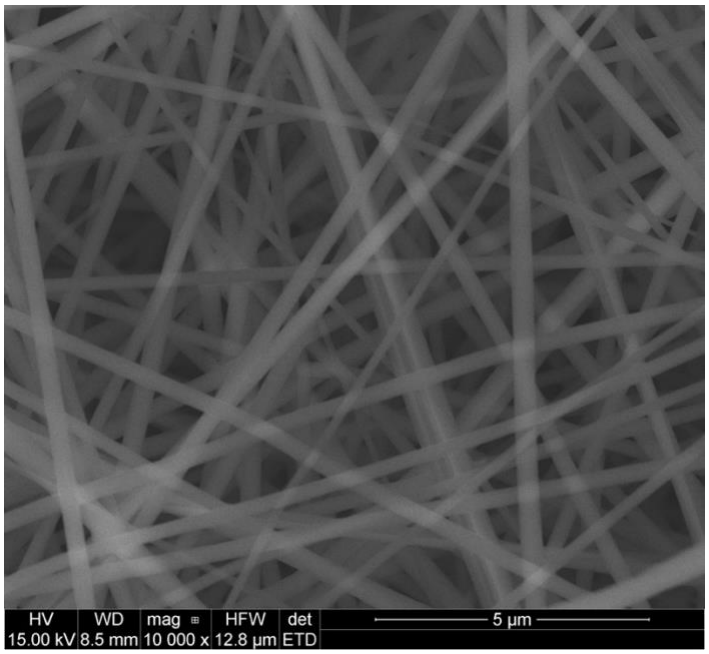

Figure 4.4. An SEM micrograph of a lecithin/PCL scaffold at 3 ml/hr at 17 kV with humidity less than 4%.

its average diameter is 429±107 nm while Figure 4.4 displays uniform nanofibers throughout with an average diameter of 275±81.1 nm.

4.3.3 Flow Rate and Voltage Characterization

Effects of flow rate and voltage were determined on the development of fiber diameters using the PTFE tubing and a low humidity (>4% humidity) chamber. Table 4.1 displays the results. By maintaining the flow rate at 3 ml/hr and increasing the voltage from 15 kV to 18 kV in 1 kV increments, the average fiber diameter was reduced and as well as the standard deviation. Increasing the voltage from 15 kV to 18 kV reduced the fiber diameter by 20% and created more uniform fibers. Reducing the flow rate to 1ml/hr actually increased the average fiber diameter and increasing the flow rate to 6 ml/hr held the average fiber diameter around the same value relative to the 3 ml/hr flow rate. A more uniform fiber diameter was observed by reducing the flow rate from 3 ml/hr to 1 ml/hr.

All samples observed in the SEM images shown in Figure 4.4 were able to successfully form fibers. Nucleation sites where some solvent was left unevaporated can be seen in Figures 4.5B, 5D, 5E & 5F. The sample with the most prominent nucleation sites was 15 kV with a flow rate of 3 ml/hr.

Table 4.1. Average fiber diameter and SD of electrospun lecithin/PCL at various flow rates and applied voltages

	Average Diameter (nm)	Standard Deviation (±)
3ml/hr 15kV	300.96	131.15
3ml/hr 16kV	274.64	111.28
3ml/hr 17kV	275.32	81.10
3ml/hr 18kV	251.72	57.03
1ml/hr 18kV	345.76	41.96
6ml/hr 18kV	263.40	46.45

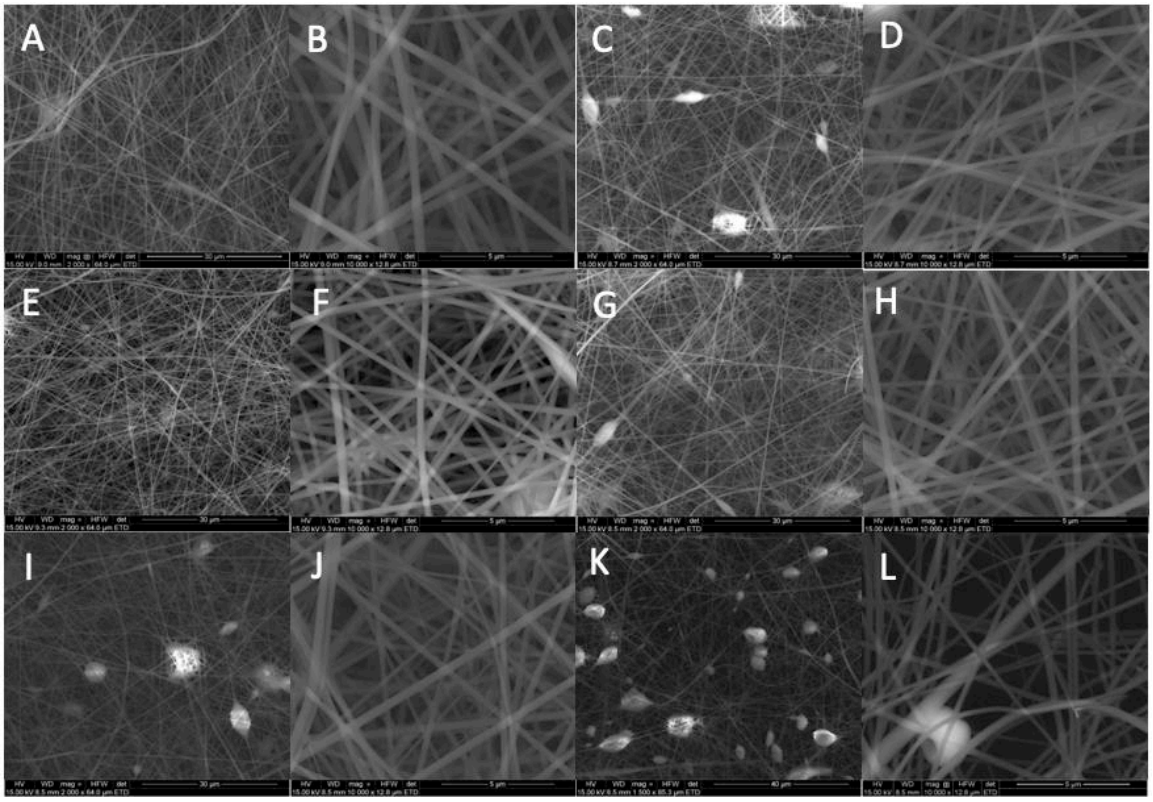

Figure 4.5. SEM micrographs of lecithin/PCL scaffolds with (A, B) 1 ml/hr at 18 kV; (C, D) 3 ml/hr at 18 kV; (E, F) 6 ml/hr at 18 kV; (G, H) 3 ml/hr at 17 kV; (I, J) 3 ml/hr at 16 kV; (K, L) 3 ml/hr at 15 kV.

4.4 Discussion

The work in this chapter focused on examining the parameters that could influence the characteristics of an electrospun lecithin/PCL scaffold suitable for osteoarthric tissue coverings. Previous work by lab member Matson et al describes in detail the in vitro work with the electrospun lecithin/PCL scaffolds [18].

To examine the fabrication of this scaffold, electrospinning under 1) a low humidity environment and 2) two different tubes flowing the lecithin/PCL solution were performed. Initial work was performed with PP tubing which flowed the lecithin/PCL solution from the syringe to the end of the cannula. It was evident

upon visual inspection of the tubing that the solvents used to prepare the lecithin/PCL solution were dissolving the tube and thus affecting the results of electrospinning as shown in Figure 4.1. Using PTFE tubing resolved the dissolution of the tubing and provided electrospun fibers without visible imperfections as shown in Figure 4.2.

Next, humidity of the chamber was examined to determine its effect on creating uniform fibers. Electrospun fibers without any humidity control can be observed in Figure 4.3. Figure 4.4 is an image of the same lecithin/PCL electrospun scaffold with humidity less than 4%. Uniform fibers were created by reducing the humidity in the chamber. Fibers that were made without humidity control were non-uniform and had a non-traditional morphology relative to common electrospun PCL fibers. Fibers made under humidity control had a more traditional morphology with uniform fiber diameters common to other electrospun fibers. Humidity control creates a more reproducible and controllable lecithin/PCL scaffold. It is theorized that the presence of the humidity hinders the evaporation rate inside the chambers. It is critical that evaporation of the solvents occur during the “time of flight” of the fibers so that dry fibers are deposited on the plate. If evaporation fails to occur, then fiber formation is hindered, resulting in a non-porous structure.

Finally, various flow rates and applied voltages were studied to determine how they affect fiber diameters. As shown in Table 4.1, applying an increased voltage, from 15 kV to 18 kV while holding flow rate constant, decreased average fiber diameter. This decrease in fiber diameter is due to the increase force

potential between the positive electrode and the ground plate, drawing out the fiber and reducing the overall diameter. Not only was a decreased in fiber diameter observed but also more uniform fiber diameters were correlated with an increase in voltage, which could be due to the strength of the potential maintaining better uniformity. While increasing the flow rate and holding the applied voltage constant did not return as expected results, reducing the flow rate increased the average fiber diameter. However, the fibers were more uniform relative to scaffolds produced with a flow rate of 3 ml/hr. Also, increasing the flow rate to 6 ml/hr returned a similar average fiber diameter relative to the 3 ml/hr sample. The 6 ml/hr had a more uniform fiber diameter compared to the 3 ml/hr sample. It is apparent that the flow rates do not affect the fiber diameter as much as the voltage, but it may affect the uniformity. It is theorized that the evaporation rate may be playing a role in uniformity; however, more research needs to be performed to determine the influencing factors on uniformity.

4.5 Conclusion

Based on the results from Figure 4.4 and factoring in other the previous studies, using PTFE tubing and reducing the humidity of the electrospinning chamber to less than 4% are necessary to create uniform electrospun fibers. Using 18 kV creates a scaffold with low nucleation site of unevaporated solvents and a flow rate of 1 ml/hr created the most uniform fiber diameter of all samples tested.

4.6 References

1. Glyn-Jones, S., et al., *Osteoarthritis.* The Lancet, 2015. **386**(9991): p. 376-387.

2. Luo, Y., et al., *The minor collagens in articular cartilage.* Protein & cell, 2017. **8**(8): p. 560-572.

3. Mora, J.C., R. Przkora, and Y. Cruz-Almeida, *Knee osteoarthritis: pathophysiology and current treatment modalities.* Journal of pain research, 2018. **11**: p. 2189.

4. Erggelet, C., et al., *Formation of cartilage repair tissue in articular cartilage defects pretreated with microfracture and covered with cell-free polymer-based implants.* Journal of Orthopaedic Research, 2009. **27**(10): p. 1353-1360.

5. Siclari, A., et al., *A cell-free scaffold-based cartilage repair provides improved function hyaline-like repair at one year.* Clinical Orthopaedics and Related Research®, 2012. **470**(3): p. 910-919.

6. Gillogly, S.D. and R.M. Arnold, *Autologous chondrocyte implantation and anteromedialization for isolated patellar articular cartilage lesions: 5-to 11-year follow-up.* The American journal of sports medicine, 2014. **42**(4): p. 912-920.

7. Steadman, J.R., W.G. Rodkey, and J.J. Rodrigo, *Microfracture: surgical technique and rehabilitation to treat chondral defects.* Clinical Orthopaedics and Related Research®, 2001. **391**: p. S362-S369.

8. Kreuz, P., et al., *Results after microfracture of full-thickness chondral defects in different compartments in the knee.* Osteoarthritis and cartilage, 2006. **14**(11): p. 1119-1125.

9. Lam, C.X., et al., *Evaluation of polycaprolactone scaffold degradation for 6 months in vitro and in vivo.* Journal of Biomedical Materials Research Part A: An Official Journal of The Society for Biomaterials, The Japanese Society for Biomaterials, and The Australian Society for Biomaterials and the Korean Society for Biomaterials, 2009. **90**(3): p. 906-919.

10. Tillman, B.W., et al., *The in vivo stability of electrospun polycaprolactone-collagen scaffolds in vascular reconstruction.* Biomaterials, 2009. **30**(4): p. 583-588.

11. Mitsak, A.G., et al., *Effect of polycaprolactone scaffold permeability on bone regeneration in vivo.* Tissue Engineering Part A, 2011. **17**(13-14): p. 1831-1839.

12. Rohner, D., et al., *In vivo efficacy of bone-marrow-coated polycaprolactone scaffolds for the reconstruction of orbital defects in the pig.* Journal of Biomedical Materials Research Part B: Applied Biomaterials: An Official Journal of The Society for Biomaterials, The Japanese Society for Biomaterials, and The Australian Society for Biomaterials and the Korean Society for Biomaterials, 2003. **66**(2): p. 574-580.

13. Townsend, J.M., et al., *Biodegradable electrospun patch containing cell adhesion or antimicrobial compounds for trachea repair in vivo.* Biomedical Materials, 2020. **15**(2): p. 025003.

14. Hensing, J.T., *The discovery of lecithin, the first phospholipid.* Bull. Hist. Chem, 2004. **29**(1): p. 9.

15. Nasab, M.E., et al., *In vitro antioxidant activity and in vivo wound-healing effect of lecithin liposomes: a comparative study.* Journal of comparative effectiveness research, 2019. **8**(8): p. 633-643.

16. Li, H., et al., *Soybean lecithin stabilizes disulfiram nanosuspensions with a high drug-loading content: remarkably improved antitumor efficacy.* Journal of Nanobiotechnology, 2020. **18**(1): p. 1-11.

17. Zhang, M., et al., *Small-diameter tissue engineered vascular graft made of electrospun PCL/lecithin blend.* Journal of Materials Science: Materials in Medicine, 2012. **23**(11): p. 2639-2648.

18. Matson, T., et al., *Electrospun PCL, gold nanoparticles, and soy lecithin composite material for tissue engineering applications.* Journal of biomaterials applications, 2019. **33**(7): p. 979-988.

Chapter Five

PRELIMINARY INVESTIVATION ON FABRICATION OF COLLAGEN MICROPARTICLES

5.1 Introduction

Fabrication of microparticles as scaffolds for tissue engineering applications are one of many different scaffold fabrication techniques ranging from electrospinning to 3D printing. Microparticles are widely fabricated due to their ease of drug delivery and potential targeting of specific locations in the body. They serve as excellent drug delivery candidates because of their high surface area to volume ratio. A review by Gupta et al. reports five different classifications for microparticle applications [1]. The five classifications include 1) controlled release of bioactive agents; 2) delivery of bioactive agents in response to environmental stimuli; 3) act as miniature bioreactors embedded in surrounding tissue for regeneration; 4) serve as cell transporters; 5) manipulation of porosity for accelerated resorption; 5) provide mechanical support for a weak matrix [1].

A few different techniques have been employed to fabricate microparticles. A couple common techniques for fabrication include water-in-oil (W/O) emulsion, and precision particle fabrication (PPF). W/O emulsion is a technique wherein a liquid “water” phase material of interest is introduced to an oil phase solution, typically on a stir plate, and emulsified at a high rpm or under sonication to generate liquid phase microparticles. The speed of rotation,

frequency of sonication, and addition of surfactants to manipulate the interfacial tension in the emulsion can tune microparticle sizes. Generally, chemical crosslinking is employed to maintain the microparticles morphology under fabrication but temperature and pH adjustment can also be used to form stable microparticles. PPF is another technique used to fabricate microparticles. PPF is a technique wherein a bulk fluid is flowed through an inner sonicating nozzle which disperses the bulk fluid into uniform particles while being entrapped by an outer nozzle of flowing liquid which flows into a collection plate. Typically, in this setup adjusting the sonication frequency, flow rate of each fluid, and the distance between the end of the nozzle and the collection plate can affect the microparticle size distribution.

A wide range of material have been used for microparticle fabrication including natural materials like chitosan [2], collagen [3], and alginate [4] or degradable, synthetic polymers like polylactic acid [5], polylactic glycolic acid [5] and polycaprolactone [6]. Collagen is the most common protein found in the body with collagen type I being the most prevalent collagen. It serves as an excellent candidate as a biomodulatory and cellular transporter and has been utilized to transport cells to affected regions in the body. For example, it has been utilized in bone tissue engineering applications [7]. Collagen is also advantageous due to its biodegradability, minimal immune response, and its exceptional biocompatibility [8]. In this chapter various methods were investigated to fabricate collagen microparticles (CMPs).

5.2 Materials and methods

5.2.1 Collagen Preparation

Porcine collagen type I (10 mg/ml, Sunmax Biotechnology,Taiwan) was precipitated using 1.04 M sodium chloride (NaCl, ≥99.0%, Sigma Aldrich, MO). The precipitated collagen solution was then centrifuged at 3,500 rpm for 15 minutes. A white collagen pellet was formed at the bottom of the tube and the supernatant was poured off leaving a 150 mg collagen pellet. Fifteen ml of 0.5 M glacial acetic acid (≥99.7%, Fisher Chemical, KS) was added to the collagen pellet and allowed to sit overnight at room temperature to let the collagen pellet dissolve. The collagen/acetic acid solution was then placed in a 15 ml, 10 kDa molecular weight cutoff dialysis cassette (Thermo Scientific, IL) and immersed in an ethylenediaminetetraacetic acid (35mM, EDTA, Fisher Chemical, KS)/ H_2O solution with a pH of 7.5 using sodium hydroxide (10 N, NaOH, Ricca Chemical Co., TX) [9]. The pH of the EDTA solution was checked and maintained at 7.5 daily until the pH no longer fluctuated from 7.5. The collagen solution was then removed and pH was tested to ensure it was set at 7.5.

5.2.2 Collagen Microparticle Sonicator Fabrication

A Branson Sonifier 450, 102C probe sonicator was used to create CMPs. To prepare the CMPs, the sonicator was set to continuous at level 5. To collect the CMPs, a petri dish was filled with 40 ml of 37°C ddH_2O. The distance between the tip of the probe to the petri dish was 14.5 cm. To create the CMPs a syringe was filled with liquid collagen and a 27 gauge needle was used to eject

the liquid collagen onto the tip of the probe. Samples were then centrifuged at 4,000 rpm and stored at 4°C in 70% ethanol.

5.2.3 Water-in-water fabrication

To create CMPs through water-in-water emulsion a 50 ml Erlenmeyer flask was used with a 6 cm stir bar. The Erlenmeyer flask was filled with 30 mm ddH_2O or cellularly relevant culture media and stirred at a rate of 1,250 rpm. Liquid collagen was then ejected into the Erlenmeyer flask using a syringe with a 27 gauge cannula. Five minutes after the addition of the liquid collagen, the stir plate heating element was set to 37°C. The emulsion was then stirred for 30 minutes. Samples were then washed at 4,000 rpm and stored at 4°C in 70% ethanol.

5.2.4 Imaging Analysis

To visualize the preparation techniques of sonication and water-in water emulsion an IX50 (Olympus, PA) microscope with a 4x objective was utilized. A linear polarized light filter was also used to observe the birefringence of the CMPs. Images were captured using Olympus CellSens software.

5.2.5 Cell Biocompatibility

Cell biocompatibility testing was performed to observe the cellular viability of L-929 fibroblast cells (ATCC, VA) with CMPs. L-929 murine fibroblast cells were cultured at 37˚C and 5% CO_2 in Eagle's Minimum Essential Medium

(ATCC, VA) supplemented with horse serum (10%, ATCC, VA) and penicillin-streptomycin (200 U/mL, ATCC, VA). Cells were subcultured and given fresh cell media as needed. All assays were performed in a biological safety cabinet under sterile conditions.

Cell proliferation reagent WST-1 (Sigma Aldrich, MO) was utilized to assess the biocompatibility of the CMPs. All CMPs were incubated with cell media for 24 hours and then added to a 96-well plate. 24 hours later, $0.75x10^4$ L-929 murine fibroblasts/well were added to a 96 well plate. Half of the medium in each well was replaced after 3 days. At 4 days, WST-1 reagent was added to each well and the plates were incubated at 37 °C for 4 hours. After 4 hours, the media was removed from each well and absorbance readings were taken at 450 nm, with 600 nm filter, using a spectrofluorometer plate reader (Cytation 5, BioTek, VT). Relative viability was based on cells with no scaffold added.

5.3 Results

5.3.1 Sonicator CMPs Fabrication

Figure 5.1 shows the CMPs fabricated utilizing sonication. Figure 5.1A is a light microscope image of the CMPs. A non-uniform distribution of CMPs were generated using this method. From visual inspection, immediately after the liquid collagen dispersed from the sonicating probe the CMPs formed and fibrilized. Figure 5.1B is a linear polarized light microscope image of the same particles in Figure 5.1A. Figure 5.1B provides a clearer picture of the CMPs. With this

information, a strong birefringence can be observed which correlates to a fibrilized collagenous structure of the CMPs.

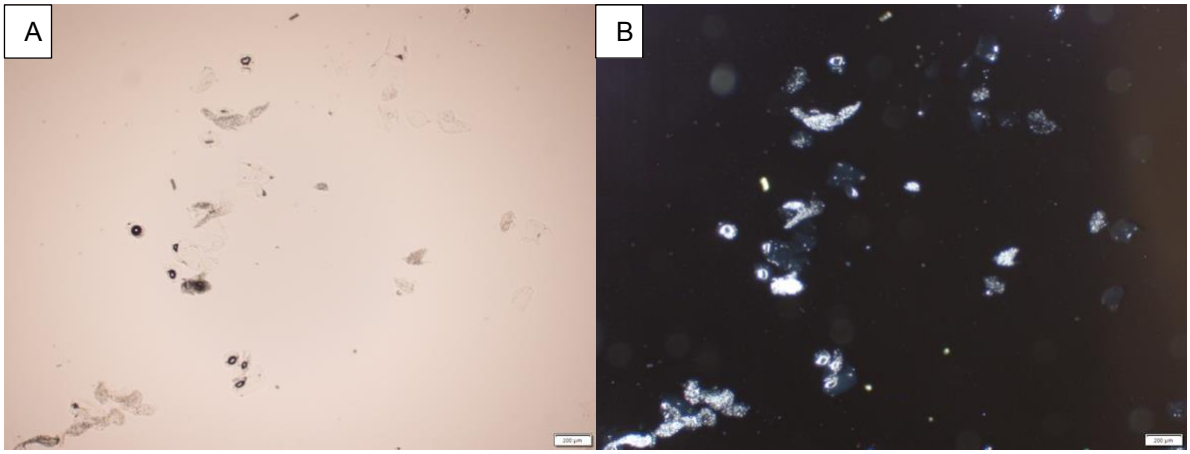

Figure 5.1. 4x microscope images of sonicated CMPs using (A) light microscopy; (B) linear polarized light microscopy.

5.3.2 Water-in-water Emulsion CMPs Fabrication

Figure 5.2 shows CMPs fabricated through water-in-water emulsion. Figure 5.2A is a light microscope image with Figure 5.2B being linear polarized light image of the same CMPs. The CMPs fabricated in this process appeared to form random structures. Again, Figure 5.2B aids visualization of fabricated collagenous CMPs through polarized light microscopy.

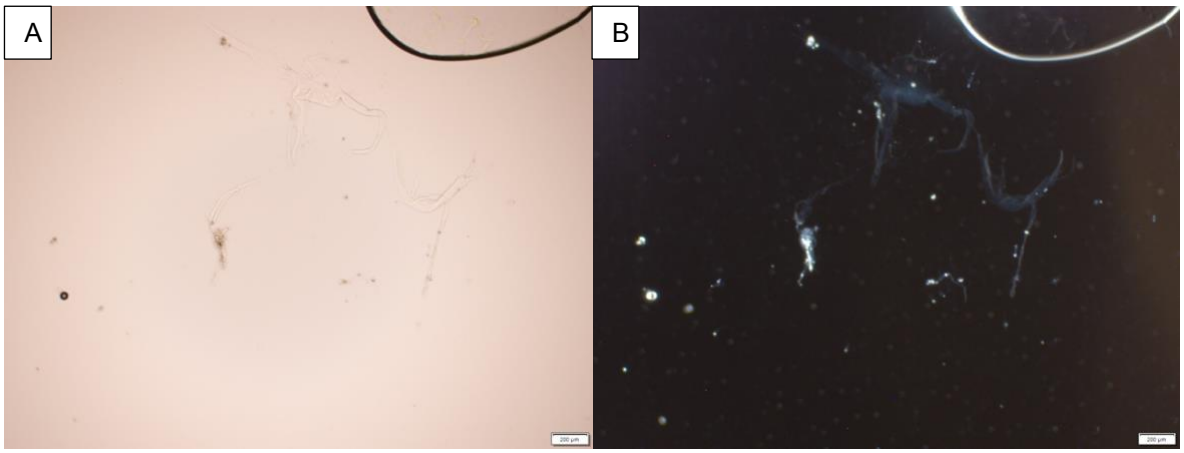

Figure 5.2. 4x microscope images of water-in-water CMPs using (A) light microscopy; (B) linear polarized light microscopy.

5.3.3 WST-1 Assay with Water-in-Water CMPs

A 4-day WST-1 assay was performed with CMPs emulsified in either H_2O or cell media and incubated with L929 fibroblast cells. At the terminal time point of 4 days, the group emulsified in cell media had a relative viability of 85% while the group emulsified in H_2O had a relative viability of 49% as shown in Figure 5.3. There was a significant difference observed between the two groups ($p \leq 0.0005$). Figure 5.4A & 4B are images of the cells incubated with the CMPs fabricated in H_2O and cell media respectively. CMPs fabricated in H_2O appeared to form a layer on the bottom of the well plate while the CMPs fabricated in cell media appeared to remain in defined particles attracting cells to the surface of the particles after 4 days.

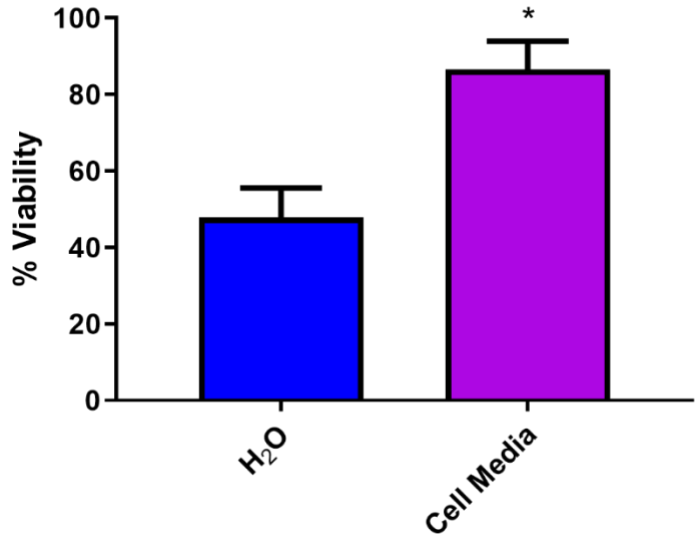

Figure 5.3. 4-day WST-1 assay using water-in-water emulsion with L929 fibroblast cells. N=5. *= p≤ 0.0005

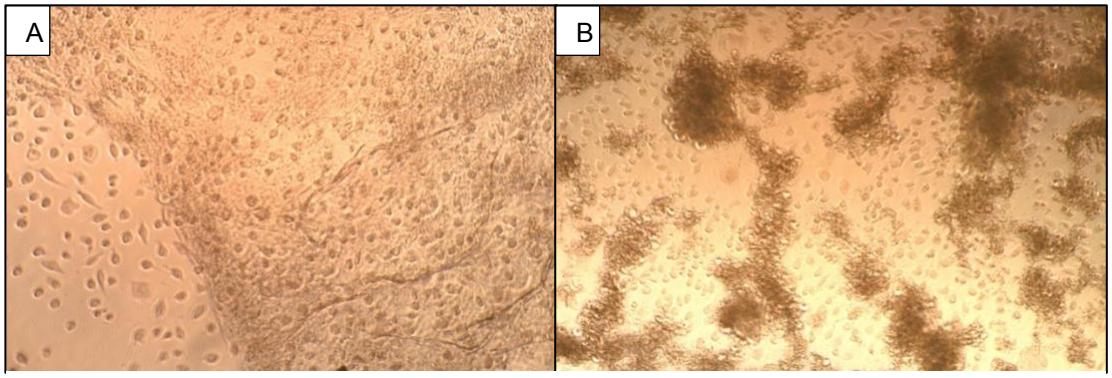

Figure 5.4. 10x light microscope images of 4-day culture of L929 fibroblast cells with (A) CMPs fabricated in H_2O; (B) CMPs fabricated in cell media.

5.4 Discussion

Two methods of CMP fabrication were investigated using microscopy. One method of fabrication that was investigated was probe sonication of liquid collagen to form CMPs while the other method was the utilization of water-in-water emulsion. Both methods formed fibrilized particles analyzed using linear polarized light microscopy in Figures 5.1 & 5.2. Both methods are quick

techniques to form CMPs with the sonication method generating CMPs immediately after sonication and water-in-water emulsion generating particles in 30 minutes.

A cell study was performed with both CMPs incubated in cell media prior to addition to the well plate. However, CMPs fabricated in cell media significantly demonstrated enhanced biocompatibility as compared to the CMPs fabricated in H_2O as shown Figure 5.3. There may be some benefits of the CMPs being fabricated in cell media as compared to the water. It is possible that during the fabrication process, CMPs are loading or entrapping the liquid (water or cell media). Even though the CMPs are subsequently incubated in cell media prior to addition to the well plate, the higher percentage of cell media entrapped during fabrication is more cell friendly than the entrapped water. Additionally, the CMPs fabricated in cell media appear to maintain their shapes as individual particles while the CMPs fabricated in H_2O appeared to be reduced or unravel and form a collagenous layer on the bottom of the well plate as shown in Figure 5.4A.

The cells appeared to be attracted to the surface of the CMPs fabricated in cell media as shown in Figure 5.4B. An explanation for this enhanced biocompatibility may be due to the CMPs being loaded with a high concentration of cell media which is providing a sustained release of fresh media which is attracting cells or cells may prefer the collagen substrate relative to the polymer well plate. A higher concentration of cells can also be observed on the surface of the collagen relative to the exposed well plate in Figure 5.4A.

In summary, two techniques of CMP fabrication - Collagen Microparticle Sonicator Fabrication and Water-in-water fabrication (both in water and cell culture media) were examined. Both techniques were quick and easy to use. A cell culture biocompatibility test with the water-in-water fabrication technique (both in water and cell culture media) demonstrated enhanced biocompatibility of CMPs in cell media.

5.5 References

1. Gupta, V., et al., *Microsphere-based scaffolds in regenerative engineering.* Annual review of biomedical engineering, 2017. **19**: p. 135-161.

2. Sinha, V., et al., *Chitosan microspheres as a potential carrier for drugs.* International journal of pharmaceutics, 2004. **274**(1-2): p. 1-33.

3. Hui, T.Y., et al., *In vitro chondrogenic differentiation of human mesenchymal stem cells in collagen microspheres: Influence of cell seeding density and collagen concentration.* Biomaterials, 2008. **29**(22): p. 3201-3212.

4. Joshi, A., et al., *Multifunctional alginate microspheres for biosensing, drug delivery and magnetic resonance imaging.* Acta Biomaterialia, 2011. **7**(11): p. 3955-3963.

5. Anderson, J.M. and M.S. Shive, *Biodegradation and biocompatibility of PLA and PLGA microspheres.* Advanced drug delivery reviews, 2012. **64**: p. 72-82.

6. Luciani, A., et al., *PCL microspheres based functional scaffolds by bottom-up approach with predefined microstructural properties and release profiles.* Biomaterials, 2008. **29**(36): p. 4800-4807.

7. Chan, B.P., et al., *Mesenchymal stem cell–encapsulated collagen microspheres for bone tissue engineering.* Tissue Engineering Part C: Methods, 2010. **16**(2): p. 225-235.

8. Herford, A.S., et al., *Use of a porcine collagen matrix as an alternative to autogenous tissue for grafting oral soft tissue defects.* Journal of Oral and Maxillofacial Surgery, 2010. **68**(7): p. 1463-1470.

9. Devore, D., et al., *Development and characterization of a rapid polymerizing collagen for soft tissue augmentation.* Journal of Biomedical Materials Research Part A, 2016. **104**(3): p. 758-767.

Chapter Six

A NOVEL CROSSLINKER-FREE TECHNIQUE TOWARD THE FABRICATION OF COLLAGEN MICROSPHERES

6.1 Abstract

Injectable collagen microspheres (CMs) have the potential to be an excellent tool to deliver various modulatory agents or to be used as a cellular transporter. A drawback has been the difficulty in producing reliable and spherical CMs. A crosslinker-free method to fabricate CMs was developed using liquid collagen (LC) in a water-in-oil emulsion process with varying concentrations of surfactant span-80. Different emulsion times of up to 16-hours were utilized to produce the CMs. Visual microscopy and scanning electron microscopy were utilized to determine the morphology of the CMs. To determine the fibril nature of the CMs, focus ion beam milling, energy dispersive spectroscopy, and Fourier Transformation-Infrared spectroscopy were performed. A cell biocompatibility study was performed to assess the biocompatibility of the CMs. The results demonstrated that consistent spherical CMs were achievable by changing the span-80 concentration. The CMs were fibrilized not only at the surface but also at the core. Both the 1-hour and the 16-hour emulsion time demonstrated biocompatibility and it appeared that the cells preferentially adhered to the CMs. This crosslinker-free method to fabricate CMs resulted in spherical, stable, biocompatible CMs, and could be an excellent technique for multiple tissue engineering applications.

6.2 Introduction

Recent advances in the field of musculoskeletal deficiencies, histogenesis, and chondro/osteoinduction are mainly attributed to the utilization of naturally occurring collagen as fillers [1]. Collagen is the most abundantly found protein in the human body, with collagen type I, II, and III composing 80-90% of all collagen [2]. The triple helix of type I collagen is composed of three peptide chains that have α1 and α2 subunits, having a characteristic repeating X-Y-Glycine sequence, with X and Y most commonly being proline and hydroxyproline respectivly [3]. A single triple helix conforms with two α1 subunits and one α2 subunit contributing to its design as an integral structural component and thus allowing collagen to be an excellent candidate for biomaterial applications [4].

Collagen is also commonly used in biomedical applications due to its excellent biocompatibility and is biodegradable with no harsh byproducts [5]. Collagen can be processed in many forms and shapes using various processes including casting, molding [6], electrospinning [7], and 3D printing [8]. While these processes can result in many different shapes and forms of the collagen structure, for tissue engineering applications, it is highly desirable for the collagen materials to be injectable as it allows minimal invasive surgeries, faster healing times, and less inflammation. Among all shapes, spheres of collagen, as microspheres, have attracted special attention due to their injectable characteristics [9].

Collagen microspheres (CMs) have been utilized in injectable form for tissue applications for recapitulation of cartilage [10], bone [11], blood vessel [9],

and intervertebral disc development [12]. In addition, the microspheres have also been used as a drug transporter for proteins such as bovine serum albumin [13], histone [13], bone morphogenetic protein 2 [11], vascular endothelial growth factor [9], and transforming growth factor beta-3 [14]. Furthermore, CMs have not only been utilized to entrap and carry various proteins but have also been used to entrap and carry cells like chondrocytes and mesenchymal stem cells [10, 15]. For example, an interesting study by Li et al [10] describes the entrapment of undifferentiated and chondrogenic pre-differentiated mesenchymal stem cells (MSC) within CMs into an osteochondral defect rabbit model. The authors demonstrated that regardless of whether the MSCs were undifferentiated or differentiated, the higher cell density resulted in better histological scores. Further, the study showed that undifferentiated and pre-differentiated MSCs at high cell densities produced hyaline cartilage. Even though there have been many biomedical applications for CMs, the fabrication of CMs is cumbersome and labor-intensive; current fabrication procedures require crosslinkers during emulsification which can lead to cytotoxicity or pipetting cycles that are time-consuming and produce non-injectable microspheres [10, 12].

The current CMs fabrication procedures commonly utilized micropipetting of collagen or emulsion. For example, neutralized type I rat tail collagen was micropipetted onto a parafilm lined Petri dish; the collagen gelled into a spherical form under physiological temperatures and conditions [10, 12]. This technique suffers disadvantages as it requires individual pipetting cycles to obtain CMs, which is time-consuming and laborious. More importantly, the technique yields

microspheres of different sizes ranging from 300 μm to 1000 μm. Other researchers have worked on different fabrications to overcome this disadvantage; Nagai et. al. utilized a water-in-oil emulsion process to fabricate CMs [9]. Commonly, a collagen solution is added to an oil emulsion and allowed to stir for a set amount of time. Preceding work have used various oils such as corn oil, PDMS, paraffin oil, olive oil, paraffin/olive oil, and perfluorinated oil with surfactants such as tween-20, span-20, span-80, and have also used a range of emulsion rates ranging from 300 – 1,200 rpm that have all contributed to changing the average CM diameters [9, 11, 13-16]. By varying these parameters, prior publications have fabricated CMs of various sizes from several microns to 300 μm. One vital factor to consider is the use of crosslinking agents in forming CMs. These agents are used during the emulsification process to form stable CMs. Chemical crosslinking agents used to fabricate CMs with good stability include glutaraldehyde [17, 18] and EDC/NHS (1-Ethyl-3-[3-dimethylaminopropyl]carbodiimide hydrochloride)/N-hydroxysuccinimide [9, 16, 19]. A disadvantage of the use of traditional chemical crosslinker glutaraldehyde is that they have long been shown to have cytotoxic effects [20, 21]. In addition, the use of chemical crosslinkers can also effect cellular adhesion to type I collagen. Bax et al. describes the use of EDC/NHS crosslinking on type I collagen inhibiting native-like cellular adhesion [22]. They have proposed that the use of EDC/NHS crosslinking modifies the carboxylic acid groups on collagen altering divalent cation-dependet cell adhesion to cation-independent cell adhesion.

We have investigated CMs using a prefibrilized, liquid collagen (LC) solution to avoid the use of traditional crosslinking agents to maintain CM stability. LC was initially developed as a crosslinker-free soft tissue filler which fibrilizes in situ [23]. Previous studies have suggested that LC remains in a prefibrilized state due to the inclusion of ethylenediaminetetraacetic acid (EDTA) which surrounds the collagen fibrils preventing the formation of a triple helix leading to fibrillization [23]. Another possible explanation proposed is multiple ionic interactions occurring upon different regions along the individual collagen fibrils preventing fibrillization. Fibrillization of the collagen occurs when it is introduced into physiological tissue fluids resulting in the displacement of either the EDTA or the ions allowing for the formation of individual fibrils into its triple helix structure. Heat can also trigger the fibrillization of LC due to the collagen fibrils energetically preferring to fibrilize. The transition from liquid to a fibrilized network is visually evident as the LC transition from a clear liquid to a semi-solid opaque material maintaining the structural form. The advantages of utilizing LC include no toxic effects shown *in vivo*, and its inherent resistance to collagenase digestion, native tissue in-growth *in vivo*, and vascularization in vivo [23].

LC is an excellent material to use in the fabrication of CMs with a water-in-oil emulsion due to its ease of fibrillization under heated temperatures, relieving the need for a crosslinker. Here we describe a novel method to fabricate crosslinker-free CMs using span-80 and olive oil emulsion. Span-80, a surfactant, was utilized to manipulate the CM diameter, and fibrillization of the CMs was achieved by emulsification at 35°C due to the energetically favorable reaction

within the solution. The results demonstrated that reproducible CMs were achieved and the size ranges can be manipulated by utilizing different concentrations of surfactant. The CMs demonstrated biocompatibility and stability over time. It is expected that these CMs will be able to serve as an injectable carrier of biomodulatory agents like stem cells, proteins, and drugs.

6.3 Materials and methods

6.3.1 Fabrication of liquid collagen

Porcine collagen type I (10 mg/ml, Sunmax Biotechnology,Taiwan) was precipitated using 1.04 M sodium chloride (NaCl, ≥99.0%, Sigma Aldrich, MO). The precipitated collagen solution was then centrifuged at 3,500 rpm for 15 minutes. A white collagen pellet was formed at the bottom of the tube and the supernatant was poured off leaving a 150 mg collagen pellet. Fifteen ml of 0.5 M glacial acetic acid (≥99.7%, Fisher Chemical, KS) was added to the collagen pellet and allowed to sit overnight at room temperature to let the collagen pellet dissolve. The collagen/acetic acid solution was then placed in a 15 ml, 10 kDa molecular weight cutoff dialysis cassette (Thermo Scientific, IL) and immersed in an ethylenediaminetetraacetic acid (35mM, EDTA, Fisher Chemical, KS)/ H_2O solution with a pH of 7.5 using sodium hydroxide (10 N, NaOH, Ricca Chemical Co., TX) [23]. The pH of the EDTA solution was checked and maintained at 7.5 daily until the pH no longer fluctuated from 7.5. The collagen solution was then removed and pH was tested to ensure it was set at 7.5.

6.3.2 Fabrication of Collagen Microspheres

Fifty ml of olive oil (Sigma Aldrich, MO) and correlating volume of span-80 or span-60 (Sigma Aldrich, MO) was added to a 100 ml round bottom flask. A 4 cm stir bar was added to the flask and placed on a stir/hot plate and set to 1150 rpm. The emulsion was allowed to equilibrate for 10 minutes. After 10 minutes, 1 ml of the LC solution was added dropwise using an 18-gauge plastic cannula. One hour after the LC addition, the stir plate temperature was set to 35°C and allowed to stir for up to 16-hours. Preliminary studies show fibril formation occuring 1 minute after LC was added to 37°C olive oil, data not shown. After the emulsion time was reached the collagen/oil solution was poured into a 50 ml centrifuge tube and centrifuged at 5000 rpm for 5 minutes. The oil was then removed and 25 ml 50% acetone (Fisher Chemical, KS) and 100 μl tween-20 (Sigma Aldrich, MO) was added to the tube to wash the CMs. The solution was vortexed for 1 minute and sonicated for 3 minutes. The solution was then centrifuged at 5,000 rpm for 5 minutes. The sample was washed 3 times using 50% acetone and tween-20 and then was washed 3 times using 1x PBS (Sigma Aldrich, MO). The CMs were stored in 15 ml 1x PBS and placed in a 4°C refrigerator. They have been shown to remain stable for at least 10 months.

6.3.3 AuNP Conjugation to CMs

EDC/NHS crosslinking was utilized to conjugate 20 nm gold nanoparticles (AuNPs, $7.0x10^{11}$ particles/ml, Ted Pella, CA) to CMs. ~$5x10^3$ CMs were introduced to a 15 ml 30 mM EDC and 55 mM NHS solution for 5 minutes. 1 ml

AuNPs were functionalized using 15 uM cysteamine. After CMs incubated for 5 minutes in crosslinking solution, the functionalized AuNPs were added to the CMs and left on a shaker table for 24 hours at 225 rpm. CMs were washed three times using PBS.

6.3.4 CM Diameter Characterization

To determine the effects of the emulsion time and surfactant concentration on CM diameter, an inverted light microscope (IX50, Olympus, PA) with a 4x objective was utilized to examine the CMs. A 1:1 ratio of CMs to Trypan blue (0.4%, Sigma Aldrich, MO) dye was added to help visualize CMs under the microscope. Images were captured using SPOT software and CM diameters were measured using ImageJ. At least 100 CM diameters were collected per group and analyzed.

6.3.5 Electron Microscopy Characterization

CM morphology was studied using a scanning electron microscope (SEM) (Scios DualBeam, Thermo Scientific, MA), 5kV - 15kV was used to image the sample. Samples were placed in a fixative solution of 100 nM sodium cacodylate, 2% glutaraldehyde, and 2% paraformaldehyde (provided by the University of Missouri Electron Microscopy Core) for 30 minutes and washed three times with H_2O. Samples were then placed on carbon tape, and the liquid was allowed to evaporate for 1-hour at 40°C prior to imaging for hydrated imaging. Critical point drying (CPD) was also used to image CMs. For CPD, samples were negative

stained with osmium and coated with platinum once fixed on carbon tape. Focused ion beam (FIB) milling was utilized to create a cross-section to determine the fibril structure of the core of the CMs. A gallium ion beam was used during FIB milling. Additionally, energy-dispersive X-ray spectroscopy (EDS) was conducted on the CMs to identify the elemental composition of the CMs.

6.3.6 FTIR

Fourier-transform infrared spectroscopy (FTIR) was performed to verify the collagen fibril formation in the CMs. An ATR-FTIR (Nicolet 6700, Thermo Scientific, MA) was utilized. Ten replicates from each sample were analyzed by averaging 32 scans per sample at a resolution of 4 cm^{-1} at room temperature. Samples were prepared by storage in a -20°C refrigerator for 24 hours and lyophilizing using a Labconco FreeZone-1 for 24 hours.

6.3.7 Thermal Stability Analysis

Differential scanning calorimetry was conducted to deterime the thermal stability of CMs. A Q2000 DSC (TA Instruments, DE) was used to determine the denaturation temperature from a non-reversing heat flow plot. Approximately 2 – 5 mg of lyophilized CMs were loaded into hermetic lid aluminum pans. Samples were tested from 5°C to 105°C with a ramp rate of 3°C per minute. Universal Analysis software was used to determine the denaturation temperature.

6.3.8 Cell Biocompatibility

Cell biocompatibility testing was performed to verify the cellular viability of L-929 fibroblast cells (ATCC, VA) with CMs. L-929 murine fibroblast cells were cultured at 37˚C and 5% CO_2 in Eagle's Minimum Essential Medium (ATCC, VA) supplemented with horse serum (10%, ATCC, VA) and penicillin-streptomycin (200 U/mL, ATCC, VA). Cells were subcultured and given fresh cell media as needed. All assays were performed in a biological safety cabinet under sterile conditions.

Cell proliferation reagent WST-1 (Sigma Aldrich, MO) was utilized to assess the biocompatibility of the CMs. In this assay, tetrazolium salts were added to wells containing cells and CMs. The CMs were incubated in cell media for 24 hours at 37°C before being added to a 96 well plate. $0.75x10^4$ L-929 murine fibroblasts/well were added to a 96 well plate and 24 hours later CMs were added to the cell seeded well plate. Half of the medium in each well was replaced after 72 hours. At the terminal time point, WST-1 reagent was added to each well and the plates were incubated at 37°C for 4 hours. After 4 hours, the media was removed from each well and absorbance readings were taken at 450 nm, with 600 nm filter, using a spectrofluorometer plate reader (Cytation 5, BioTek, VT). L-929 fibroblasts with no CM scaffold served as the 100% viability baseline.

6.4 Results

6.4.1 Influence of Surfactant Concentration on Microsphere Diameter

To understand the influence of span-80 and span-60 on the size of CMs, we performed the fabrication in various concentrations of span-80 and span-60. Specifically, we varied the concentrations from 0 to 0.50% (v/v) for span-80 and from 0 to 2.50% (w/v) for span-60. The mean, standard deviation, median, and size range of each concentration is also shown in Table 6.1 for span-80 and Table 6.2 for span-60. The average diameter and standard deviation of the CMs decreased with the increase in concentrations of span-80 from 92.7±44.1 μm with 0% span-80 to 22.7±12.9 μm with 0.35% span-80. Likewise with span-60, the average diameter from using 2.50% span-60 reduced by 81 μm relative to not

Table 6.1. Mean, standard deviation, median, and size range of counted CMs for each concentration of span-80 emulsion

Span-80 Concentration (v/v%)	Mean (μm)	Standard Deviation (±)	Median (μm)	Size Range (μm)
0	92.7	44.1	86.3	18.0 – 222.0
0.02	86.1	40.0	83.0	18.9 – 188.3
0.10	60.3	29.6	57.2	18.1 – 139.3
0.20	35.9	13.6	33.3	18.4 – 85.3
0.35	22.7	12.9	20.8	8.0 – 85.2

Table 6.2. Mean, standard deviation, median, and size range of counted CMs for each concentration of span-60 emulsion

Span-60 Concentration (w/v%)	Mean (μm)	Standard Deviation (±)	Median (μm)	Size Range (μm)
0	118	43	119.5	37 – 252
0.01	134	57	117	50 – 278
0.10	53	18	52	8 – 111
1.00	38	15	36	5 – 69
2.50	37	14	35	10 – 77

using span-60. Using a one-way analysis of variance (ANOVA) with a pairwise Tukey test ($p<0.05$), a difference in the average diameter of CMs was observed between 0.02%, 0.10%, 0.20% and 0.35% span-80 concentrations.

Figure 6.1A-F includes 4x light microscope images of CMs, which were dyed with trypan blue to increase visibility. The images demonstrate an increase in span-80 concentration to the reaction mixture up to 0.35%, lead to a decrease in particle size, as evidenced by the figures. However, the particle size did not significantly decrease after increasing the concentration of span-80 over 0.35% (v/v). Interestingly, upon increasing the concentrations of span-80 emulsion to 0.50% (v/v), the spherical morphology of the CMs was no longer maintained (Figure 6.1F). Based on the result, we determined that 0.35% (v/v) of span-80 in the formulation is considered to optimal concentration for generating uniform size CMs.

6.4.2 SEM and EDS Characterization

The spherical morphology of a hydrated, 1-hour CM emulsion is observed in Figure 6.2A of the SEM micrograph. Collagen fibrils were not immediately evident based on the surface morphology of the CM. FIB milling was utilized to mill half of the of the CM, as shown in Figure 6.2B-2H, to show the cross-section to reveal the morphology of the CM core. A progression from initial milling to fully milled CM (Figure 6.2B-2H) took a total time of 29 minutes with a 3nA current. After initial milling of the sphere, collagen fibrils were revealed. Further milling, as shown in Figure 6.2C-2F, continued to reveal the collagen fibrils throughout the

CM. A collagen network can be seen in Figure 6.2H cross-section along with white salt crystals.

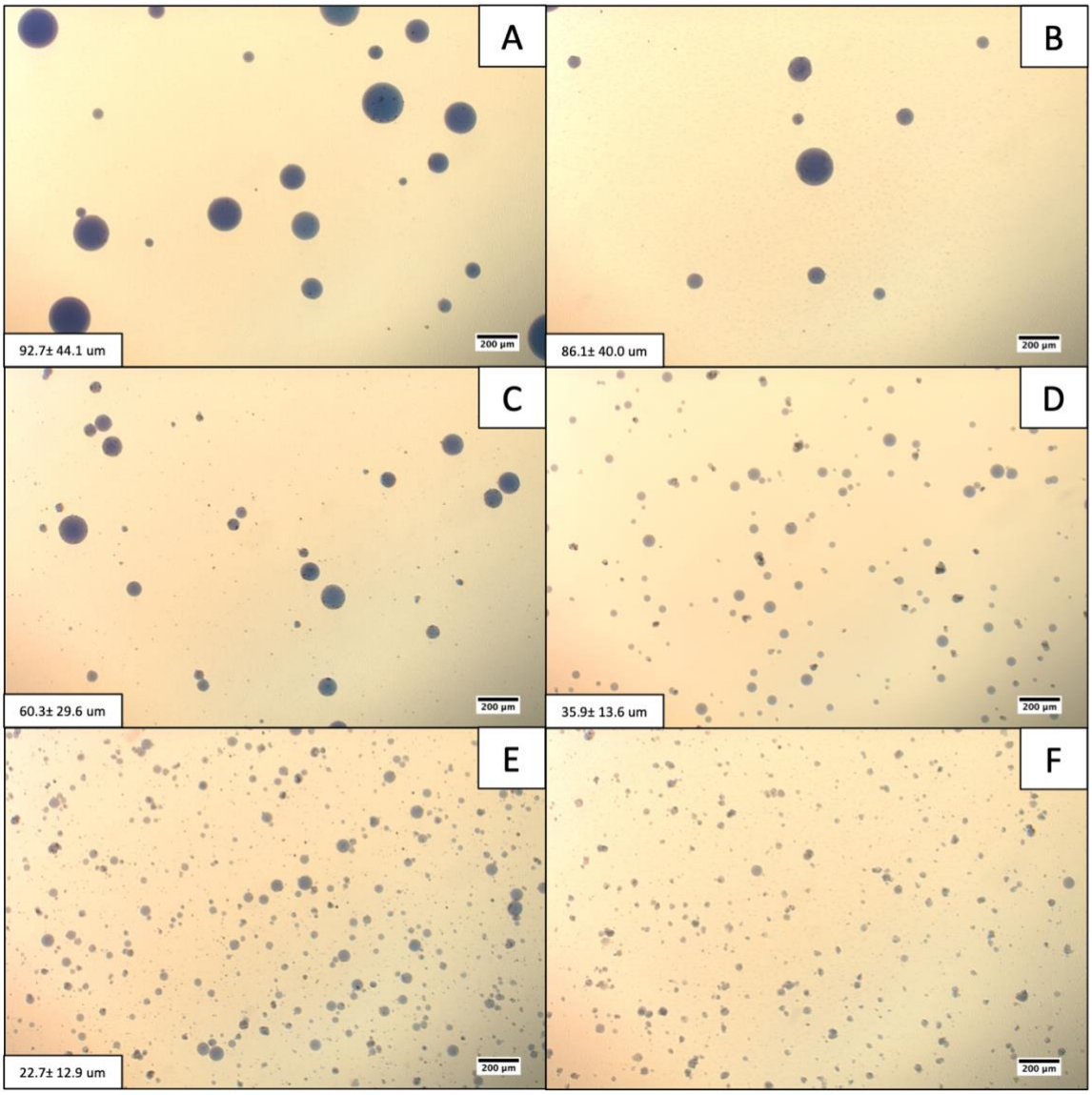

Figure 6.1. 4x light microscope images of 1-hour emulsion CMs with (A) 0% span-80; (B) 0.02% span-80; (C) 0.10% span-80; (D) 0.20% span-80; (E) 0.35% span-80; and (F) 0.50% span-80. Scale bar = 200 um

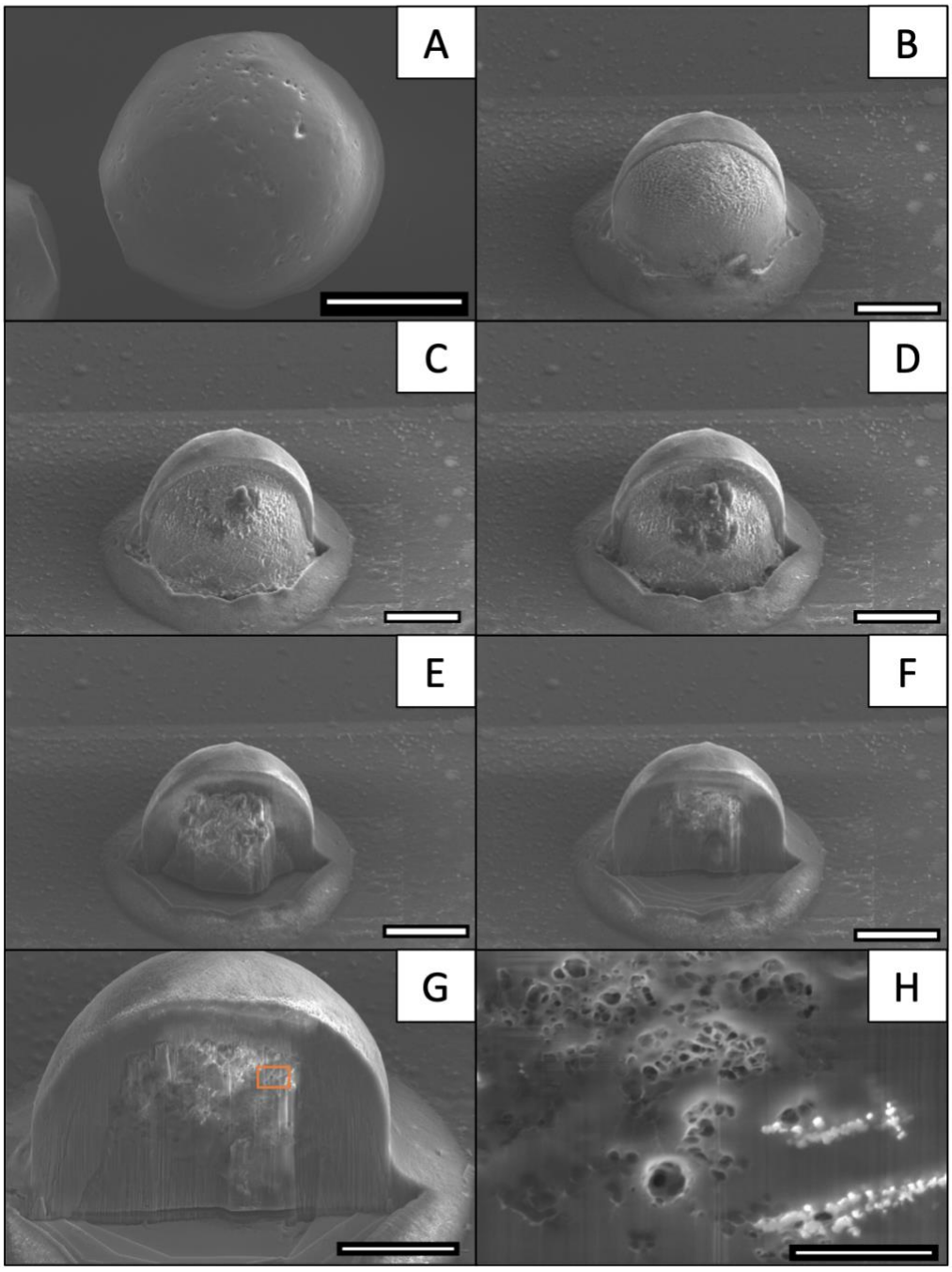

Figure 6.2. SEM micrograph of a CM emulsified for 1-hour and etched using gallium FIB milling. (A) is a CM prior to milling. Scale bar = 40 um. (B)-(F) are images taken during milling requiring 29 minutes with a 3 nA current. Scale bar = 30 um. (G) is a cross section of the core of the CM. Scale bar = 20 um. (H) is a high magnification image of the cross section from the orange box in (G). Scale bar = 5 um.

Figure 6.3A is an SEM micrograph of an 8-hour CM emulsion that has been fixed and critically point dried. Collagen fibrils appear to be evident on the surface of

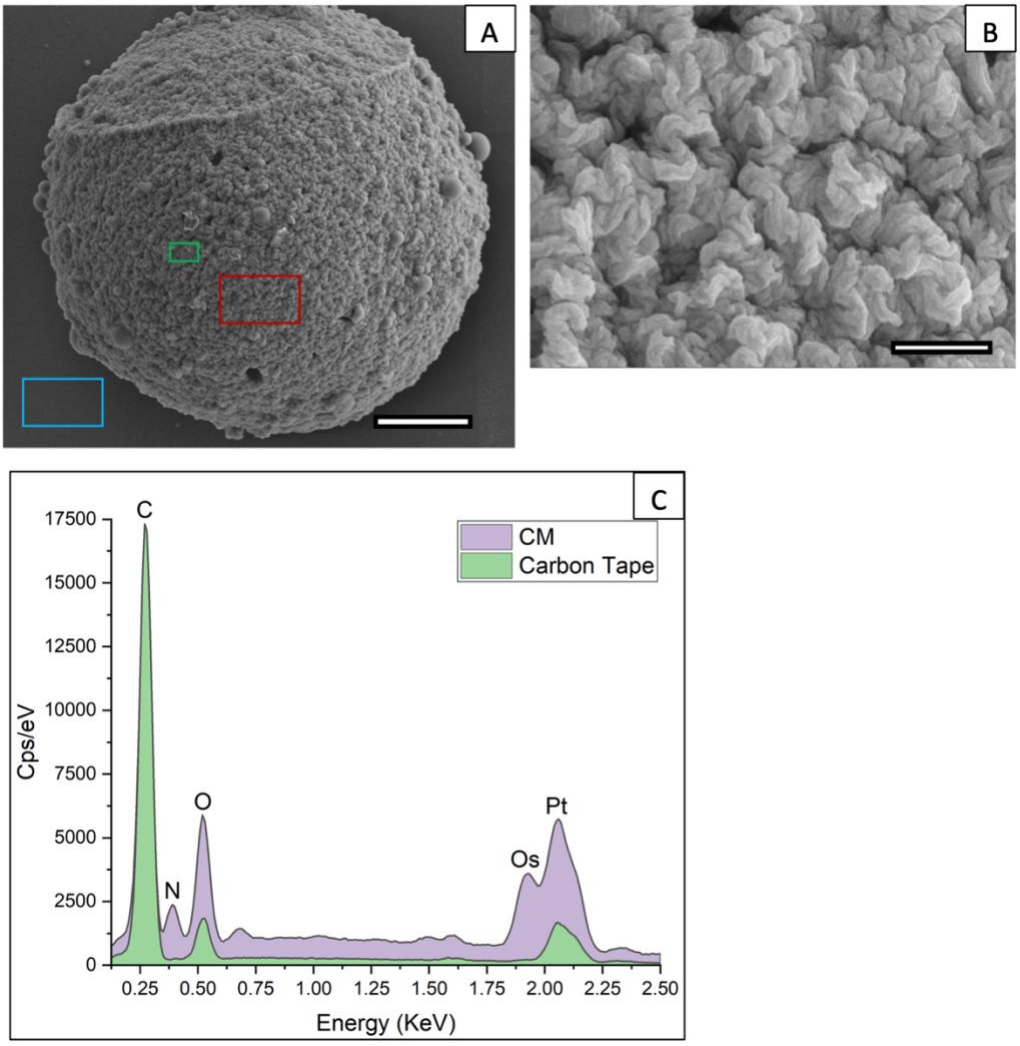

Figure 6.3. SEM micrograph of a CM emulsified for 8-hours (A) 9,000x magnification of CM. Scale bar = 5 um. (B) 80,000x magnification of CM within the region of the red square form image (A). Scale bar = 500 nm. (C) EDS spectra acquired from the CM (red box in (A)) and on carbon tape (blue box in (A)).

the CM in Figure 6.3A. Figure 6.3B is a magnified view of the CM within the highlighted green box in Figure 6.3A. Visually these fibrils appear to be a mature fibrilized network maintaining a spherical structure. Figure 6.3C is an EDS spectrum acquired on the surface of the CM (red box) and the carbon tape (blue box) as a background spectra. A strong nitrogen signal was acquired from the CM relative to the carbon tape background. A nitrogenous peak lends further

evidence of the composition of the CM is collagen due to collagen being the only material containing nitrogen during the fabrication process.

Figure 6.4 is another SEM micrograph of a critically point dried CM. This CM was conjugated with 20 nm AuNPs using EDC/NHS conjugation. Figure 6.4A is an SEM micrograph of the the overall structure of the CM. The fibril structure is evident. Figure 6.4B is a backscatter electron micrograph. The red box is the region imaged in Figure 6.4C. Figure 6.4C provides a closer image of the detailed fibril structure of the CM. The light spots on the backscattered electron image are AuNPs that were conjugated on the CM. The AuNPs appear to be fairly homogenous over the whole surface of the CM. This provides evidence that AuNPs can be conjugated to CMs through EDC/NHS conjugation.

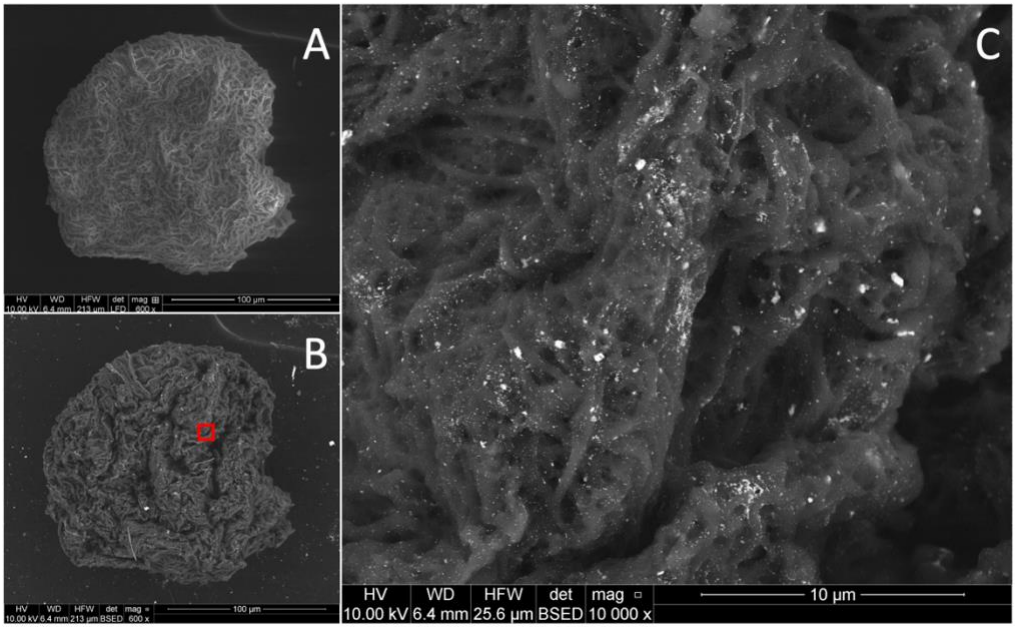

Figure 6.4. Scanning electron micrograph of a CM conjugated with AuNPs (A) SE image at 600x; (B) BSE image at 600x; (C) BSE image at 10,000x, red box indicates region imaged in C.

6.4.3 FTIR Analysis

FTIR spectra from 1,700-1,000 cm^{-1} were acquired from six separate samples to determine the fibrilized nature of the CMs. The first sample tested was LC, which was added to the olive oil emulsion to form the CMs. The second sample was of the fibrilized collagen. To prepare the fibrilized collagen, LC was immersed in water for 24 hours to form a fibrilized collagen structure. The results, as shown in Figure 6.5, demonstrated that the fibrilized collagen and the CM samples had similar characteristic peaks. Collagen characteristic peaks were found at amide I between 1700-1600 cm^{-1}, amide II between 1600-1500 cm^{-1}, and amide III between 1300-1180 cm^{-1} corresponding to (C=O) stretching, (C-N) stretching and (N-H) bending, and (C-N) stretching, (C-H) bending and (C-C) stretching [24].

While the CMs spectra mimic that of the fibrilized collagen's spectra with peaks found at the amide I, amide II, and amide III absorption bands, the LC had two peaks at 1585 cm^{-1} and 1400 cm^{-1} with a shoulder at 1630 cm^{-1}. After fibrillization of the collagen, the 1585 cm^{-1} and 1400 cm^{-1} peaks are reduced and thereby revealing amide I and amide II absorption bands in the fibrilized collagen and CM samples.

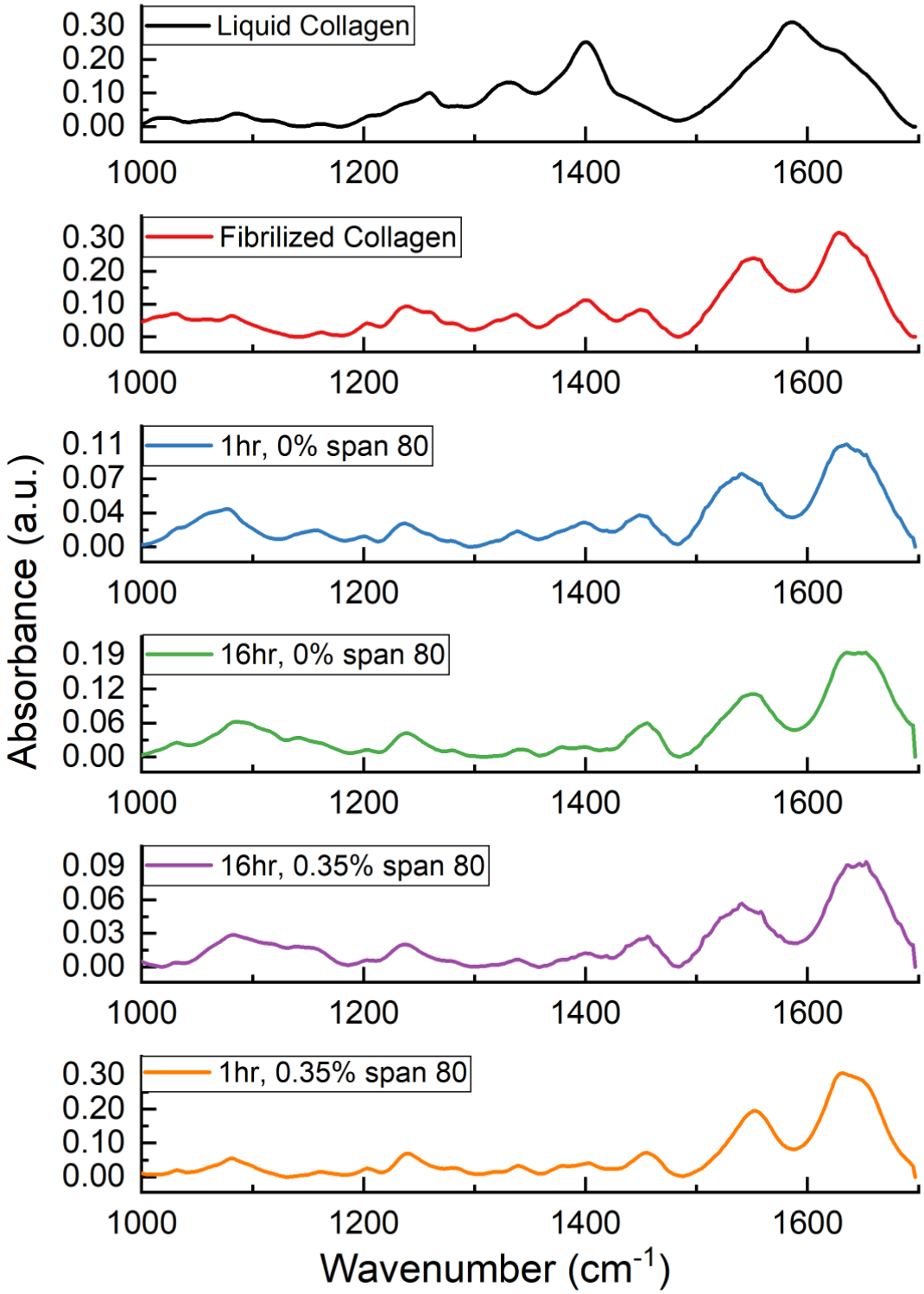

Figure 6.5. FTIR spectra of prefibrilized liquid collagen, fibrilized collagen, 1-hour emulsion CM with 0% span-80, 16-hour emulsion CM with 0% span-80, 16-hour emulsion CM with 0.35% span-80, and 1-hour emulsion CM with 0.35% span-80.

6.4.4 Thermal Stability Analysis

Differential scanning calorimetry was utilized to determine the thermal stability of fabricated CMs. One and 16 hour emulsion with and without 0.35% span-80 CMs were analyzed in this study which can be observed in Figure 6.6. CMs without the addition of span-80 were thermally more stable than samples emulsified with span-80. The 16 hour emlusion sample without span-80 was the most thermally stable sample with an average denaturization temperature of 60.1°C. Both the 1 hour and 16 hour emulsion with 0.35% span-80 had very similar denaturization temperature at 41.6°C and 41.0°C respectively. Both samples fabricated in the span-80 solution had significantly lower denaturization temperature than both sampled fabricated without span-80.

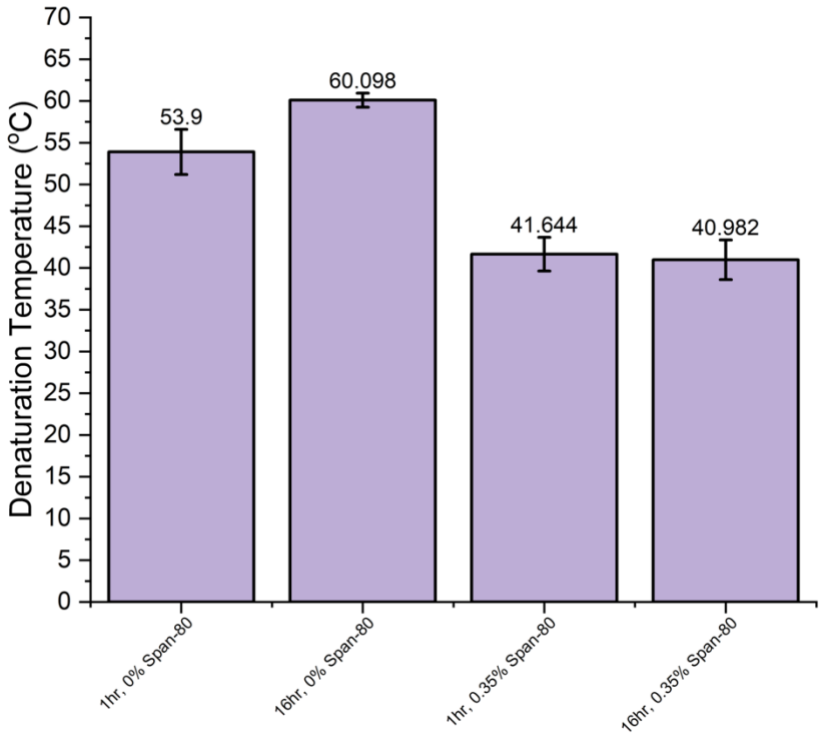

Figure 6.6. DSC results providing data on denaturization temperature of various preparations of CMs. N=5.

6.4.5 Cell Viability

To evaluate the cellular toxicity of CMs fabricated in our study, we performed a WST-1 cell viability assay. We used CMs emulsified for 1-hour and 16-hours using 0.35% span-80. This study also examined if the CM emulsion time affected fibroblast cell viability over 7 days. Even though the CMs form after 1-hour of emulsion time, it was desirable to determine if CMs would begin to denature at the longer emulsion times and thus become less biocompatible. We chose to compare the 1-hour emulsion time with an emulsion time of 16-hours. L-929 fibroblast cells were incubated with the CMs at 3, 5, and 7 day time points. Untreated L-929 fibroblast cells were used as control. The results demonstrated that there was no statistical significance between either group (1-hour or 16-hour emulsification time) relative to cells alone but inferences can be made upon the trend in cellular viability and visually how the cells interacted with the CMs during culture. After 3-days, as shown in Figure 6.7A, both the 1-hour and 16-hour CMs demonstrated equivalent cellular viability as compared to that of the control (set at 100% viability). Both Figure 6.7D & 7E show fibroblasts adhering to the surface of CMs. After 5 days, Figure 6.7B, both the 1-hour and 16-hour CMs showed overall increased viability in comparison to the control. Figure 6.7F & 7G showed significant coverage of fibroblast cells on the CMs with elongation of the fibroblasts extending from the CMs. At 7 days, Figure 6.5C, both 1-hour and 16-hour emulsions maintain a similar viability advantage in comparison to the control. Figure 6.7H & 7I show a high density of fibroblasts covering the bottom of the well plate and complete coverage on the surface of CMs.

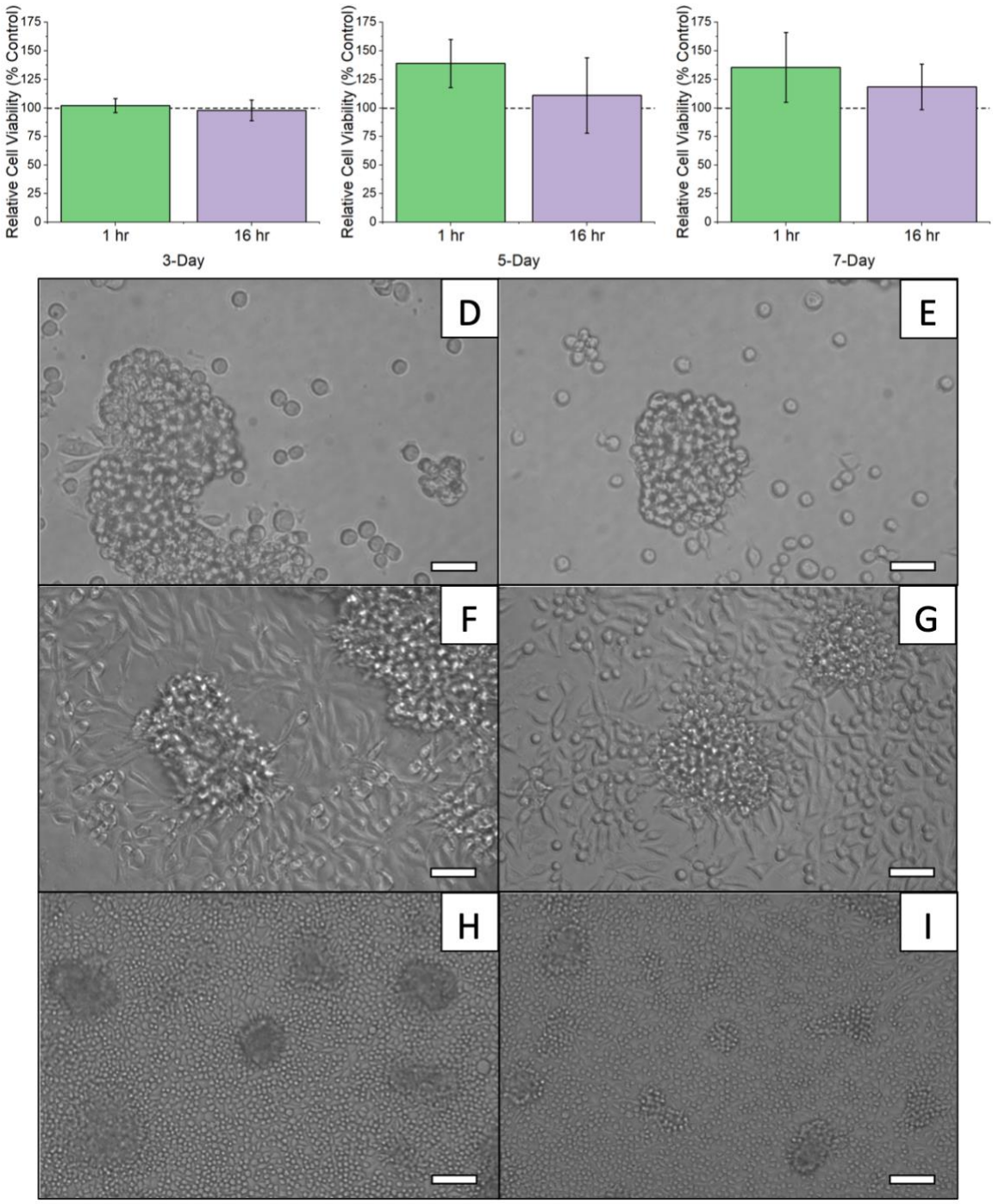

Figure 6.7. WST-1 cell viability assay with (A) 3-day, (B) 5-day, and (C) 7-day time points using L929 fibroblast cells. 20x light microscope images of (D) 3-day 1-hour emulsion and 0.35% span-80, (E) 3-day 16-hour emulsion and 0.35% span-80, (F) 5-day 1-hour emulsion and 0.35% span-80, (G) 5-day 16-hour emulsion and 0.35% span-80, (H) 7-day 1-hour emulsion and 0.35% span-80, (I) 7-day 16-hour emulsion and 0.35% span-80. Scale bar = 50 um.

6.5 Discussion

Type I collagen is a triple helix, polypeptide chain protein that can be easily processed in a variety of forms. Processing collagen as an injectable fibrilized material for tissue engineering applications is advantageous not only due to collagen's excellent biocompatibility but also due to its ability to integrate with tissue *in vivo*, forming a template for cellular attachment and resulting in no harmful byproducts. However, the injectability of bulk collagen is problematic mainly due to its high viscosity; therefore, researchers have processed collagen in different forms such as microspheres to ease injectability. CMs are versatile materials but the limitations in terms of fabrication, such as the need for crosslinkers during emulsification and the limited ability to inject CMs fabricated via individual pipetting cycles, creates an opportunity to utilize liquid collagen to fabricate CMs. To overcome the limitations, we developed a simple, crosslinker free method to fabricate CMs with reproducibility for a wide range of musculoskeletal applications using LC.

Controlling the size of CMs during the fabrication process to create uniform sizes is critical for tissue engineering applications particularly if the CMs are entrapped with additional biomodulatory agents or cells. The release of biomodulaory agents and the survivability of cells can be controlled with greater accuracy relative to size uniformity in correlation to the release kinetics of a sphere. A wide range of CM sizes can result in a bulk release or delayed release of agents and thus may not achieve the therapeutic effect or even may result in cytotoxicity. In this study, we were able to better control the average diameter

and standard deviation of the CMs by utilizing span-80. The use of span-80 resulted in a decreased CM diameter and standard deviation by decreasing the interfacial tension between water and oil seen in Table 6.1 [19]. Similarly the effect of span-60 on CM fabrication duing emulsion can be observed in Table 6.2. Span-80 was preferred and utilized in further studies due to its ability to fabricate smaller and more uniform particles relative to span-60. Span-60 is also in a solid form and takes more time to dissolve in solution where as span-80 is in a liquid form and can immediately be added to the emulsion. Figure 6.1 demonstrated the influence of increasing concentrations of span-80 during the CM fabrication process. The increased concentration of span-80 proportionally led to a decrease in CM average diameter and standard deviation; however, CM spherical morphology was lost after increasing the span-80 concentration over 0.35%.

Evidence to support a collagenous fibrilized network within the CM was two-fold. First, SEM imaging of 1-hour and 8-hour CM emulsions provided evidence of collagen fibrillization. The inspection of Figure 6.2A with the 1-hour emulsion time demonstrated a smooth surface. Uncovering the surface of the 1-hour emulsion CM using FIB milling, Figure 6.2B – 2F, provided evidence of a collagen network at the core of the CM.

Through critical point drying in Figure 6.3A and 3B of an 8-hour emulsion CM, a collagenous network was visually apparent. An additional study was performed to verify the composition of CMs using EDS. EDS identified the elemental composition of an 8-hour CM emulsion on the surface as shown in Figure 6.3C.

A nitrogenous peak was indicated on the surface of the CM. Nitrogen is a unique element to collagen during the CM fabrication process; thus further confirming the collagenous network created during fabrication.

Figure 6.4A provides further evidence of a fibril structure of CMs while also verifying conjugation of AuNPs to CMs. Figure 6.4B and 4C are both backscattered images of the CM. The light deposits found on the surface of the CM are AuNPs. The AuNPs are fairly distributed througout the surface of the CM. Previous work with AuNPs have shown them to be free radical scavengers along with promoting cell migration and attachment which may all be advantageous attributes for the CMs [25-29]. Validating conjugation of AuNPs to CMs can open new avenues to investigate AuNP-CMs in future work.

The second method utilized to identify fibrilized collagen within the CM was FTIR analysis as shown in Figure 6.5. The FTIR scans of the CMs were compared to that of the LC and fibrilized collagen. The CMs scans mimicked that of fibrilized collagen scans, which indicates the fibrilized nature of the CMs. Characteristic peaks of collagen reported in literature also correlated with the peaks identified in the CM scans [24, 30, 31]. Kim et al. provided an FTIR spectra of porcine collagen [32]. The spectra obtained correlated almost identically to the spectras of the fibrilized collagen and CM samples obtained in this work [33]. There were observable differences between the LC and the fibrilized collagen. For the LC, a single peak was identified at 1585 cm^{-1} while the fibrilized collagen and the CMs displayed two individual peaks at 1635 cm^{-1} and 1545 cm^{-1}, which corresponded to amide I and amide II respectively. Also, the LC sample had a

significant peak at 1400 cm^{-1} relative to all other samples. Liturature suggests that a peak at 1400 cm^{-1} is attributed to CH_2 bending from glycine residues and also symmetrical stretching of (COO-) from glutamate and aspartate [34-36] found in LC. Liu et al. proposed the diminishment in the intensity of 1400 cm^{-1} may be due to dehydration of type I collagen during the crosslinking or fibrillization stage [34, 37]. Fibrillization of collagen leads to dehydration [38]. It was observed that our CMs demonstrated a decrease in the 1400 cm^{-1} peak, which can be attributed to fibrillization; these results validate the fibrillization of the CMs.

Differential scanning calorimetry was used to determine the thermal stability of the CMs as shown in Figure 6.6. An emulsion of 1 or 16 hours with or without 0.35% span-80 was analized in this study. Both samples without span-80 had a significantly higher denaturization temperature with the 16 hour emulsion without span-80 had the highest average denaturization temperatrue of 60.1°C. Both samples with span-80 performed very similarly with denaturization tempearature for the 1 hour and 16 hour emulsion being 41.6°C and 41.0°C respectively. While the denaturization temperatures are lower for both samples with span-80 they are still above the average temperature of the body at 36.6°C allowing these samples to maintain their structre if implemented *in vivo* [39].

It was imperative that the CMs demonstrated biocompatibility. Cellular viability was performed to determine the compatibility of CMs with L-929 fibroblast cells. Three, five, and seven-day time points were evaluated and compared between the 1-hour and 16-hour CM emulsion times. At 3 days, both

the 1-hour and 16-hour CM emulsions were equivalent in cellular viability to the negative control (Figure 6.7A). At days 5 and 7, there was an overall trend toward enhanced viability compared to the negative control by both 1-hour and 16-hour CM emulsions (Figure 6.7D and Figure 6.7G). Upon visual inspection of the cells and the CMs over 7 days, it appeared that the cells have an attraction towards the CMs. As shown in Figure 6.7D-7I, cells were more clustered on the CMs than on the bottom of the 96-well plate. The CMs may play a role in enhancing cellular proliferation. While no quantitative data was recorded, the cells appeared to wrap around the surface of the CMs and gave the appearance of being adherent to the surface of the CMs. The cells also appeared to be extending from the CMs and creating a cellular network. These results were similarly observed by Matsuhashi et al. when incubating CMs with NIH3T3 cells [19].

Our findings demonstrated that fibroblast cells have an affinity for the crosslinker-free CMs. The cells may be experiencing a native-like recognition and cell attachment due to a larger number of integrin moities of the type I collagen along with a more open network as compared to collegen that has various chemical crosslinking agents [22, 40]. In future work, we propose the use of CMs as possible bioactive agent carriers and cell transporters. We examined the extensive work perfomed with adipose-derived mesenchymal stem cells (ADSC) on chondrocyte cells and on the differentiation into chondrocyte cells and our CMs are uniquly suited as an injectable transporter for ADSCs into osteoarthritc tissues due to their injectable size and their affinity for cellular

adherence [41-43]. We plan to examine the integration of CMs and ADSCs in a traditional impeller bioreactor and investigate the effects of CM-ADSCs on osteoarthritic chondrocyte cells or CM-differentiated ADSCs into chondrocyte cells on osteoarthric articular cartilage.

6.6 Conclusion

In this study, we developed a crosslinker-free method to fabricate CMs. CMs were developed using a LC in a water-in-oil emulsion process. We were able to modify the size of the CMs by using span-80. Fibrilized CM structures were obtained for up to 16-hour emulsion times. The spherical and fibrilized nature was confirmed via SEM. EDS analysis confirmed CMs composition through the identification of a unique nitrogenous peak to collagen. FTIR analysis also confirmed collagen transitioning from a pre-fibrilized state prior to the emulsion and subsequently to a fibrilized state after emulsion. The CMs exhibited a thermally stable, biocompatible material for both 1-hour and 16-hour emulsion times and it appeared that the cells preferentially adhered to the CMs. This crosslinker-free method to fabricate CMs resulted in spherical, stable, biocompatible CMs. Future applicatons could include injectable delivery agents for biomodulatory molecules or cellular transporter to achieve self-assembled scaffolds for tissue recapitulation.

6.7 References

1. Glowacki, J. and S. Mizuno, *Collagen scaffolds for tissue engineering.* Biopolymers, 2008. **89**(5): p. 338-344.

2. Uzman, A., *Molecular Cell Biology (4th edition) Harvey Lodish, Arnold Berk, S. Lawrence Zipursky, Paul Matsudaira, David Baltimore and James Darnell; Freeman & Co., New York, NY, 2000, 1084 pp., list price $102.25, ISBN 0-7167-3136-3.* Biochemistry and Molecular Biology Education, 2001. **29**(3): p. 126-128.

3. Shoulders, M.D. and R.T. Raines, *Collagen structure and stability.* Annual review of biochemistry, 2009. **78**: p. 929-958.

4. Bella, J., et al., *Crystal and molecular structure of a collagen-like peptide at 1.9 A resolution.* Science, 1994. **266**(5182): p. 75-81.

5. Parenteau-Bareil, R., R. Gauvin, and F. Berthod, *Collagen-based biomaterials for tissue engineering applications.* Materials, 2010. **3**(3): p. 1863-1887.

6. Savolainen, J., et al., *Collagen synthesis and proteolytic activities in rat skeletal muscles: effect of cast-immobilization in the lengthened and shortened positions.* Archives of physical medicine and rehabilitation, 1988. **69**(11): p. 964-969.

7. Chen, J.-P., G.-Y. Chang, and J.-K. Chen, *Electrospun collagen/chitosan nanofibrous membrane as wound dressing.* Colloids and Surfaces A: Physicochemical and Engineering Aspects, 2008. **313**: p. 183-188.

8. Mozdzen, L.C., et al., *Increasing the strength and bioactivity of collagen scaffolds using customizable arrays of 3D-printed polymer fibers.* Acta biomaterialia, 2016. **33**: p. 25-33.

9. Nagai, N., et al., *Preparation and characterization of collagen microspheres for sustained release of VEGF.* Journal of Materials Science: Materials in Medicine, 2010. **21**(6): p. 1891-1898.

10. Li, Y.Y., et al., *Mesenchymal stem cell-collagen microspheres for articular cartilage repair: Cell density and differentiation status.* Acta Biomaterialia, 2014. **10**(5): p. 1919-1929.

11. Mumcuoglu, D., et al., *Collagen I derived recombinant protein microspheres as novel delivery vehicles for bone morphogenetic protein-2.* Materials Science and Engineering: C, 2018. **84**: p. 271-280.

12. Yuan, M., K.W. Leong, and B.P. Chan, *Three-dimensional culture of rabbit nucleus pulposus cells in collagen microspheres.* The Spine Journal, 2011. **11**(10): p. 947-960.

13. Chan, O., K.-F. So, and B. Chan, *Fabrication of nano-fibrous collagen microspheres for protein delivery and effects of photochemical crosslinking on release kinetics.* Journal of Controlled Release, 2008. **129**(2): p. 135-143.

14. Mathieu, M., et al., *Induction of mesenchymal stem cell differentiation and cartilage formation by cross-linker-free collagen microspheres.* Eur Cell Mater, 2014. **28**: p. 82-96.

15. Liu, J., et al., *Chondrocytes behaviors within type I collagen microspheres and bulk hydrogels: an in vitro study.* RSC Advances, 2015. **5**(67): p. 54446-54453.

16. Yang, C. and J. Wang, *Preparation and characterization of collagen microspheres for sustained release of steroidal saponins.* Materials Research, 2014. **17**(6): p. 1644-1650.

17. Wu, T.-J., et al., *Studies on the microspheres comprised of reconstituted collagen and hydroxyapatite.* Biomaterials, 2004. **25**(4): p. 651-658.

18. Chowdhury, D.K. and A.K. Mitra, *Kinetics of in vitro release of a model nucleoside deoxyuridine from crosslinked insoluble collagen and collagen–gelatin microspheres.* International journal of pharmaceutics, 1999. **193**(1): p. 113-122.

19. Matsuhashi, A., et al., *Fabrication of fibrillized collagen microspheres with the microstructure resembling an extracellular matrix.* Soft Matter, 2015. **11**(14): p. 2844-2851.

20. Gough, J.E., C.A. Scotchford, and S. Downes, *Cytotoxicity of glutaraldehyde crosslinked collagen/poly (vinyl alcohol) films is by the mechanism of apoptosis.* Journal of Biomedical Materials Research: An Official Journal of The Society for Biomaterials, The Japanese Society for Biomaterials, and The Australian Society for Biomaterials and the Korean Society for Biomaterials, 2002. **61**(1): p. 121-130.

21. Sung, H.-W., et al., *In vitro evaluation of cytotoxicity of a naturally occurring cross-linking reagent for biological tissue fixation.* Journal of Biomaterials Science, Polymer Edition, 1999. **10**(1): p. 63-78.

22. Bax, D.V., et al., *Fundamental insight into the effect of carbodiimide crosslinking on cellular recognition of collagen-based scaffolds.* Acta Biomaterialia, 2017. **49**: p. 218-234.

23. Devore, D., et al., *Development and characterization of a rapid polymerizing collagen for soft tissue augmentation.* Journal of Biomedical Materials Research Part A, 2016. **104**(3): p. 758-767.

24. Belbachir, K., et al., *Collagen types analysis and differentiation by FTIR spectroscopy.* Analytical and Bioanalytical Chemistry, 2009. **395**(3): p. 829-837.

25. Smith, S.E., et al., *Homogenized porcine extracellular matrix derived injectable tissue construct with gold nanoparticles for musculoskeletal tissue engineering applications.* Journal of Biomaterials and Nanobiotechnology, 2017. **8**(02): p. 125.

26. Ionita, P., F. Spafiu, and C. Ghica, *Dual behavior of gold nanoparticles, as generators and scavengers for free radicals.* Journal of materials science, 2008. **43**(19): p. 6571-6574.

27. Cozad, M.J., S.L. Bachman, and S.A. Grant, *Assessment of decellularized porcine diaphragm conjugated with gold nanomaterials as a tissue scaffold for wound healing.* Journal of Biomedical Materials Research Part A, 2011. **99**(3): p. 426-434.

28. Grant, S., et al., *A comparative study of the remodeling and integration of a novel AuNP-tissue scaffold and commercial tissue scaffolds in a porcine model.* Journal of Biomedical Materials Research Part A, 2013. **101**(10): p. 2778-2787.

29. Christenson, E.M., et al., *Nanobiomaterial applications in orthopedics.* Journal of Orthopaedic Research, 2007. **25**(1): p. 11-22.

30. de Campos Vidal, B. and M.L.S. Mello, *Collagen type I amide I band infrared spectroscopy.* Micron, 2011. **42**(3): p. 283-289.

31. Payne, K. and A. Veis, *Fourier transform IR spectroscopy of collagen and gelatin solutions: deconvolution of the amide I band for conformational studies.* Biopolymers: Original Research on Biomolecules, 1988. **27**(11): p. 1749-1760.

32. Blaney Davidson, E., et al., *Correction: Increase in ALK1/ALK5 Ratio as a Cause for Elevated MMP-13 Expression in Osteoarthritis in Humans and Mice*. Vol. 182. 2009. 7937-45.

33. Kim, S.H., et al., *Fabrication of duck's feet collagen–silk hybrid biomaterial for tissue engineering.* International journal of biological macromolecules, 2016. **85**: p. 442-450.

34. Boryskina, O.P., et al., *Energies of peptide–peptide and peptide–water hydrogen bonds in collagen: Evidences from infrared spectroscopy, quartz*

piezogravimetry and differential scanning calorimetry. Journal of Molecular Structure, 2007. **827**(1): p. 1-10.

35. Barth, A., *The infrared absorption of amino acid side chains.* Progress in Biophysics and Molecular Biology, 2000. **74**(3): p. 141-173.

36. Parikh, S.J., et al., *Evaluating Glutamate and Aspartate Binding Mechanisms to Rutile (α-TiO2) via ATR-FTIR Spectroscopy and Quantum Chemical Calculations.* Langmuir, 2011. **27**(5): p. 1778-1787.

37. Liu, Y., et al., *Enhancement in dentin collagen's biological stability after proanthocyanidins treatment in clinically relevant time periods.* Dental materials : official publication of the Academy of Dental Materials, 2013. **29**(4): p. 485-492.

38. Miles, C.A., et al., *The Increase in Denaturation Temperature Following Cross-linking of Collagen is Caused by Dehydration of the Fibres.* Journal of Molecular Biology, 2005. **346**(2): p. 551-556.

39. Geneva, I.I., et al. *Normal body temperature: a systematic review*. in *Open Forum Infectious Diseases*. 2019. Oxford University Press US.

40. Grover, C.N., et al., *Crosslinking and composition influence the surface properties, mechanical stiffness and cell reactivity of collagen-based films.* Acta biomaterialia, 2012. **8**(8): p. 3080-3090.

41. Manferdini, C., et al., *Adipose-derived mesenchymal stem cells exert antiinflammatory effects on chondrocytes and synoviocytes from osteoarthritis patients through prostaglandin E2.* Arthritis & Rheumatism, 2013. **65**(5): p. 1271-1281.

42. Zhou, J., et al., *Adipose derived mesenchymal stem cells alleviated osteoarthritis and chondrocyte apoptosis through autophagy inducing.* Journal of cellular biochemistry, 2019. **120**(2): p. 2198-2212.

43. Barlian, A., et al., *Chondrogenic differentiation of adipose-derived mesenchymal stem cells induced by L-ascorbic acid and platelet rich plasma on silk fibroin scaffold.* PeerJ, 2018. **6**: p. e5809-e5809.

Chapter Seven

FABRICATION OF TARGETED COLLAGEN MICROSPHERES FOR MITIGATION OF POSTTRAUMATIC OSTEOARTHRITIS

7.1 Introduction

Osteoarthritis (OA) is a progressively degenerative joint disease leading to loss of articular cartilage and creating joint instability. This degradation can cause severe disability; today over 27 million Americans have been diagnosed with clinical OA [1]. About 12% of symptomatic OA can be attributed to posttraumatic osteoarthritis (PTOA) at a cost to the U.S. of around $3 billion [2, 3]. In the events following PTOA, chondrocyte cells found in the articular cartilage in close proximity to the trauma undergo cell death namely through necrosis. Cells surrounding the trauma site tend to exhibit a hypertrophic phenotype that expresses a host of catabolic enzymes that can further dysregulate chondrocyte cells eventually leading to apoptosis and cause degradation of articular cartilage extracellular matrix (ECM) [4-7]. Interleukin-1β (Il-1β) is particularly detrimental to chondrocyte cells in the progression of PTOA. Catabolic chondrocytes begin to express cytokines and chemokines like tumor necrosis factor (TNF)-α, Il-1β, Il-6, Il-8, and receptor activator of NF-kβ ligand (RANKL), which perpetuates and enhances articular damage [8-10]. Work has also shown Il-1β to be a major contributor in the progression of PTOA, particularly in the upregulation of known collagenases like matrix metalloproteinases -3 & -13 [11] and is also associated with the downregulation of articular cartilage components like type II collagen and

aggrecan by inhibiting anabolic activities of chondrocytes [12-14]. Reactive oxygen species (ROS) are a grouping of molecules and free radicals with one unpaired electron derived from molecular oxygen [15]. Produced ROS can dysregulate or signal unwanted or unintended mechanistic pathways. ROS begins to accumulate after mechanical impact and are known to drive chondrocyte cells into an enhanced metabolic state [16-18]. With chondrocytes already synthesizing procatabolic and proinflammatory products, the enhanced metabolic activity leads to further cartilage degradation. ROS has been shown to enhance activation of procatabolic pathways like nuclear factor-kB (NF-kB), and mitogen-activated protein kinases (MAPK) like extracellular signal-regulated kinase 1/2 (Erk 1/2), p38 cascade, and c-Jun N-terminal kinases (JNK) [4, 19, 20]. Specifically, the cascade of the NF-kβ signaling pathway leads to detrimental effects on the articular environment. This pathway leads to the secretion of MMP-1, -2, -3, -7, -8, -9, -13, and -14 and a disintegrin and metalloproteinase with thrombospondin motifs (ADAMTS)-1, -3, -4 and -5 which results in cartilage breakdown [8, 21, 22]. Work by Ansari et al. provided evidence of increased ROS production levels and mitochondrial dysfunction in primary human chondrocyte cells stimulated with Il-1β (5 ng/ml) in culture [23]. Yang et al. also reported similar results observing cell viability and ROS production in primary human chondrocyte cells cultured with Il-1β (10 ng/ml) [24].

Current treatments for PTOA are largely palliative and the advanced progression of PTOA can lead to joint replacement [25]. Typically, a discrete joint trauma is a common impetus for PTOA with the younger population being more

commonly affected by PTOA which may be due to the younger population having a more active lifestyle [26]. Commonly after a joint trauma associated with PTOA, progression, disruption, and penetration of the glycan surface occurs exposing the underlying articular cartilage ECM [27]. This ECM is mainly composed of type II collagen which provides a unique physical characteristic of PTOA damage that can be utilized in the challenge of mitigating PTOA's progressive destruction [28]. By using type II collagen as a targeted binding site for a therapeutic, this can provide therapeutic delivery at the damaged site rather than in the intraarticular space [29].

The use of targeting type II collagen in subjects with PTOA trauma has historical standing. Cho et al. developed a non-invasive type II collagen antibody conjugated to nanoliposomes encapsulated with a fluorescent dye which was used as a diagnostic tool to determine the early stages of PTOA and cartilage injury [30]. In a two-week study, they were able to show an increase in osteoarthritic changes through histopathology in a mechanical load PTOA mouse model which correlated with an increased fluorescence through imaging.

Curcumin is a naturally derived molecule from turmeric. It is well known for its anti-inflammatory and free radical scavenging abilities [31]. It has also been investigated as a treatment for OA and PTOA [31-33]. It is believed that curcumin can suppress the activator protein-1 and nuclear factor kappa B pathways which are known to stimulate the synthesis of a host of proinflammatory cytokines and interleukins, like Il-1β, known to lead to chondrocyte apoptosis and articular cartilage ECM degradation [33-35].

Research into the use of mesenchymal stem cells (MSCs) in the treatment of PTOA have also been investigated [36]. MSCs can play an interesting role in the regeneration of damaged articular cartilage. It has been reported that the use of bioactive agents like hyaluronic acid, transforming growth factor-β and insulin growth factor-1 all help to promote differentiation of MSCs down a chondrocytic lineage [36]. By creating a collagenous transporter for MSCs loaded with bioactive agents to promote chondrocyte differentiation, this may create a structurally sound 3-dimensional scaffold with a proper microenvironment which can provide the cells with mechanical cues along with the cues from the bioactive agents for the development of similar tissue to native articular cartilage when implemented to the damaged site [36, 37].

We have developed a type II collagen monoclonal antibody conjugated to collagen microspheres (CMs) immersed in curcumin to specifically bind to exposed type II collagen that may arise from mechanical impacts or chemical reduction of the articular surface from PTOA events. The CMs provide an opportunity for the release of the bioactive agent, curcumin, into the damaged region to mitigate PTOA progression. Type II collagen antibody binding studies along with Il-1β stimulated human chondrocyte work was performed. Work with MSCs was also performed. MSC adherence to CMs was observed via light microscopy and live/dead cell staining was utilized to determine the viability of CMs to be utilized as a cellular transporter.

7.2 Materials and methods

7.2.1 Fabrication of liquid collagen

Porcine collagen type I (10 mg/ml, Sunmax Biotechnology,Taiwan) was precipitated using 1.04 M sodium chloride (NaCl, ≥99.0%, Sigma Aldrich, MO). The precipitated collagen solution was then centrifuged at 3,500 rpm for 15 minutes. A white collagen pellet was formed at the bottom of the tube and the supernatant was poured off leaving a 150 mg collagen pellet. Fifteen ml of 0.5 M glacial acetic acid (≥99.7%, Fisher Chemical, KS) was added to the collagen pellet and allowed to sit overnight at room temperature to let the collagen pellet dissolve. The collagen/acetic acid solution was then placed in a 15 ml, 10 kDa molecular weight cutoff dialysis cassette (Thermo Scientific, IL) and immersed in an ethylenediaminetetraacetic acid (35mM, EDTA, Fisher Chemical, KS)/ H_2O solution with a pH of 7.5 using sodium hydroxide (10 N, NaOH, Ricca Chemical Co., TX) [38]. The pH of the EDTA solution was checked and maintained at 7.5 daily until the pH no longer fluctuated from 7.5. The liquid collagen (LC) solution was then removed and pH was tested to ensure it was set at 7.5.

7.2.2 Collagen microsphere Fabrication

Fifty ml of olive oil (Sigma Aldrich, MO) and 0.35% (v/v) span-80 (Sigma Aldrich, MO) was added to a 100 ml round bottom flask. A 4 cm stir bar was added to the flask and placed on a stir/hot plate and set to 1150 rpm. The emulsion was allowed to equilibrate for 10 minutes. After 10 minutes, 1 ml of the LC solution was added dropwise using an 18-gauge plastic cannula. One hour

after the LC addition, the stir plate temperature was set to 35°C and allowed to stir for 1 hour. After the emulsion time was reached the collagen/oil solution was poured into a 50 ml centrifuge tube and centrifuged at 5000 rpm for 5 minutes. The oil was then removed and 25 ml 50% acetone (Fisher Chemical, KS) and 100 μl tween-20 (Sigma Aldrich, MO) was added to the tube to wash the collagen microspheres (CMs). The solution was vortexed for 1 minute and sonicated for 3 minutes. The solution was then centrifuged at 5,000 rpm for 5 minutes. The sample was washed 3 times using 50% acetone and tween-20 and then was washed 3 times using 1x PBS (Sigma Aldrich, MO). The CMs were stored in 15 ml 1x PBS and placed in a 4°C refrigerator.

7.2.3 Anti-Collagen Type II Antibody Conjugation to Collagen Microspheres and Incubation with Curcumin

Monoclonal mouse collagen type II antibody (CIIMAb, Invitrogen, Thermo Fisher Scientific, MA5-12789) was conjugated to fabricated CMs with genipin. To conjugate, approximately 100 CMs in 100 μl PBS was introduced to 16.7 μl 35 mM genipin and incubated for 2 hours. After 2 hours, 1.67 μl CIIMAb was added to the CM/genipin solution and allowed to incubate for 24 hours on a shaker table at 225 RPM. Samples were washed three times with PBS and stored at 4°C.

CMs with curcumin (Sigma Aldrich, MO) were incubated for 24 hours in the specified (w/v) curcumin solution. After 24 hours, curcumin incubated CMs were washed 3 times using cellularly relevant media.

7.2.4 Semi-Quantitative CIIMAb Conjugation Analysis

After CIIMAb-CM conjugation, anti-mouse IgG, superclonal recombinant secondary antibody, alexa fluor 488 (FSSAB, Invitrogen, Thermo Fisher, A28175) was used to provide information on the ability of genipin to conjugate CIIMAbs to CMs. Six µl FSSAb was added to 100 CIIMAb-CMs and incubated on a shaker table set to 225 RPM at room temperature for 1 hour. After 1 hour, samples were washed three times using PBS. A spectrofluorometer plate reader (Cytation 5, BioTek, VT) was used to read the fluorescent intensity of FSSAb-CIIMAb-CMs at 499 nm excitation and 520 nm emission.

7.2.5 Articular Cartilage Preparation

Articular cartilage was harvested from euthanized swine from the School of Medicine at the University of Missouri. The articular cartilage was removed from the end of the femoral surface and was punched using a 4 mm cylindrical tissue punch. To damage the surface of articular cartilage, the articular cartilage was exposed to 0.25% trypsin-EDTA for 1 hour at 37°C. The articular cartilage was then washed with PBS and subsequently blocked with 5% horse serum for 1 hour at 37°C. The 100 CIIMAb-CMs were incubated with 200 µl FITC (1 mg/ml) for 1 hour. After 1 hour, the samples were washed and rehydrated with PBS. Samples were then added onto the surface of the articular cartilage discs and incubated at 37°C for 30 minutes. The articular cartilage discs were then washed

three times with PBS and imaged using fluorescent microscopy using a Cytation 5 (BioTek, VT) Cell Imaging Multi-Mode Reader using a GFP filter.

7.2.6 Cell Culture

7.2.6.1 Human Chondrocyte Cells

Human chondrocyte cells (CHON-001, ATCC, VA) were used to assess cell viability and ROS production when incubated with CIIMAb-CMs. The cells were cultured at 37°C and 5% CO_2 in Dulbecco's Modified Eagle's Medium (ATCC, 30-2002), 10% (v/v) heat-inactivated fetal bovine serum (Gibco, Thermo Fisher, A3840001), and 0.1mg/ml geneticin (Gibco, Thermo Fisher, 10131035). Cells were passed at confluency and media was exchanges as needed. Studies with these cells were between cell passages 5 and 10.

7.2.6.2 Murine Mesenchymal Stem Cells

Murine mesenchymal stem cells (MSC, C57BL/6, Cyagen, CA) were used to determine the time course it would take for the cell to become adherent onto CMs. The cells were cultured at 37°C and 5% CO_2 in Dulbecco's Modified Eagle's Medium (Gibco, Thermo Fisher), 10% fetal bovine serum (Sigma Aldrich, MO), and 1% penicillin-streptomycin (Invitrogen, Thermo Fisher). Cells were passed and provided with fresh media as required. MSCs used in this study were passage 6.

7.2.7 WST-1 Assay

A WST-1 cell proliferation assay (Roche, Sigma Aldrich, MO) was utilized to determine the activity of human chondrocytes with CIIMAb-CMs incubated with various concentrations of curcumin. Cells were plated at a concentration of $5x10^3$ cells per well and allowed to become confluent in a Costar 96-well plate. After the cells were confluent they were stimulated with 10 ng/ml Il-1β for 24 hours prior to the addition of CMs to evoke a simulated osteoarthritic cellular response [32]. The cellular activity was analyzed 24 hours after the addition of CMs to the cells. WST-1 reagent was added to each well and the plates were incubated at 37°C for 4 hours. After 4 hours, the media was removed from each well and absorbance readings were taken at 450 nm, with a 600 nm filter, using a spectrofluorometer plate reader (Cytation 5, BioTek, VT).

7.2.8 ROS Assay

An OxiSelect ROS assay (Cell Biolabs, CA) was used to determine produced intracellular ROS. Again, $5x10^3$ human chondrocyte cells per well were stimulated with 10 ng/ml Il-1β for 24 hours in a 96-well plate after confluency was reached. After 24-hours of Il-1β stimulation, each well was washed with DPBS, and then 1x 2',7'-dichlorodihydrofluorescein diacetate (DCF-DA)/DMEM was added and incubated for 1-hour. After 1-hour, the DCF-DA/DMEM was removed and washed two times with DPBS. CIIMAb-CMs incubated in curcumin were then introduced to the plate for 24 hours. Cell lysis buffer was then added to each well and allowed to incubate for 5 minutes. Each well was then transferred to a new

well plate and read using a Cytation 5 spectrofluorometer (BioTek, VT) at 480 nm excitation and 530 nm emission.

7.2.9 Cell Imaging and Live/Dead Cell Staining

MSCs were added to a Costar 24-well low attachment well plate along with media incubated CMs. The MSC/CM incubation was imaged using an Olympus IX50 inverted light microscope (Olympus, PA) using CellSense software.

Live/dead cell staining was performed using 3 μM calcein AM and 5 μM propidium iodide. Both calcein AM and propidium iodide were added to each well and incubated for 10 minutes before imaging. Cell/CMs were imaged with fluorescent microscopy using a Cytation 5 (BioTek, VT) Cell Imaging Multi-Mode Reader using either GFP or Texas Red filters.

7.3 Results

7.3.1 Semi-Quantitative data of CIIMAb conjugation to CMs

The use of FSSAb, a specific fluorescent secondary antibody to CIIMAb, was used to determine if the use of covalent crosslinker, genipin, provided an increased attachment of CIIMAbs to CMs over adsorption of CIIMAbs to CMs. Naturally, an increased fluorescent signal correlates to an increased concentration of CIIMAbs on the CMs. Figure 7.1 provides evidence that the use of genipin to conjugate CIIMAbs to CMs does significantly outperform adsorption

alone. A background signal was also determined to verify possible adhesion of FSSAb to CMs without the inclusion of either genipin or CIIMAbs.

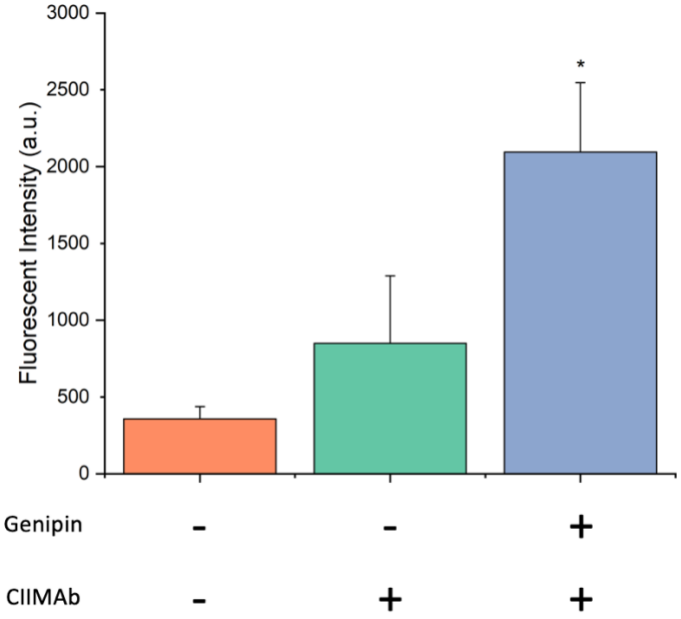

Figure 7.1. CIIMAb binding characterization through quantification of FSSAb attachment. Excitation at 499 nm and emission at 520 nm. n = 6. * = P<0.01.

7.3.2 Binding of CIIMAbs-CMs to Articular Cartilage

Proteolytic digestion of the glycan surface on the articular cartilage was used to simulate articular damage and expose underlying type II collagen [39]. This was performed to determine if CIIMAb-CMs can in fact bind to exposed type II collagen. Figure 7.2 shows qualitative images of CIIMAb-CMs and CMs only exposed to both damaged and normal porcine cartilage. It is visually apparent that neither CIIMAb-CMs nor CMs only bound to the surface of normal cartilage. While both the CIIMAb-CMs and CMs only both bound to the surface of the damaged cartilage. It does appear however that the CIIMAb-CMs had more bound to the surface of the damaged cartilage relative to CMs only.

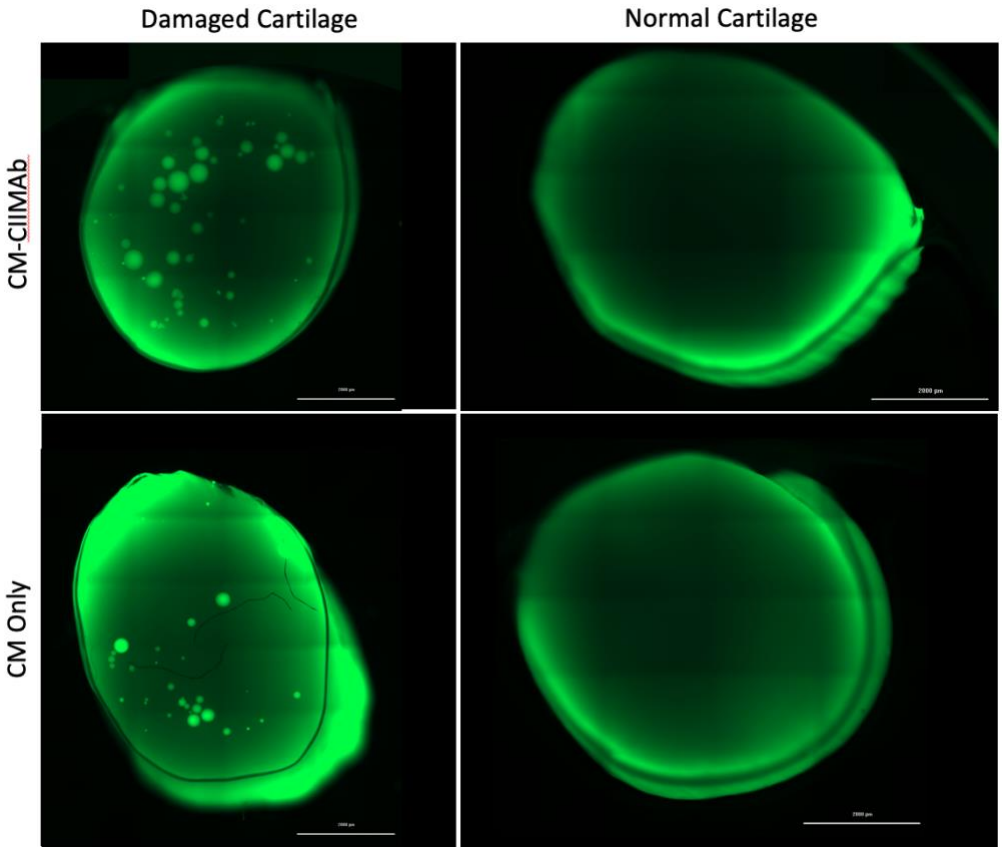

Figure 7.2. Fluorescent micrographs of CIIMAb-CMs and CMs only exposed to both damaged and normal cartilage. Scale bar = 0.1 cm

7.3.3 Cell Proliferation Assay

A WST-1 cell proliferation assay, which measures cellular metabolic activity, was utilized to determine how Il-1β stimulated chondrocyte cells interact with CIIMAb-CMs supplemented with various concentrations of curcumin for a 24-hour incubation period. The Il-1β stimulated chondrocyte cells were utilized in order to simulate osteoarthritic activity. In Figure 7.3, all groups treated with Il-1β had an increased cellular activity relative to the untreated cells. The only group to have a higher average cell activity than the treated cells group was the CIIMAb-CMs group treated with 6% (w/v) curcumin.

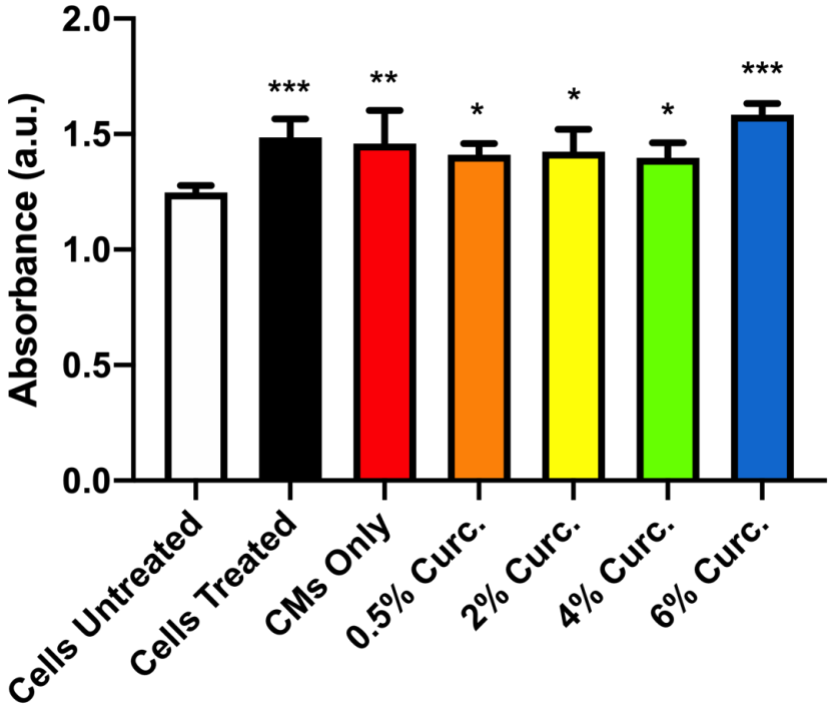

Figure 7.3. A 24-hour WST-1 assay with Il-1β stimulated human chondrocyte cells. n=6.
* = P<0.05; ** = P<0.01; *** = P<0.001

7.3.4 ROS Assay

An OxiSelect ROS assay was used to determine the intracellular ROS production of Il-1β stimulated human chondrocyte cells after 24-hours of incubation with CIIMAb-CM supplemented with various concentrations of curcumin in Figure 7.4. After the 24-hour incubation, the treated cells had higher intracellular production than the untreated cells. Interestingly the 4% & 6% (w/v) curcumin group had a lower average ROS production relative to the treated cells.

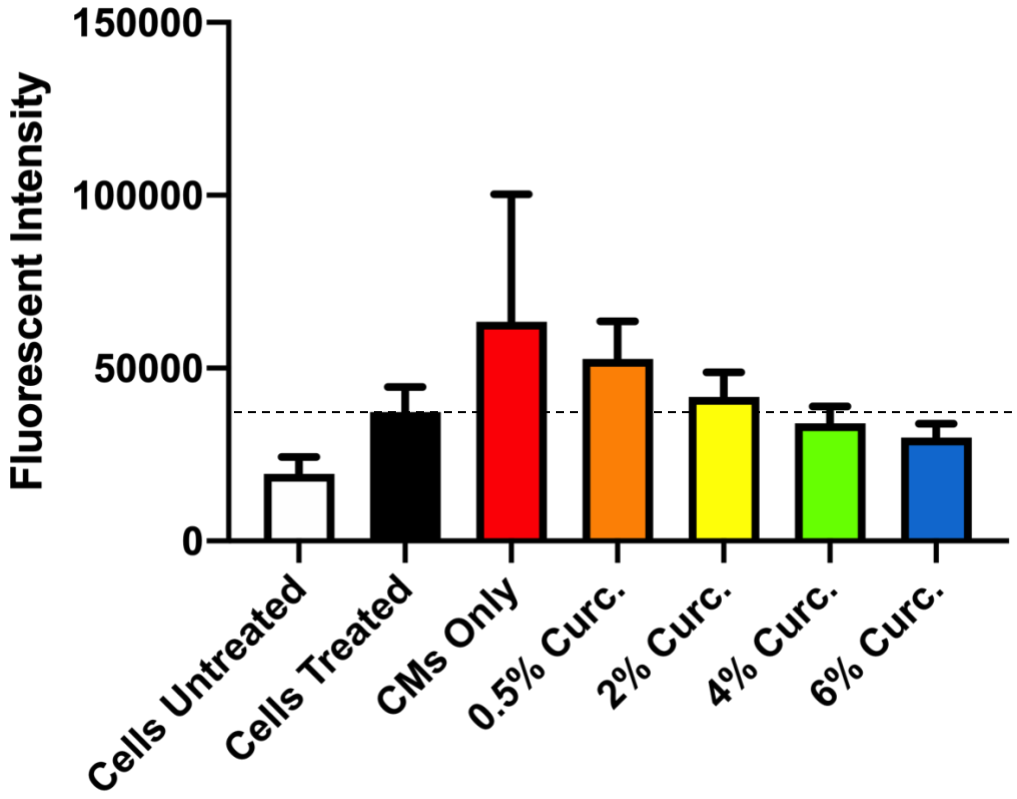

Figure 7.4. A 24-hour OxiSelect Intracellular ROS assay with Il-1β stimulated human chondrocyte cells. n=6.

7.3.5 Imaging of MSC-CMs

Imaging over 2 weeks was performed to observe the interaction between CMs and MSCs as shown in Figure 7.5A-F. Figure 7.5B, at 24-hours of incubation, MSCs are attaching to the CMs. Figure 7.5C, at 48-hours the MSCs appear to be completely covering the CMs surface. Figure 7.5D, at 72-hours the MSC covered CMs appeared to aggregate into large clusters of MSC-CMs. Growth can continue to be observed at 1 week, in Figure 7.5E, of culture as the MSC-CM clusters continue to grow. At 2 weeks, Figure 7.5F, MSC-CMs became large enough that light had difficulty passing through the whole MSC-CM cluster.

Figure 7.6 inlay provides a 20x image giving better resolve to the CMs that are entrapped within the cluster at 2-weeks. Figure 7.7 displays live/dead cell staining images of MSC-CMs. At 24 hours in Figures 7A &7B, low clustering was observed with viable cells seen on the surface. At 48 hours, in Figures 7C & 7D, clustering of CMs with MSCs were beginning to form. Some red fluorescence can also be seen which appears to be mostly in the CMs and does not appear to correlate to dead cells. In Figure 7.7E, the cluster is largely living cells; it appears that the center may have some cellular remnants or most likely as shown in Figure 7.7E, some of the propidium iodide was able to infiltrate the CMs giving rise to the red color.

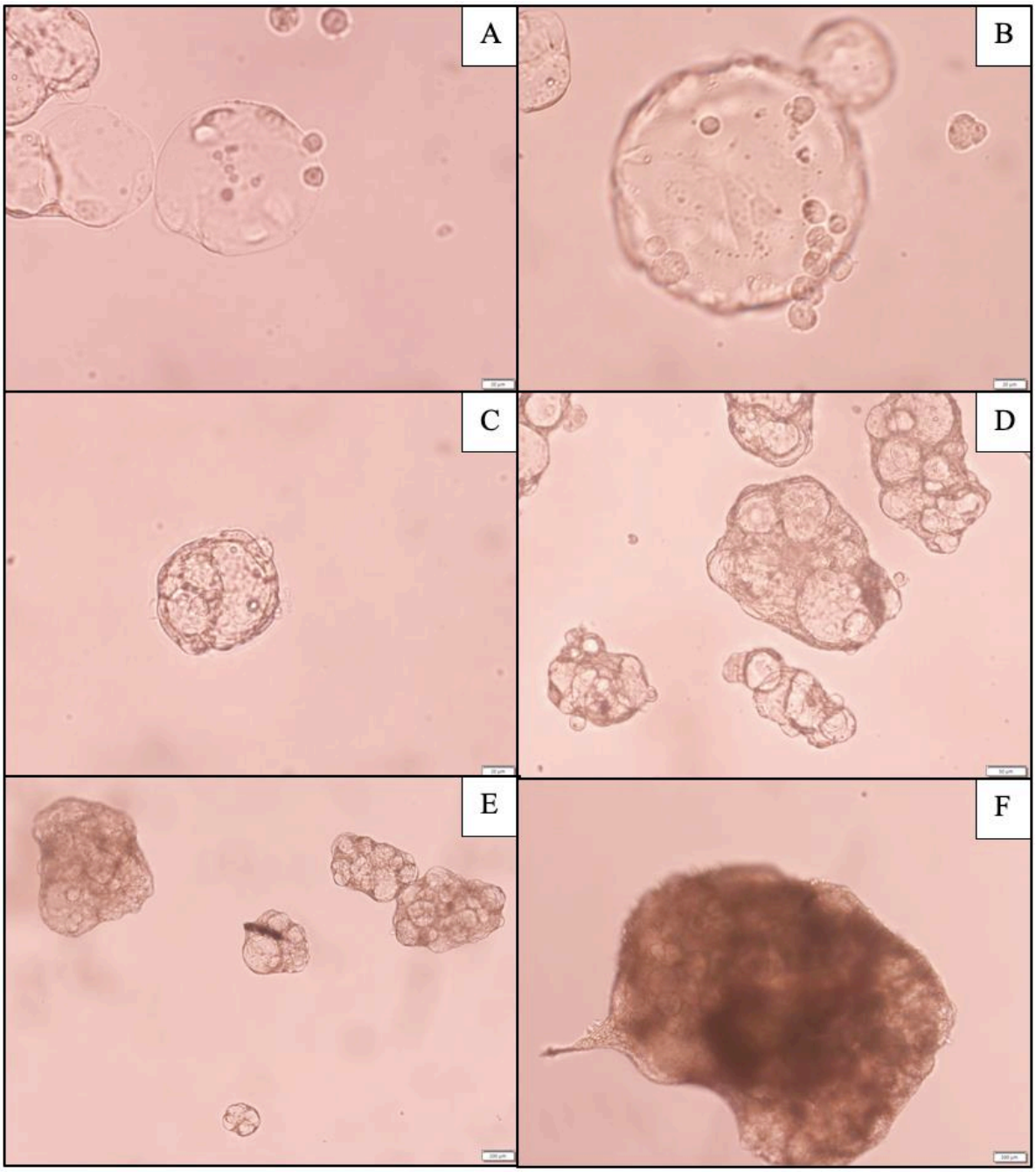

Figure 7.5. Light micrograph images of CMs incubated with MSC on a low attachment well plate for (A) 5 hours; (B) 24 hours; (C) 48 hours; (D) 72 hours; (E) 1 week; (F) 2 weeks. (A-C) = 40x; (D) = 10x; (E-F) = 4x.

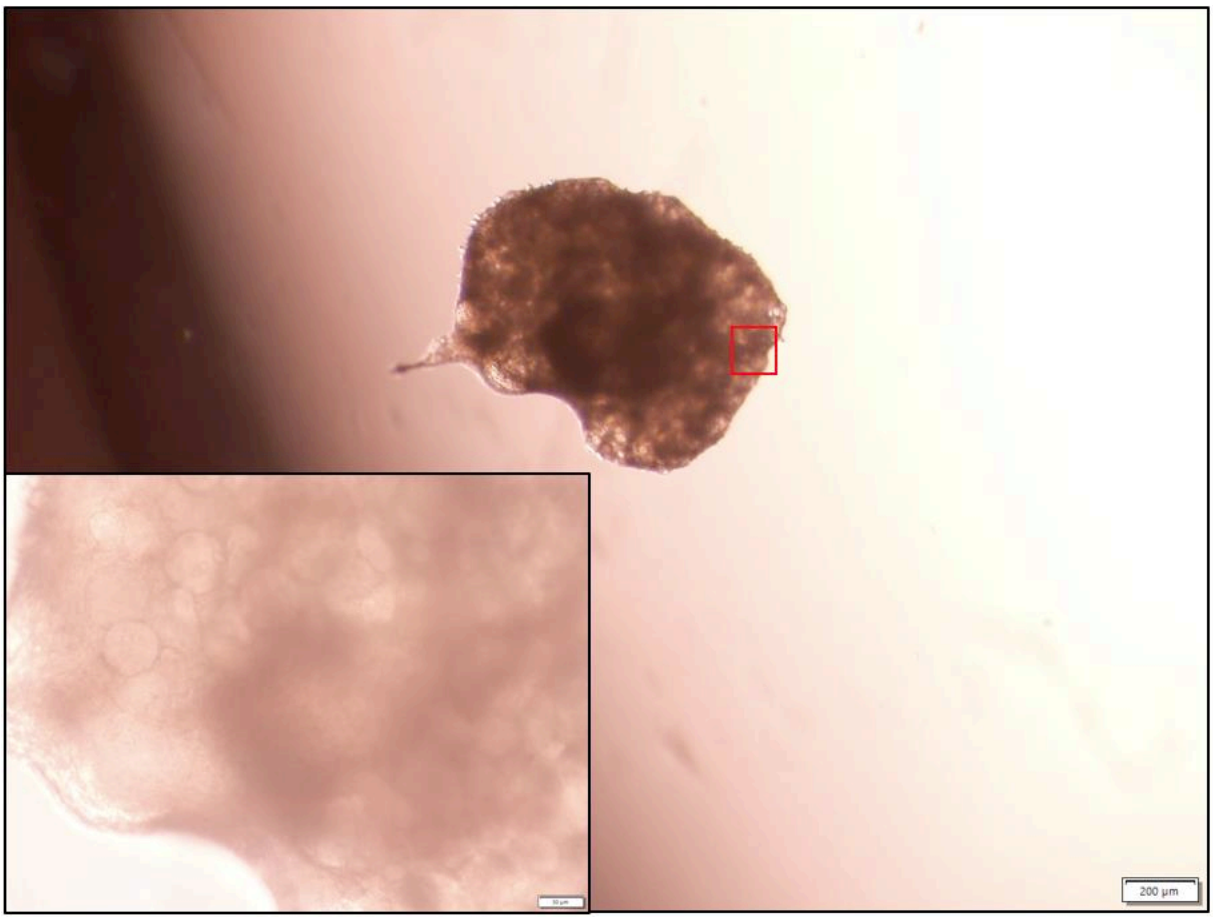

Figure 7.6. 4x Light micrograph of MSC-CM cluster at 2-weeks. Red box indicated the region imaged for the inlay. Inlay = 20x.

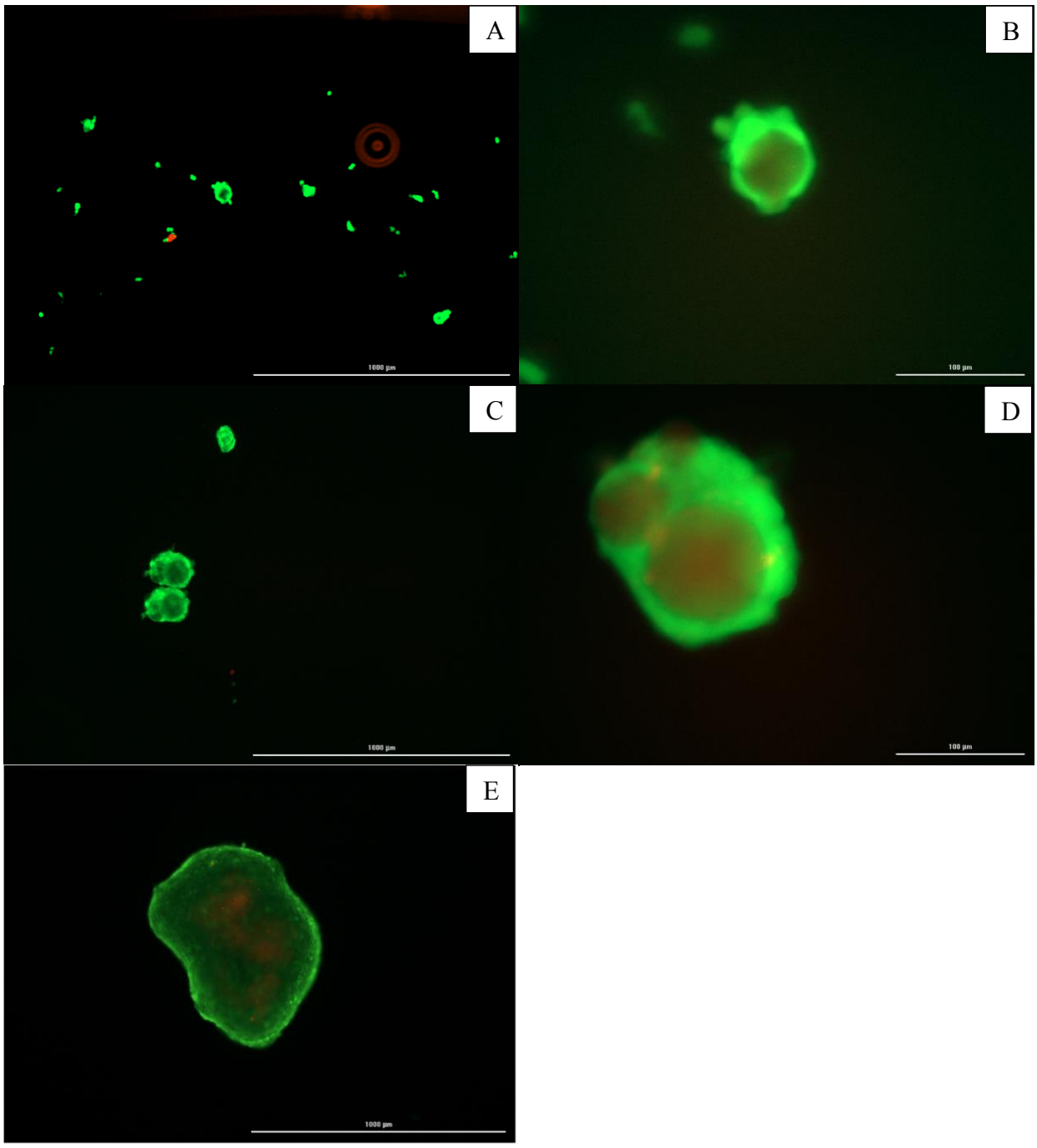

Figure 7.7. fluorescent micrograph of live/dead cell staining of MSC-CM cluster at (A,B) 24 hours; (C,D) 48 hours; (E) 2 weeks with calcein AM and propidium iodide. GFP and Texas Red filters were used.

7.4 Discussion

Previous work focused on the development of CMs for general injectable musculoskeletal applications [40]. In this work, we have developed an antibody-based CM scaffold to target damaged cartilage. The CMs may have the potential to mitigate detrimental effects that can arise in dysregulated catabolic chondrocyte cells exposed to a PTOA environment. We have also taken preliminary steps into creating a CM transporter for MSCs which may be valuable for tissue regeneration after stabilization of the catabolic environment has occurred.

We were able to demonstrate that by conjugating the CIIMAbs to CMs using a covalent crosslinker, genipin, we had a higher overall attachment to the CMs in comparison to adsorption of the CIIMAbs to the CMs.

The glycan surface of the articular cartilage becomes disrupted as events like PTOA occur leaving exposure of the underlying articular cartilage ECM components like type II collagen and can even expose and penetrate through to the mineralized bone region [41]. We also demonstrated that in a simulated osteoarthritic cartilage model both the CIIMAb-CMs and CMs only were able to bind to the surface of the damaged cartilage, albeit CIIMAb-CMs appeared to bind at a higher percentage. Neither the CIIMAb-CMs nor the CMs only were able to bind to normal undamaged cartilage. Taking the work from Cho et al. which transitioned their antibody conjugated liposomes from an explanted trypsin *in vitro* cartilage lesion model to an *in vivo* mouse model with translational results, this provides a sound basis for the ability of CIIMAb-CMs to target and

deliver therapeutic bioactive agents to damaged regions of articular cartilage [30]. Another observable advantage of binding CIIMAB-CMs to damaged regions of articular cartilage is their ability to create a physical barrier between the exposed damaged tissue and the articulating surface by binding to the exposed damaged tissue. This creates a potential protective layer and prevents further articulating mechanical damage at the already damaged site.

Il-1β is a commonly overexpressed proinflammatory cytokine in damaged cartilage which has profound effects on chondrocytes and the surrounding ECM and is thought to be one of two main driving cytokines in disease progression [42]. Exposing Il-1β to chondrocyte cells in monolayer culture can simulate the catabolic response seen in PTOA impacts like an increased expression of catabolic cytokines and ROS production which are two major factors that progressively degrade articular cartilage ECM and lead to chondrocyte cell death [25, 43].

ROS has been linked to significant cartilage degradation through increased activation of known catabolic pathways nuclear factor-kB and several mitogen-activated protein kinase pathways [19, 20]. Accumulation of ROS has been shown to enhance chondrocyte metabolic activity after injury and also contribute to cell death [4].

Observing Il-1β stimulated human chondrocyte cells metabolic activity, we saw an increase in metabolic activity with all CIIMAb-CM groups along with the positive control relative to the untreated cells 24-hours after exposure to Il-1β. This was not necessarily unexpected as increased metabolic activity shortly after

exposure is a hallmark of damaging the environment [16-18]. To further assess the curcumin loaded CIIMAb-CMs, an assay to study intracellular ROS production 24 hours after exposure to Il-1β was conducted to determine if the curcumin was playing a role in limiting ROS production.

While examining ROS production, we saw that the CIIMAb-CM group supplemented with 4% and 6% curcumin reduced intracellular ROS relative to the positive control group. While taking both the cellular metabolic activity and ROS data into correlation with the CIIMAb-CMs supplemented with 4% & 6% curcumin, we observed chondrocyte cells that have an enhanced metabolic activity relative to untreated cells while having a lower overall intracellular ROS production relative to treated cells which lends evidence to the chondrocyte cells having a reduced catabolic response when coming into contact with CIIMAb-CMs supplemented with 4% & 6% curcumin.

Working with MSCs and CMs, the MSCs appeared to preferentially adhere to the surface of the CMs at about 24 hours of incubation. The MSCs appear to completely cover most CMs at 48 hours. They also began to aggregate with each other and also aggregate into MSC-CM clusters. At 48 hours and also at 2-weeks, live/dead cell staining provided evidence of a largely living cluster of cells with some possible cellular remnants in the center of the cluster. The dead cells may have been due in part to poor diffusion of cellular media into the core of the cluster. Another possibility could be the porous structure of the CMs allowed the infiltration of propidium iodide and had some adsorption to the CMs. It does appear the red stain clustered in and around the CMs. Between 24 to 48 hours

CMs appear to be viable transporters of MSCs to damaged cartilage without forming large clusters. More work needs to be performed to investigate but these MSC-CMs may be a suitable injectable which targets articular cartilage regeneration. Supplementation of the CMs with bioactive agents like hyaluronic acid, transforming growth factor-β and insulin growth factor-1, which help to progress differentiation of MSCs down a chondrogenic lineage would be advantageous [36]. With the MSC-CMs able to cluster, this may allow for clusters to form on damaged regions of cartilage which may have the capacity to fill articular defects after MSC-CMs are introduced into the articular environment.

7.5 Conclusion

In conclusion, we have demonstrated the ability of CMs to be labeled with collagen type II targeting antibodies. The CIIMAb-CMs preferentially bound to the damage induced cartilage. The addition of curcumin appeared to reduce ROS production and increase cellular metabolic activity. MSCs preferential adhered to CMs and grew large cellularly viable clusters over 2-weeks of incubation. The use of CIIMAb-CMs may have potential uses for targeting damaged cartilage and delivering therapeutic agents at the damaged site. While MSC-CM clusters may provide potential regeneration of tissue.

7.6 References

1. Neogi, T., *The epidemiology and impact of pain in osteoarthritis.* Osteoarthritis and cartilage, 2013. **21**(9): p. 1145-1153.

2. Schenker, M.L., R.L. Mauck, and S. Mehta, *Pathogenesis and prevention of posttraumatic osteoarthritis after intra-articular fracture.* Journal of the American Academy of Orthopaedic Surgeons, 2014. **22**(1): p. 20-28.

3. Brown, T.D., et al., *Posttraumatic osteoarthritis: A first estimate of incidence, prevalence, and burden of disease.* Journal of Orthopaedic Trauma, 2006. **20**(10): p. 739-744+747-748.

4. Riegger, J. and R.E. Brenner, *Pathomechanisms of Posttraumatic Osteoarthritis: Chondrocyte Behavior and Fate in a Precarious Environment.* International Journal of Molecular Sciences, 2020. **21**(5): p. 1560.

5. Riegger, J. and R.E. Brenner, *Evidence of necroptosis in osteoarthritic disease: investigation of blunt mechanical impact as possible trigger in regulated necrosis.* Cell Death & Disease, 2019. **10**(10): p. 1-12.

6. Stevens, A.L., et al., *A sodium dodecyl sulfate–polyacrylamide gel electrophoresis–liquid chromatography tandem mass spectrometry analysis of bovine cartilage tissue response to mechanical compression injury and the inflammatory cytokines tumor necrosis factor α and interleukin-1β.* Arthritis & Rheumatism: Official Journal of the American College of Rheumatology, 2008. **58**(2): p. 489-500.

7. Van der Kraan, P. and W. Van den Berg, *Chondrocyte hypertrophy and osteoarthritis: role in initiation and progression of cartilage degeneration?* Osteoarthritis and cartilage, 2012. **20**(3): p. 223-232.

8. Rigoglou, S. and A.G. Papavassiliou, *The NF-κB signalling pathway in osteoarthritis.* The International Journal of Biochemistry & Cell Biology, 2013. **45**(11): p. 2580-2584.

9. Ulivi, V., et al., *p38/NF-kB-dependent expression of COX-2 during differentiation and inflammatory response of chondrocytes.* Journal of Cellular Biochemistry, 2008. **104**(4): p. 1393-1406.

10. B Marcu, K., et al., *NF-κB signaling: multiple angles to target OA.* Current drug targets, 2010. **11**(5): p. 599-613.

11. Aida, Y., et al., *The effect of IL-1β on the expression of matrix metalloproteinases and tissue inhibitors of matrix metalloproteinases in human chondrocytes.* Life Sciences, 2005. **77**(25): p. 3210-3221.

12. Kapoor, M., et al., *Role of proinflammatory cytokines in the pathophysiology of osteoarthritis.* Nature Reviews Rheumatology, 2010. **7**: p. 33.

13. Goldring, M.B., et al., *Transcriptional suppression by interleukin-1 and interferon-γ of type II collagen gene expression in human chondrocytes.* Journal of cellular biochemistry, 1994. **54**(1): p. 85-99.

14. Saklatvala, J., *Tumour necrosis factor α stimulates resorption and inhibits synthesis of proteoglycan in cartilage.* Nature, 1986. **322**(6079): p. 547-549.

15. Turrens, J.F., *Mitochondrial formation of reactive oxygen species.* The Journal of physiology, 2003. **552**(2): p. 335-344.

16. Wolff, K.J., et al., *Mechanical stress and ATP synthesis are coupled by mitochondrial oxidants in articular cartilage.* Journal of Orthopaedic Research, 2013. **31**(2): p. 191-196.

17. Coleman, M.C., et al., *Targeting mitochondrial responses to intra-articular fracture to prevent posttraumatic osteoarthritis.* Science translational medicine, 2018. **10**(427).

18. Lee, R., et al., *The effect of mechanical stress on cartilage energy metabolism.* Biorheology, 2002. **39**(1, 2): p. 133-143.

19. Son, Y., et al., *Mitogen-activated protein kinases and reactive oxygen species: how can ROS activate MAPK pathways?* Journal of signal transduction, 2011. **2011**.

20. Pantano, C., et al., *Redox-sensitive kinases of the nuclear factor-κB signaling pathway.* Antioxidants & redox signaling, 2006. **8**(9-10): p. 1791-1806.

21. Goldring, M.B. and K.B. Marcu, *Cartilage homeostasis in health and rheumatic diseases.* Arthritis Research & Therapy, 2009. **11**(3): p. 224.

22. Sebastian, A., et al., *Comparative Transcriptomics Identifies Novel Genes and Pathways Involved in Post-Traumatic Osteoarthritis Development and Progression.* International journal of molecular sciences, 2018. **19**(9): p. 2657.

23. Ansari, M.Y., et al., *Parkin clearance of dysfunctional mitochondria regulates ROS levels and increases survival of human chondrocytes.* Osteoarthritis and cartilage, 2018. **26**(8): p. 1087-1097.

24. Yang, G., et al., *Polydatin reduces IL-1β-induced chondrocytes apoptosis and inflammatory response via p38 MAPK signaling pathway in a rat model of osteoarthritis.* Int J Clin Exp Med, 2017. **10**(2): p. 2263-73.

25. Borrelli Jr, J., et al., *Understanding Articular Cartilage Injury and Potential Treatments.* Journal of orthopaedic trauma, 2019. **33**: p. S6-S12.

26. Kramer, W.C., K.J. Hendricks, and J. Wang, *Pathogenetic mechanisms of posttraumatic osteoarthritis: opportunities for early intervention.* International journal of clinical and experimental medicine, 2011. **4**(4): p. 285.

27. D., A.D., et al., *Post-traumatic osteoarthritis: Improved understanding and opportunities for early intervention.* Journal of Orthopaedic Research, 2011. **29**(6): p. 802-809.

28. Sophia Fox, A.J., A. Bedi, and S.A. Rodeo, *The Basic Science of Articular Cartilage: Structure, Composition, and Function.* Sports Health, 2009. **1**(6): p. 461-468.

29. Jasin, H.E., et al., *Characteristics of anti-type ii collagen antibody binding to articular cartilage.* Arthritis & Rheumatism, 1993. **36**(5): p. 651-659.

30. Cho, H., et al., *Detection of early cartilage damage using targeted nanosomes in a post-traumatic osteoarthritis mouse model.* Nanomedicine: Nanotechnology, Biology and Medicine, 2015. **11**(4): p. 939-946.

31. Shakibaei, M., et al., *Suppression of NF-κB activation by curcumin leads to inhibition of expression of cyclo-oxygenase-2 and matrix metalloproteinase-9 in human articular chondrocytes: Implications for the treatment of osteoarthritis.* Biochemical Pharmacology, 2007. **73**(9): p. 1434-1445.

32. Shakibaei, M., A. Mobasheri, and C. Buhrmann, *Curcumin synergizes with resveratrol to stimulate the MAPK signaling pathway in human articular chondrocytes in vitro.* Genes & nutrition, 2011. **6**(2): p. 171-179.

33. Zhang, Z., et al., *Curcumin slows osteoarthritis progression and relieves osteoarthritis-associated pain symptoms in a post-traumatic osteoarthritis mouse model.* Arthritis research & therapy, 2016. **18**(1): p. 1-12.

34. Clutterbuck, A.L., et al., *Curcumin reduces prostaglandin E2, matrix metalloproteinase-3 and proteoglycan release in the secretome of interleukin 1β-treated articular cartilage.* F1000Research, 2013. **2**.

35. Schulze-Tanzil, G., et al., *Effects of curcumin (diferuloylmethane) on nuclear factor-kB signaling in interleukin-1b-stimulated chondrocytes.* Ann NY Acad Sci, 2004. **1030**: p. 578-86.

36. Dubey, N.K., et al., *Combating osteoarthritis through stem cell therapies by rejuvenating cartilage: a review.* Stem cells international, 2018. **2018**.

37. Rai, V., et al., *Recent strategies in cartilage repair: a systemic review of the scaffold development and tissue engineering.* Journal of Biomedical Materials Research Part A, 2017. **105**(8): p. 2343-2354.

38. Devore, D., et al., *Development and characterization of a rapid polymerizing collagen for soft tissue augmentation.* Journal of Biomedical Materials Research Part A, 2016. **104**(3): p. 758-767.

39. Moody, H.R., et al., *In vitro degradation of articular cartilage: does trypsin treatment produce consistent results?* Journal of anatomy, 2006. **209**(2): p. 259-267.

40. Snider, C., et al., *A novel crosslinker-free technique toward the fabrication of collagen microspheres.* Journal of Biomedical Materials Research Part B: Applied Biomaterials, 2020.

41. Eskelinen, A.S., et al., *Maximum shear strain-based algorithm can predict proteoglycan loss in damaged articular cartilage.* Biomechanics and Modeling in Mechanobiology, 2019. **18**(3): p. 753-778.

42. Lieberthal, J., N. Sambamurthy, and C.R. Scanzello, *Inflammation in joint injury and post-traumatic osteoarthritis.* Osteoarthritis and Cartilage, 2015. **23**(11): p. 1825-1834.

43. Johnson, C.I., D.J. Argyle, and D.N. Clements, *In vitro models for the study of osteoarthritis.* The Veterinary Journal, 2016. **209**: p. 40-49.

Chapter Eight

FABRICATION OF 3D PRINTED SCAFFOLDS USING NOVEL CROSSLINKER-FREE COLLAGEN SOLUTION

8.1 Introduction

Collagen is one of the most abundant protein in the body [1]. This protein provides structural scaffold support for soft tissues such as the dermis, ligaments, and tendons to mechanical protection in articular cartilage [2]. There are 29 different forms of collagen identified [3]. Type I collagen is the most commonly found collagen in the human body at about 80% [4]. It possesses a triple helix structure composed of three polypeptide chains with a glycine-X-Y repeating sequence with X and Y commonly being proline and hydroxyproline respectively.

Type I collagen is a highly biocompatible material with low immunogenicity. It can easily degrade and remodel naturally by the body's cells over time, which positions it as an excellent candidate for therapeutic applications and tissue engineering applications [5]. Collagen can be derived from various sources including animals such as porcine and bovine [6]. Acquiring type I collagen from a source requires a process of solubilizing various tissue elements until a purified collagen structure can thus be solubilized [7, 8].

Solubilized collagen can be formulated into many types of structures. A relatively young technique utilizing solubilized collagen is extrusion-based bioprinting [9]. With this method, collagen can remain in a liquid state, depending

on the solutions pH and temperature. The liquid collagen can be bioprinted into solutions with adjusted pH or increased temperatures, which initiates collagen fibrilization forming a solid structure. Research on bioprinting of type I collagen has been focused on hard tissue applications. A publication by Kim et al. describes the optimization of a type I collagen laden osteoblast-like cell and human adipose-derived stem cell bioink [10]. In this work they compared a collagen-based bioink to an alginate bioink. The collagen-based bioink improved cellular activity and also improved relative concentrations of osteogenic biomarkers like BMP-2, Runx2, type I collagen, and OCN at 28 days with human adipose-derived stem cells [10]. Another interesting study by Filardo et al. printed an MRI scanned human meniscus tissue using extrusion-based 3D printing with a type I collagen and bone-marrow-derived mesenchymal stem cells [11]. Using additive manufacturing methods like extrusion-based bioprinting of collagen creates unique fabrication capabilities for patient-specific treatments.

Chemical crosslinking is a common technique used to conjugate additional agents, such as gold nanoparticles (AuNPs) to collagen tissue scaffolds [12]. Common crosslinkers include genipin and 1-Ethyl-3-[3-dimethylaminopropyl]carbodiimide hydrochloride)/N- hydroxysuccinimide (EDC/NHS) crosslinking. EDC/NHS crosslinking involves the formation of a peptide bond between carboxyl and amino groups. EDC/NHS crosslinking is a zero-length crosslinker, meaning the actual EDC molecule is not a part of the final crosslinked product. But the EDC/NHS crosslinking reaction creates unwanted urea byproducts that can cause cytotoxicity if not removed. This then

requires laborious washing techniques which can cost time and may damage the tissue/collagen scaffolds. EDC/NHS crosslinking has also been shown to affect native-like cellular adhesion [13]. An alternative crosslinker is genipin. Genipin is a natural crosslinker isolated from gardenia jasminoides fruits. Genipin can spontaneously react with two amino groups that form monomer to tetramer crosslinks [14]. The use of genipin has also been studied as an anti-inflammatory agent [15, 16]. With this in mind, genipin is generally advantageous because it does not necessitate extensive washing steps to remove extraneous unwanted byproducts after the crosslinking process. In fact, the lack of washing could improve the overall healing time with the observed anti-inflammatory properties of genipin.

Gold nanoparticles (AuNPs) have had much interest in tissue engineering applications in recent years. This may be due to AuNPs multiple studied benefits such as mitigation of inflammation, promotion of cellular migration, and high biocompatibility [12, 17, 18]. Attachment of AuNPs to scaffolds may increase the surface energy of the scaffold which can in turn increase cellular adherence through adsorption of proteins [19]. AuNPs have also been documented to be an effective antimicrobial agent along with being an effective free radical scavenger which inhibits the formation of reactive oxygen species (ROS) [20, 21]. The production of ROS is known to be detrimental to tissues during wound healing. By utilizing AuNPs on musculoskeletal tissue scaffolds, this may allow for quicker healing time through increased cellular migration, remodeling and reduction of surrounding ROS.

This work describes the method of fabrication of porcine type I collagen scaffolds for general musculoskeletal tissue applications via additive manufacturing, 3D printing, with two different bioprinters. Further characterization of the 3D printed collagen scaffolds includes the use of two different chemical crosslinkers, EDC/NHS and genipin. An analysis of thermal stability, ability to conjugate AuNPs, and cellular interactions on the composite 3D printed collagen scaffolds was performed.

8.2 Materials and methods

8.2.1 Bioprinter

One of the bioprinters used to fabricate the 3D scaffolds was a custom bioprinter assembled from a CNC milling machine as shown in Figure 8.1. Three stepper motors were used to individually control each axis; X, Y, and Z. The motors had an error of movement less than 0.1 μm. The print bed was created by placing the X stage and Y stage on top of one another. The Z stage was placed in a perpendicular orientation to the print bed. To control the motor's movements, G-code was written and executed using Mach3 Mill software. A syringe pump was mounted on the Z stage which held and extruded the printing solution (liquid collagen). Figure 8.2 are images of scaffolds printed from the custom CNC milling machine. Figures 2A & 2B are images of a 20 mm X 6.3 mm cylinder. Studies performed in this work were 4 mm X 2.4 mm scaffolds printed in Figure 8.2C.

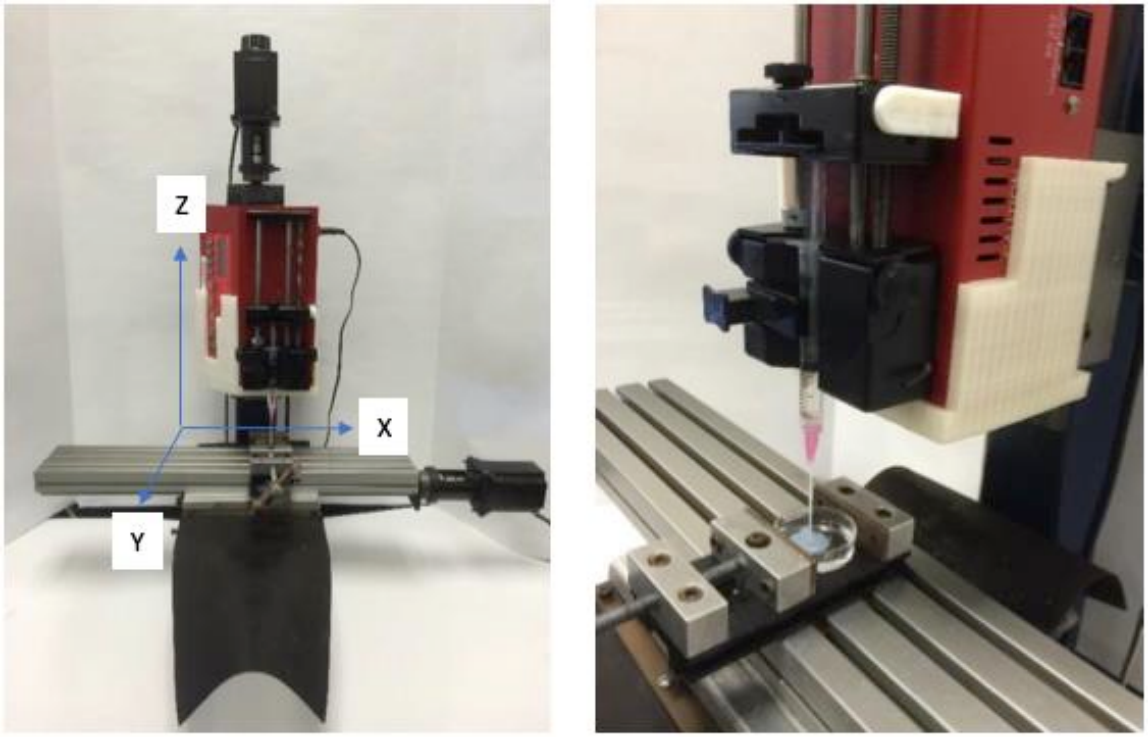

Figure 8.1. Custom 3D printer from CNC milling machine. (A) X, Y, and Z axes denoted on the printer (b) shows the 3D printer printing a collagen scaffold.

Figure 8.2. Collagen scaffolds printed from the custom 3D printer (A) top view of a 20 mm X 6.3 mm 3D printed collagen cylinder scaffold (B) side view of a 20 mm X 6.3 mm 3D printed collagen cylinder scaffold (C) 4 mm X 2.4 mm 3D printed cylinder scaffolds used for experimentation.

A Cellink Bio X (Boston, MA) 3D bioprinter using a temperature-controlled pneumatic printhead (4-65°C) was also used to print, as shown in Figure 8.3. A 3

ml Cellink pneumatic printing cartridge was filled with our printing solution (liquid collagen) and a 27-gauge conical nozzle was utilized during printing. The temperature-controlled pneumatic printhead was set to 4°C. The printing solution was printed into a 150 mm diameter polystyrene Petri dish filled with 15 ml of 24°C ddH_2O. The print height was set to 0.2 mm with a printing speed of 3 mm/s and nozzle pressure was set to 10 kPa for all prints. Post printing, scaffolds were allowed to fibrillize for 5 minutes and then lifted out of the Petri dish and placed in 70% ethanol for storage. 3D models were designed using Solidworks and sliced with Cellink's built-in slicing software or Slic3r software. Figure 8.4 is a computer-generated diagram of the printed scaffold layer by layer. For cell studies, a 6 mm X 0.8 mm (4 layers) cylinder scaffold with a 20% rectilinear infill pattern was designed as shown in Figure 8.5A. Figure 8.5B is a scaffold printed in an agarose microparticle solution.

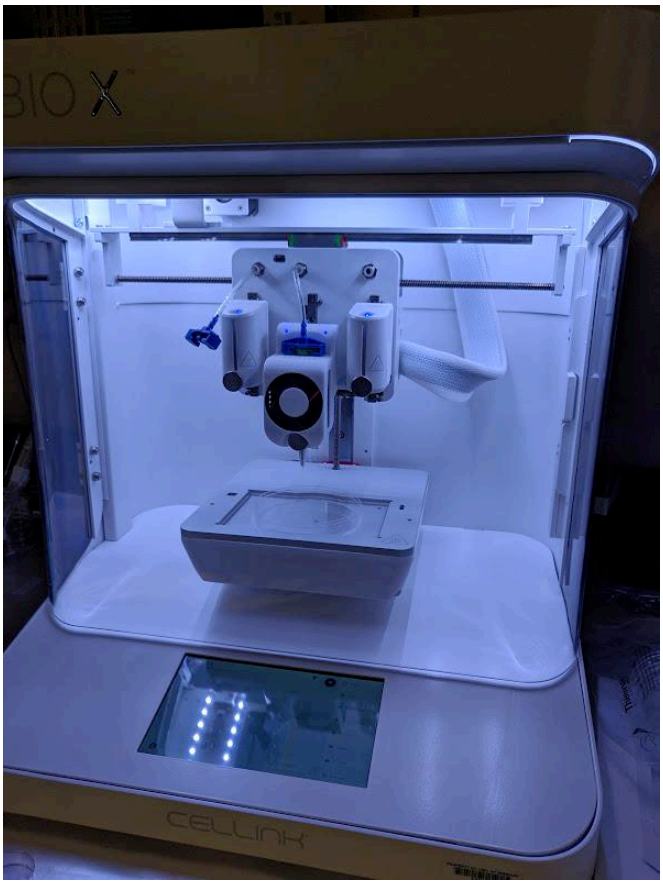

Figure 8.3. Cellink BioX printer with temperature controlled printed head.

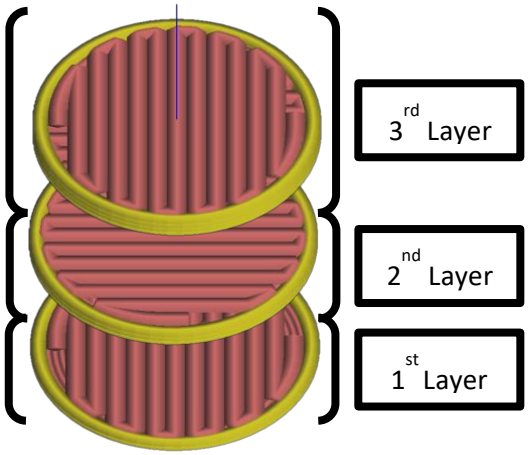

Figure 8.4. Slic3r computer generated sliced diagram of a 6 mm X 0.8 mm scaffold

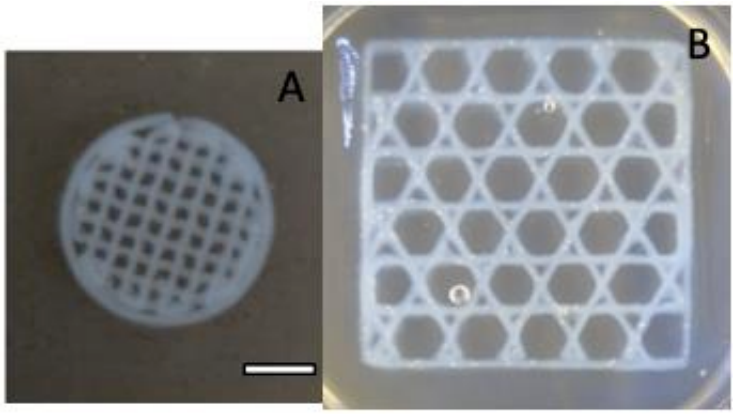

Figure 8.5. 3D printed collagen scaffolds using the Cellink BioX printer (A) 6 mm X 0.8 mm cylinder scaffold printed in water (B) 20 mm X 20 mm X 1 mm rectangular scaffold printed in an agarose microparticle solution.

8.2.2 Fabrication of liquid collagen

Porcine collagen type I (6 mg/ml, Sunmax Biotechnology, Taiwan) was precipitated using 1.04 M sodium chloride (NaCl, ≥99.0%, Sigma Aldrich, MO). The precipitated collagen solution was then centrifuged at 3,500 rpm for 15 minutes. A white collagen pellet was formed at the bottom of the tube and the supernatant was poured off leaving a 150 mg collagen pellet. Fifteen ml of 0.5 M glacial acetic acid (≥99.7%, Fisher Chemical, KS) was added to the collagen pellet and allowed to sit overnight at room temperature to let the collagen pellet solubilize. The collagen/acetic acid solution was then placed in a 15 ml, 10 kDa molecular weight cutoff dialysis cassette (Thermo Scientific, IL) and immersed in ethylenediaminetetraacetic acid (35mM, EDTA, Fisher Chemical, KS)/ H_2O solution with a pH of 7.5 using sodium hydroxide (10 N, NaOH, Ricca Chemical Co., TX) [22]. The pH of the EDTA solution was checked and maintained at 7.5 daily until the pH no longer fluctuated from 7.5. The liquid collagen (LC) solution was then removed and pH was tested to ensure it was set at 7.5.

8.2.3 Agarose Microparticle Printing Solution

The agarose microparticle printing solution was developed by Senior et al. [23]. To prepare the solution, a 0.5% (w/v) agarose solution was heated in an autoclave for 30 minutes at 225°F. After autoclaving, the heated solution was placed on a stir plate at 700 rpm until the solution reached room temperature.

8.2.4 EDC/NHS Crosslinking

To crosslink the 3D printed scaffolds using EDC/N-hydroxysulfosuccinimide (NHS) crosslinking, printed scaffolds were placed in a flask at room temperature in a solution of 2 mM EDC (dissolved in 0.1 M 2-(N-morpholino)ethanesulfonic acid (MES) in 0.5 M sodium chloride (NaCl)) and 5 mM sulfo-NHS (first dissolved in dimethylformamide (DMF)) 50% acetone and phosphate-buffered saline (PBS; 7.5 pH). The flasks were placed on an orbital shaker at 75 rpm for 12 hours. Samples were subsequently washed three times with PBS.

8.2.5 Genipin Crosslinking

To crosslink the genipin crosslinked scaffolds, 2 mM genipin (initially dissolved in 18% (w/v) dimethylsulfoxide (DMSO)) solution was prepared using PBS. Samples were placed in a flask on an orbital shaker at 75 rpm and were incubated in the genipin solution for 12 hours. Samples were subsequently washed three times with PBS.

8.2.6 Conjugation of AuNPs

Twenty nm AuNPs were acquired from Ted Pella Inc. (Redding, CA). To conjugate AuNPs, AuNPs were functionalized using a 15 μM 2-mercaptoethylamine (MEA) solution and added to the printed scaffolds at the same time as the addition of EDC/NHS crosslinking solution or genipin crosslinking solution [24]. A 1x concentration of AuNPs correlates to $7.0x10^{11}$ AuNP/ml AuNPs and 2x concentrations correlates to a $14.0x10^{11}$ AuNP/ml

concentration of AuNPs. A 1x AuNP concentration was used unless otherwise stated.

8.2.7 Sterilization

Samples undergoing biological study were sterilized using an ethanol solution. Samples were placed in a 70% ethanol solution for 24 hours at room temperature. After 24 hours, samples were then placed in sterile cell media for 24 hours. Finally, samples were transferred to a sterile 48-well culture and immersed in fresh sterile cell media in preparation for biological culture.

8.2.8 Differential Scanning Calorimetry

A Q2000 Differential scanning calorimeter (DSC) (TA Instruments, New Castle, DE) was used to observe the denaturation temperatures of the 3D printed scaffolds. The 4mm X 2.4 mm cylinders, Figure 8.2C, were printed, dissected and then placed in the bottom of aluminum sample pans (~5 mm in diameter). These pans were then hermetically sealed. The DSC heated from -5°C to 120°C with a temperature ramp rate of 3°C/min with modulation every 80 s ± 0.64°C. The denaturation temperatures were determined using Universal Analysis software.

8.2.9 Scanning Electron Microscopy

Scanning electron microscopy (SEM) was used to determine AuNP conjugation to 3D printed scaffolds. Images were acquired using a Quanta 600

FEG (FEI, Hillsboro, OR). Samples were in low vacuum. Magnification ranged from 75X to 20,000X and the electron beam was set to 10 kV.

8.2.10 Neutron Activation Analysis

Neutron activation analysis was utilized to quantify the gold nanoparticles bound to the scaffolds. NAA was conducted at the University of Missouri Research Reactor Center. Once printed, the collagen samples were lyophilized, weighed, and secured within high-density polyethylene vials where they remained during the analysis. Samples were irradiated for two minutes, then allowed to decay for one to seven hours. Gamma radiation was measured for ten minutes via a Canberra High Purity Germanium detector. The detector has a relative efficiency of 33.7% and a full width half maximum resolution of 1.73 keV at 1.33 MeV. A Canberra digital signal processor, Model 9660A, was used in tandem with the detector and a high voltage power supply. Analysis of the data was performed utilizing Canberra-VMS Genie 2000 software, and the quantities of gold were recorded in Microsoft Excel.

8.2.11 Cell Culture

All cell assays were conducted with L929 murine fibroblast cells acquired from ATCC Manassas, VA. Cells were cultured at 37ºC and 5% CO_2. Cell media used for culture was Eagle's Minimum Essential Medium (EMEM) supplemented with 200 U/ml Penicillin streptomycin and 10% horse serum. Cell passage

numbers in the assays were between two and twenty-eight times. Cells remained under sterile conditions using a biological safety cabinet.

Cell studies involving stromal cells were human, patient derived. Fitzgerald et al. described the protocol for isolation [25]. A very similar protocol to remove and isolate the endometrial epithelial cells was used to isolate the stromal cells. Further processing to isolate the stromal cells included using a 10 μm filter strainer to isolate the stromal cells after 100 μm and 40 μm filters. The filtrate was pelleted by centrifugation at 232 RCF for 10 minutes and the stromal cell pellet resuspended in 5 ml DMEM/F12 (Gibco, #11320-033) supplemented with 1% antibiotic-antimycotic (Gibco, #15240-062) and 10% charcoal stripped fetal bovine serum (CSFBS) and then transferred to a T25 flask. To obtain a pure population of stromal cells, the cells were incubated for 15 minutes at 37°C, supernatant collected and then transferred to a second T25 flask. The stromal cells were then continuously cultured until needed for further experiments. The stromal cells were seeded onto the 3D printed scaffolds in 50 μl of $3x10^4$ cells. Cells were allowed to adhere for 30 minutes and the then 700 μl of culture medium was added. Culture media was exchanged as needed.

8.2.12 Cell Viability Study

Cell viability reagent WST-1 (Sigma Aldrich, MO) was used to assess the biocompatibility of the 3D printed scaffolds with L929 murine fibroblast cells. The 3D printed scaffolds were incubated in fresh supplemented EMEM 24 hours prior to the addition of fibroblast cells in a 48-well plate. Cells were seeded onto

scaffolds at a ratio of $3x10^4$ cells per well. A 250 µl of the supplemented media was replaced every 3 days during study. A 50 µl of the WST-1 reagent was added to each well and allowed to incubate for 4 hours. After 4 hours, 125 µl from each well was plated into a new 48-well plate and absorbance reading were measured at 450 nm with a 600 nm filter using a spectrofluorometer.

8.3 Results

8.3.1 Printing Images

Figure 8.2 provides images of 3D printed collagen scaffolds using the LC solution on the custom CNC bioprinting machine. As shown in Figure 8.2A & 2B, a general 20 mm X 6.3 mm cylinder was printed in order to determine if the LC was applicable for 3D printing. The images demonstrated that the LC is amendable to printing; we are the first to report 3D printing of this EDTA stabilized collagen. The 3D printed scaffolds observed in Figure 8.2C was used in our characterization studies. Samples produced using the Cellink BioX printer can be seen in Figure 8.5. The 3D printed scaffold in Figure 8.5A was used in our cellular characterization studies. The 3D printed scaffold in Figure 8.5B was printed using the support agarose solution which provides solid-like behavior under low shear but liquid-like behavior with applied stress [23]. The support solution is also able to recover from the deformation quickly once the shear stress is removed. This allowed the collagen to be held in into position and supported by the agarose solution after being printed creating less printing defects and created a more reproducible scaffold.

8.3.2 LC printing Diameter

Using a 27-gauge conical bioprinting nozzle tip from Cellink, a profile of LC's print diameter was determined by holding the printing rate a 3mm/s. The results are shown in Figure 8.6. Noticeably, an increase in printed diameter was observed with increased extrusion pressure ranging from 7 kPa to 13 kPa. Printed diameters ranged from 400 µm to 802 µm. A significant increase in printed diameter was observed from 12 kPa to 13 kPa with demonstrated approximately 224 µm increase in diameter. Printing below 6 kPa was not possible due to the difficulty of extruding collagen under low pressures while printing above 13 kPa resulted in non-uniform collagen diameters.

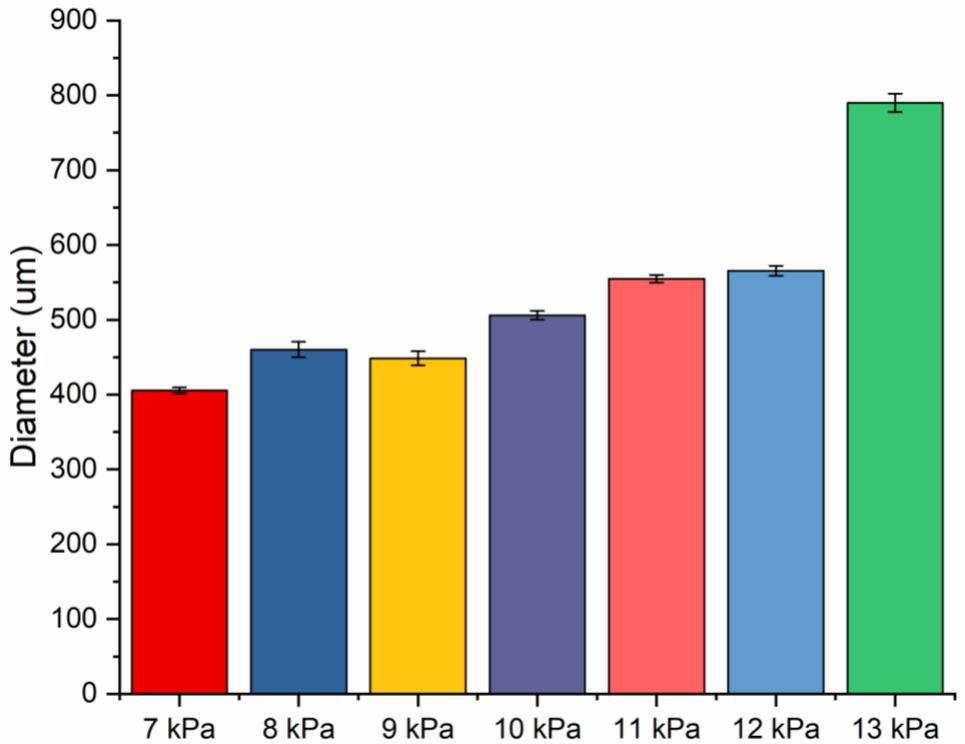

Figure 8.6. 3D printed collagen fiber diameter of various extrusion pressures from Cellink BioX printer using a 27-gauge nozzle at 3 mm/s.

8.3.3 Thermal stability

Thermal stability of 3D printed scaffolds crosslinked with either EDC/NHS or genipin were analyzed using DSC analysis. In our preliminary experiments with EDC/NHS crosslinking, two methods of crosslinking were tested. In one method, the samples were printed directly into the crosslinking solution. In the second method, the samples were printed into water, and stayed in water for 24 hours and then placed in the crosslinking solution. The denaturation results are shown in Figure 8.7A. These results demonstrated that both methods increased the overall denaturation temperature relative to the uncrosslinked sample. Interestingly, the two crosslinking techniques demonstrated significantly different results. Crosslinking in 2 mM, 5 mM, and 10 mM, the samples that were printed in water first and then crosslinked had a much higher denaturation temperature compared to the samples that were printed directly into the crosslinking solution. Alternatively, the group that was printed directly into the 20 mM solution higher denaturation temperature in comparison to printing in water then crosslinking. Overall, the 10 mM EDC crosslinking group that was printed into water then crosslinked had the highest thermal stability at 71°C. The 2 mM EDC/NHS was used in future studies utilizing EDC/NHS crosslinking unless otherwise stated. The reasoning for using 2mM EDC/NHS was to achieve structural stability of the collagen scaffold without the rigidity. If the scaffold is too stiff, then the collagen's ability to achieve enhanced cellularity might be reduced. The 2mM solution provided an increase denaturation temperature which provided us a more thermally stable scaffold.

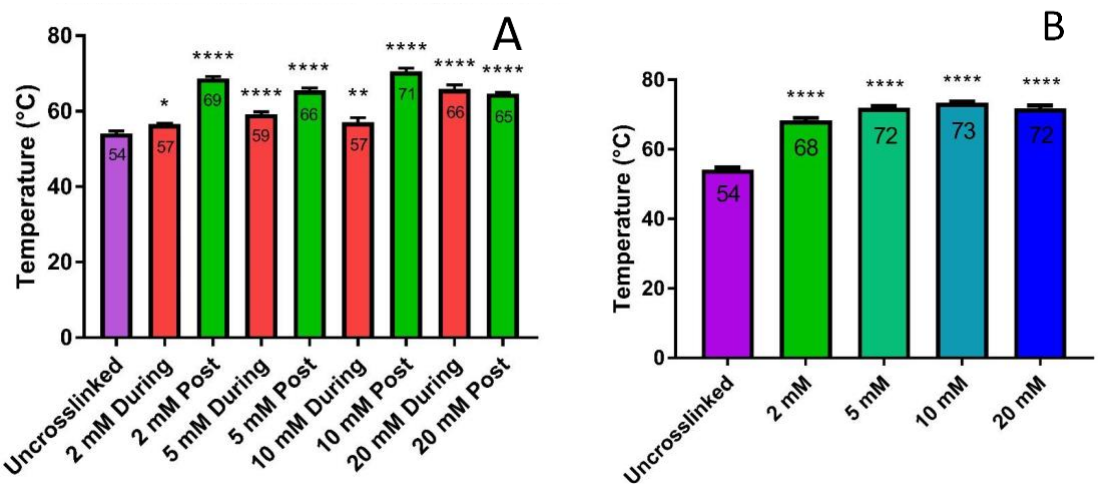

Figure 8.7. DSC denaturation results from (A) crosslinking using EDC/NHS during printing or after printing (B) crosslinking using genipin.

Samples crosslinked with genipin were all printed into water and then placed in a genipin crosslinking solution. All samples crosslinked with genipin were significantly more stable than uncrosslinked samples as shown in Figure 8.7B. An increase in denaturation temperature can be observed by increasing the genipin crosslinking solution from 2 mM to 10 mM. The increased denaturation temperature from 2 mM to 5 mM was the most significant with an overall decrease in denaturation temperature observed from 10 mM to 20 mM. With 2 mM genipin providing a significant increase in thermal stability and due to the cost of genipin, 2 mM genipin was used in all future studies unless otherwise stated.

8.3.4 SEM Analysis

Both EDC/NHS and genipin crosslinking was used to conjugate AuNPs to the 3D printed collagen scaffolds and were analyzed using SEM microscopy to validate the presence of AuNPs as shown in Figures 8.8 and 8.9 respectively. Both crosslinking techniques had AuNPs conjugated to the surface of the printed collagen fibers. Upon visual inspection, the samples conjugated with EDC/NHS appeared to have more clumped AuNPs on the surface of the scaffolds relative to the samples conjugated with genipin.

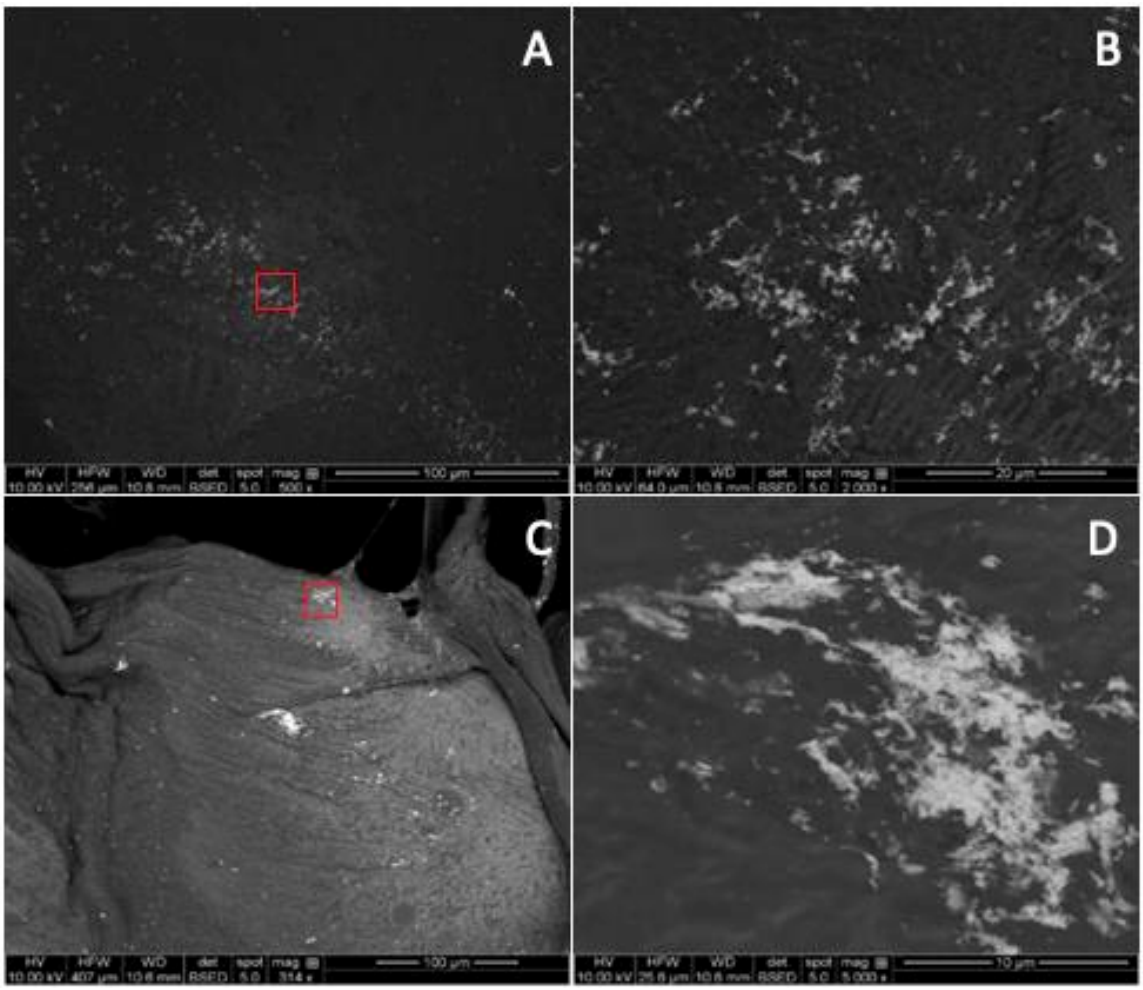

Figure 8.8. SEM backscattered micrographs of EDC/NHS conjugated AuNPs on 3D printed scaffolds (A) 500X magnification; (B) 2,000X magnification from red box in (A); 314X magnification (D) 5,000X magnification from red box in (C).

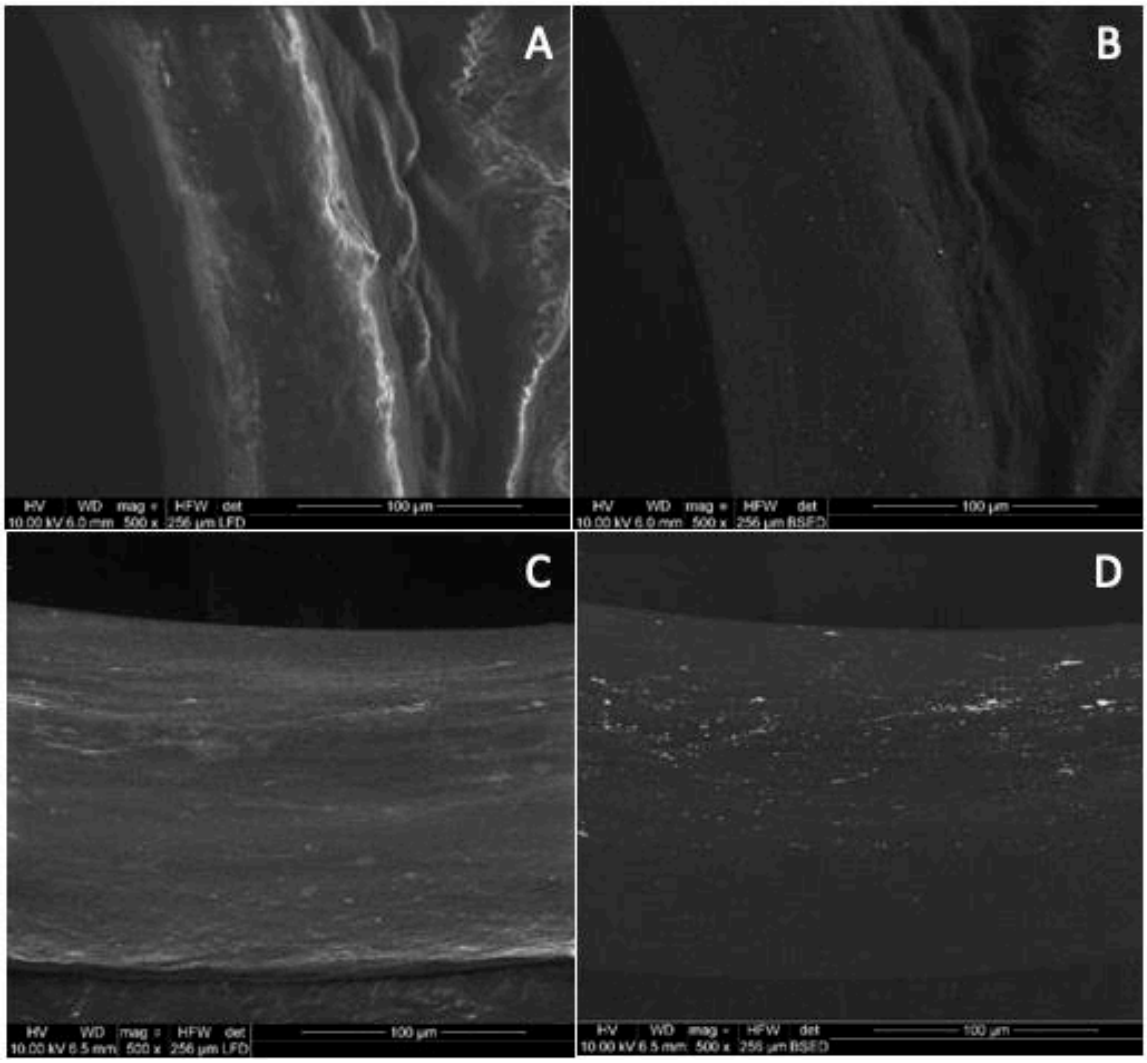

Figure 8.9. SEM micrographs of genipin conjugated AuNPs on 3D printed scaffolds (A) secondary electron micrograph, 1x AuNP concentration; (B) backscattered electron micrograph, 1x AuNP concentration; (C) secondary electron micrograph, 2x AuNP concentration; (D) backscattered electron micrograph , 2x AuNP concentration

8.3.5 NAA Analysis

NAA analysis was used to provide a quantitative measurement of relative AuNPs conjugated to the 3D printed scaffolds. The results are shown in Figure 8.10. A 1x and 2x concentrations of AuNPs were conjugated with both EDC/NHS and genipin. On average genipin, in both cases of 1x and 2x AuNP concentrations, correlated to increased conjugation compared to EDC/NHS

conjugation in terms of mass percent. Comparing the increase from 1x to 2x AuNP using EDC/NHS, this correlated to an approximately 100% increase in AuNP mass percent as shown in Figure 8.10A. When examining the use of genipin comparing 1x and 2x AuNP mass percent, approximately a 78% increase in AuNP attachment was observed as shown in Figure 8.10B.

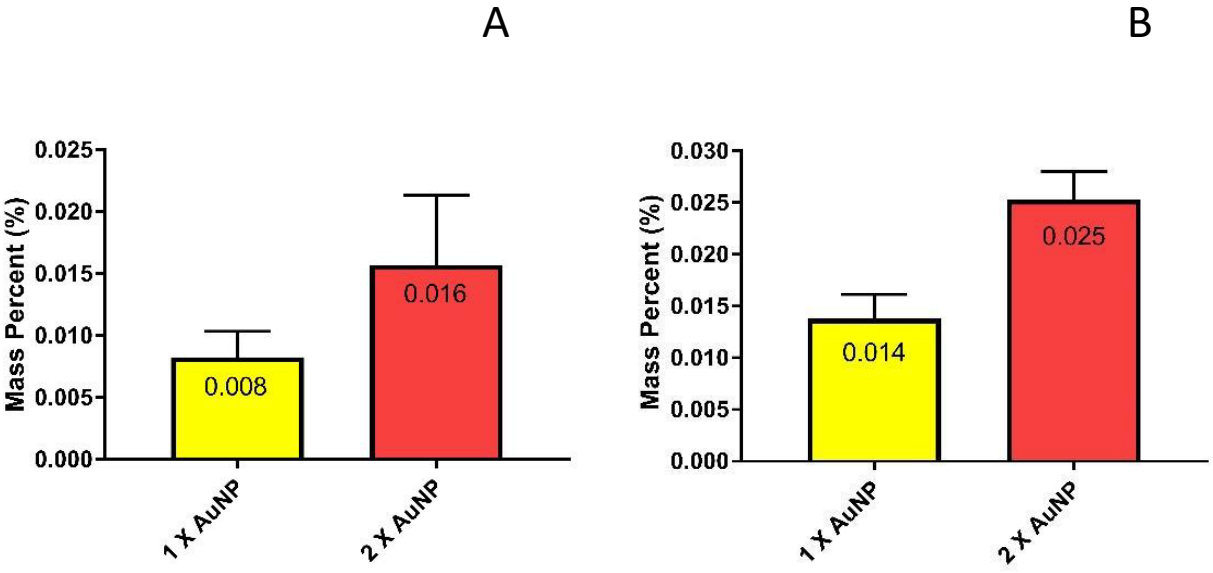

Figure 8.10. NAA results from crosslinking AuNPs to 3D printed scaffolds with (A) EDC/NHS (B) genipin

8.3.6 3D Printing into A Cell Suspension

Printing of a 3D collagen scaffold into an L929 fibroblast cell solution was investigated using light microscopy. Figure 8.11 provides images of a 3D printed scaffold printed into 4 ml of $4.0x10^5$ cells/ml L929 fibroblast solution. The goal of this study was to determine if printing into a cell solution with a 10-minute incubation would provide enough time for the cells to adhere to the 3D scaffold. Figure 8.11A is an image immediately after the printing of the scaffold. The outline of the collagen fibers can be observed due to the cells covering and

adhering to the fibers. After a 10-minute incubation of the cells at 37°C, the 3D scaffold was washed 5 times using cell media and imaged again as shown in Figure 8.11B. After washing the scaffold, a significant number of cells still remained on the 3D printed scaffold.

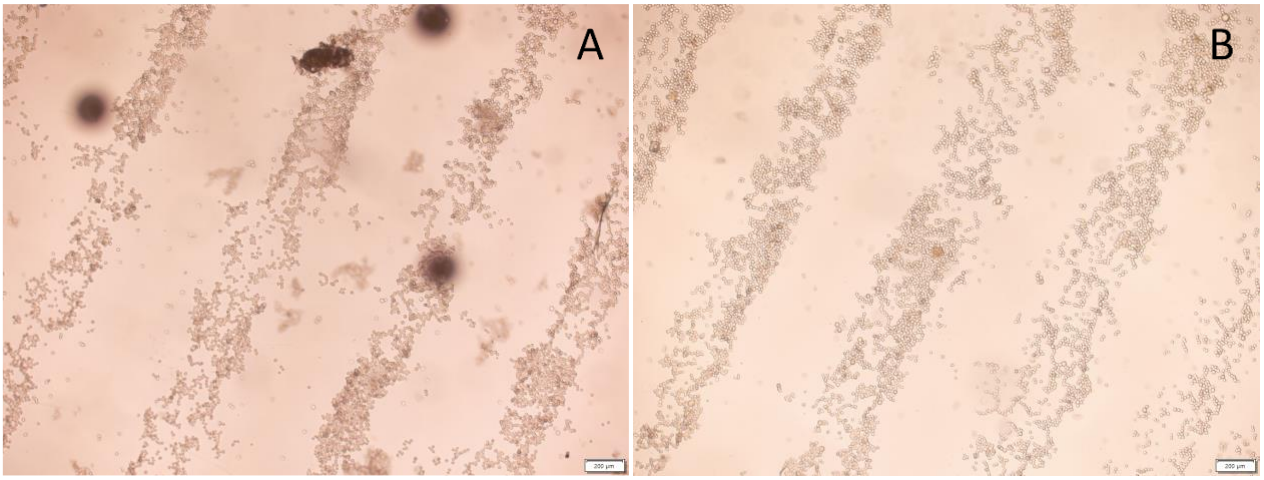

Figure 8.11. Printing collagen scaffold into L929 cell solution (A) 4x light microscope image of cells on collagen fibrils immediately after printing without washing (B) 4x light microscope image of cell on collagen fibrils after 10 minutes of incubation and 5 washes.

8.3.7 Cell Viability Analysis

A 3-day cell viability analysis was conducted using both EDC/NHS and genipin crosslinkers with AuNPs. Results are shown in Figure 8.12. Scaffolds crosslinked with genipin were studied in Figure 8.12A. All groups with 3D printed collagen scaffolds had enhanced cellular viability compared to cells with no scaffold as shown in Figure 8.12A. A reduction in viability can be observed with the genipin scaffolds and also the genipin scaffolds conjugated with AuNPs. Using EDC/NHS crosslinking, similar cellular viability can be observed between groups with 3D printed collagen scaffolds and cells with no scaffolds as shown in Figure 8.12B. EDC/NHS crosslinking along with the addition of AuNPs decreased the cellular viability relative to cells with no scaffold.

A 7-day cell viability analysis was also conducted looking at the use of crosslinker genipin and 1x and 2x AuNP concentrations, Figure 8.12C. Cells with no scaffold had increased viability relative to cells with 3D printed collagen scaffolds. The addition of genipin to the scaffolds increased the viability relative to the uncrosslinked scaffolds. The conjugation of 1x and 2x AuNP further enhanced viability relative to genipin alone with 2x AuNP providing the highest

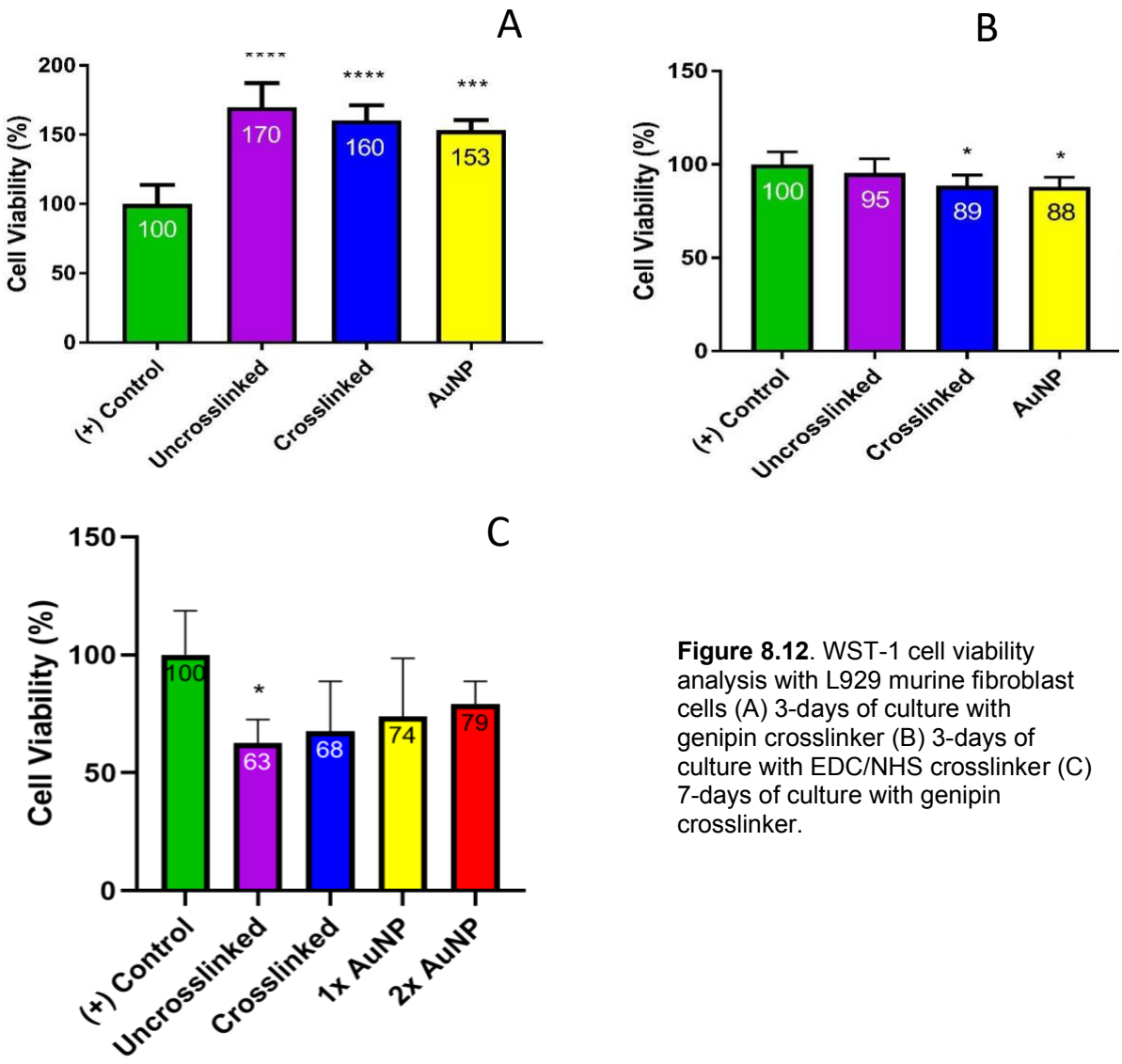

Figure 8.12. WST-1 cell viability analysis with L929 murine fibroblast cells (A) 3-days of culture with genipin crosslinker (B) 3-days of culture with EDC/NHS crosslinker (C) 7-days of culture with genipin crosslinker.

overall viability relative to all groups with 3D printed scaffolds.

8.3.8 ROS Analysis

An OxiSelect ROS assay was used to determine the ability of the 3D printed scaffolds to mitigate intracellular ROS production by the cells after the introduction of the 3D printed collagen scaffolds in Figure 8.13. The uncrosslinked 3D printed scaffolds produced similar amounts of ROS relative to the cells with no scaffold added. Crosslinking with genipin and the addition of AuNPs appeared to increase ROS production with the addition of AuNP significantly increasing ROS production.

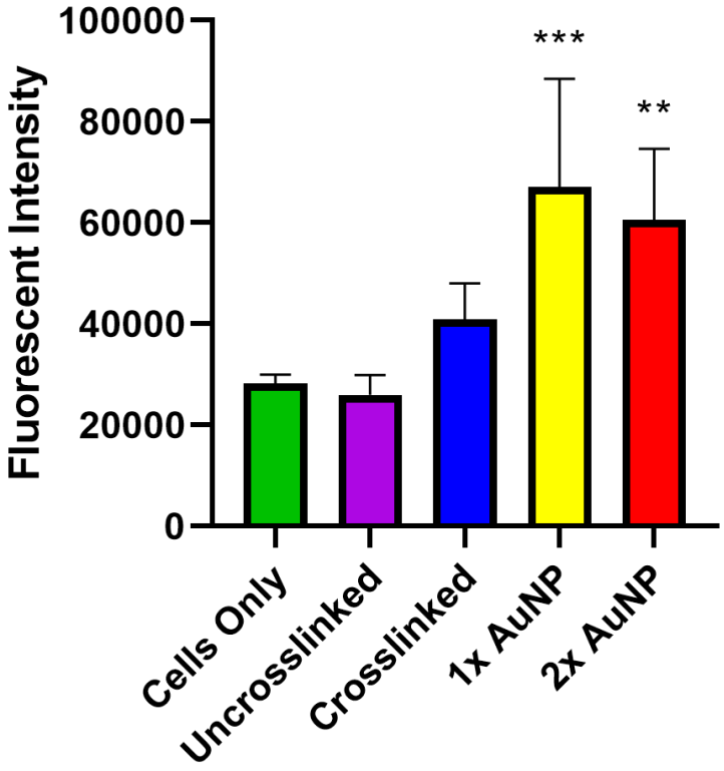

Figure 8.13. 24-hour OxiSelect ROS assay quantifying produced intracellular ROS by L929 murine fibroblast cells

8.3.9 Printing in Agarose Solution

Printing into an agarose microparticle solution was attempted as shown earlier in Figure 8.5B and cultured with cells. Printing into the agarose microparticle solution was advantageous due to the almost 100% reproducibility of each scaffold. However, problems arose when printing into the agarose microparticle solution when culturing cells on the 3D printed scaffolds. The first complication was washing the scaffolds after printing. The agarose needed to be removed from the scaffold post-printing. After washing, remnant agarose microparticles were apparent on the 3D printed scaffold as shown in Figure 14. Secondly, cells seeded onto the scaffold did not appear to have much if any attachment on the scaffold, preferring the bottom of the well plate instead.

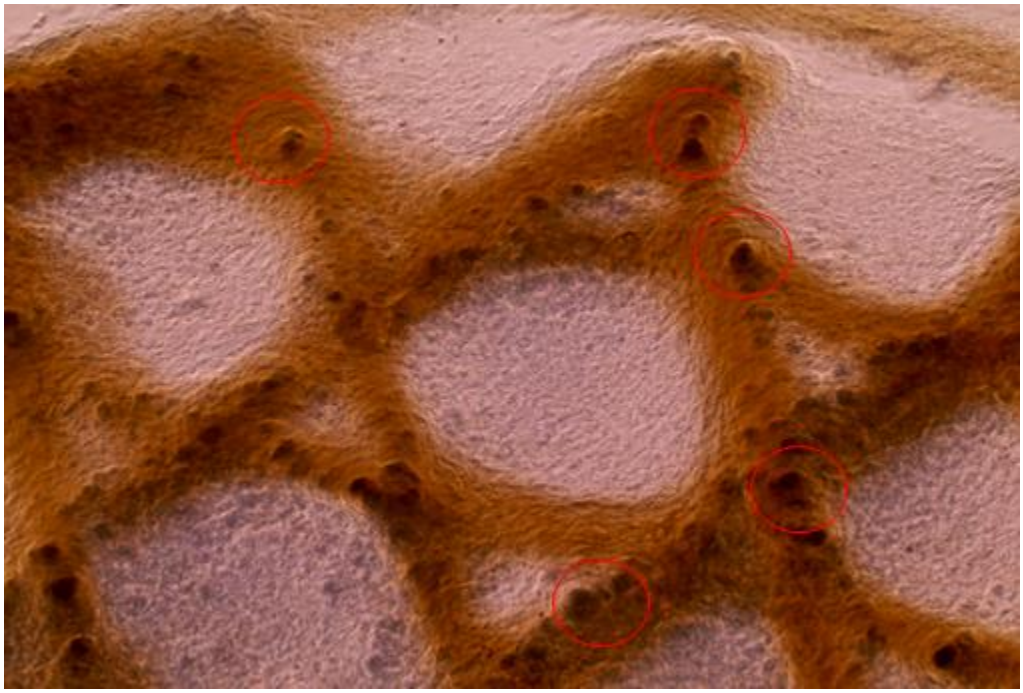

Figure 8.14. A 4x light microscope image of a 3D printed collagen scaffold printed into agarose microparticle solution. The scaffold was washed prior to imaging. Red circles highlight some of the remnant agarose particles on the scaffold.

8.3.10 Stromal cell degradation of 3D printed scaffolds

Stromal cells were seeded onto a 10 mm X 0.6 mm 3D printed collagen scaffold. Figure 8.15 provides images of the scaffold at 9 days of incubation without cells, Figure 8.15A, and with the stromal cells, Figure 8.15B. The cells appeared to significantly degrade the 3D printed scaffold at 9 days relative to the sample with no cells. The cells also began to seed along the bottom of the well plate.

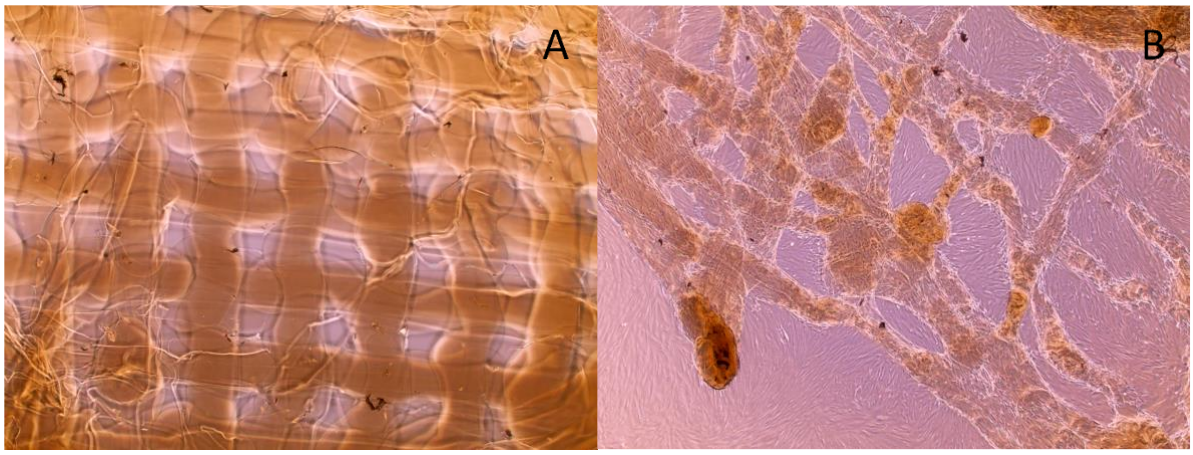

Figure 8.15. 4x Light microscope images of 9-day cultured 3D printed collagen scaffolds with no crosslinker (A) with no cells (B) with stromal cells.

This study was repeated with stromal cells. This time three separate groups were studied, genipin only, laminin only, and genipin + laminin. Figure 8.17. Genipin was used to crosslink the collagen fibers to create a more stable structure as previously observed from the DSC results. Laminin, a basement membrane protein, was also added to the scaffolds in an attempt to improve cellular adherence to the 3D printed scaffolds. The third group is a genipin + laminin. Figure 8.16 provides a flow chart on how these scaffolds were prepared

for culture. The results of the scaffolds seeded with stromal cells can be observed in Figure 8.17. Images were acquired at 4 days and 16 days of culture. On day 4 of culture, the scaffold with only laminin began shrinking, and visually the pores of the scaffold were lost as noted in Figure 8.17A. Both samples crosslinked with genipin remained structurally sound and their shape was retained as shown in Figure 8.17D & 17G. Cells can be observed on the surface of both genipin crosslinked scaffolds at 4 days. At 16 days, the laminin-only sample had completely lost its structural integrity and formed a globular shape as noted in Figure 8.17B & 17C. The two genipin crosslinked samples remained structurally intact at 16 days as shown in Figure 8.17E & 17H. Again, both genipin crosslinked samples retained a homogenous cellular network across their scaffolds. Figure 8.17C, 17F & 17I are photographs of the scaffolds at 16 days. The scaffolds' porous network is still visible by the naked eye with samples crosslinked with genipin while the uncrosslinked, laminin sample demonstrated visible reduction in size and lost of integrity.

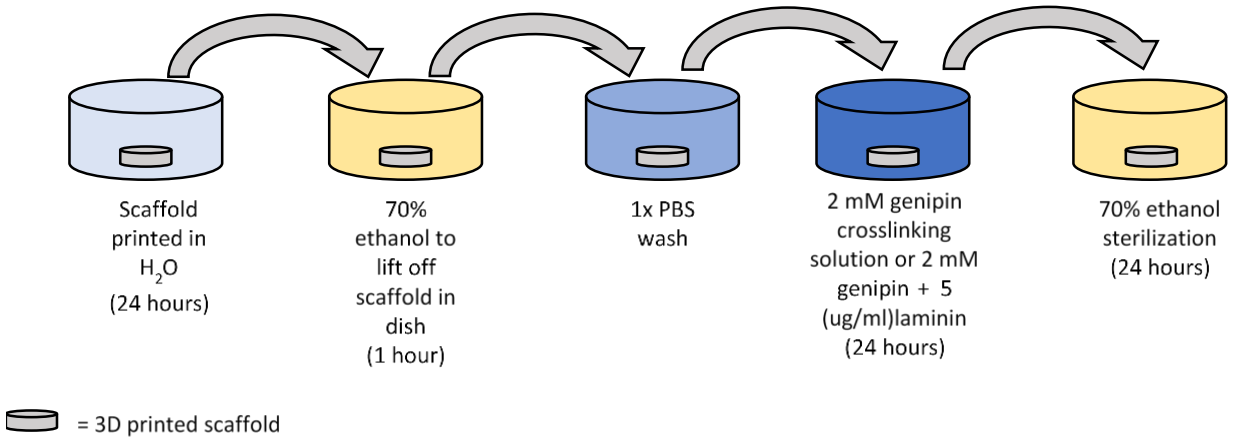

Figure 8.16. Diagram of how 3D printed collagen scaffolds were prepared for culture with stromal cells

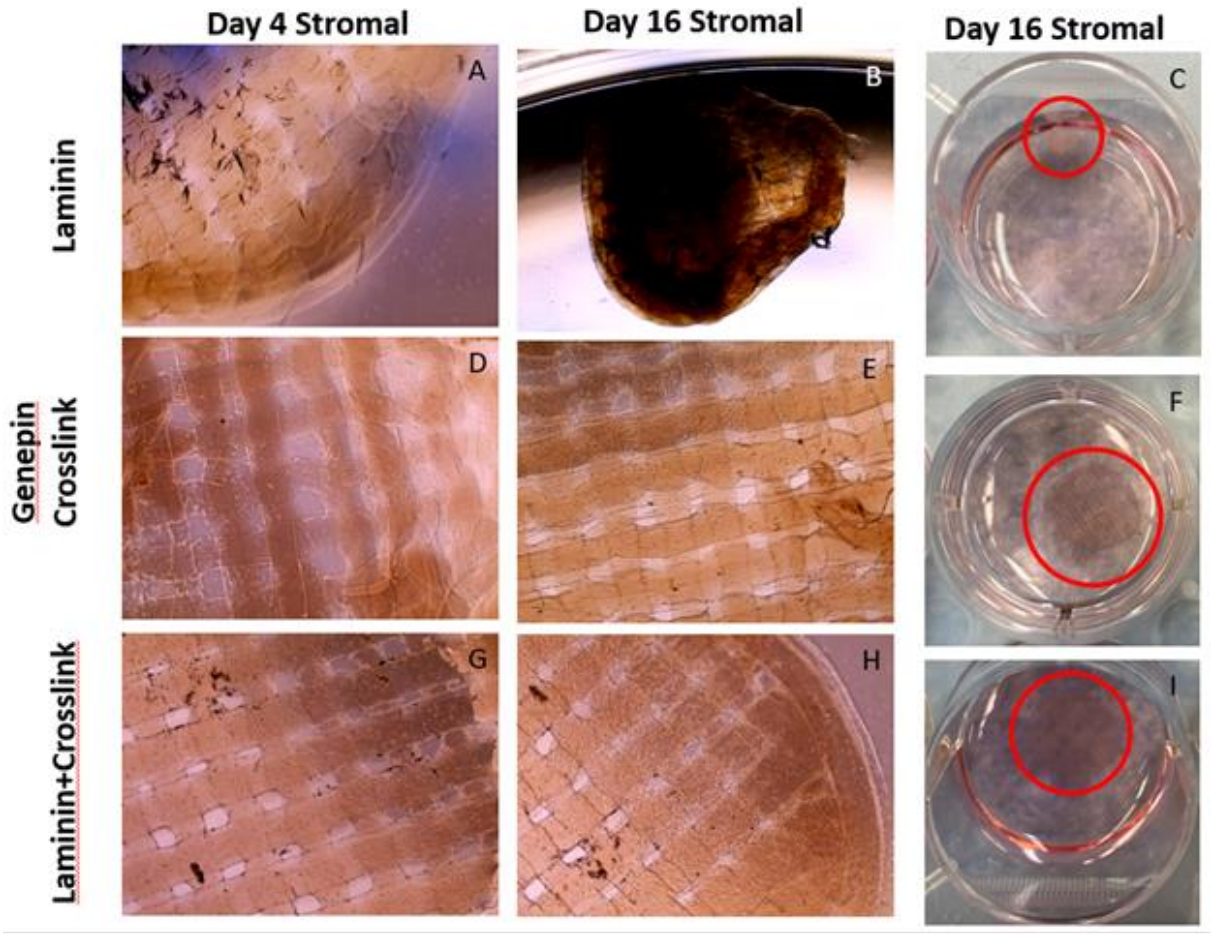

Figure 8.17. Images of stromal cells seeded onto 3D printed collagen scaffolds supplemented with (A,B,C) laminin; (D,E,F) genipin crosslinked; (G,H,I) genipin crosslinked and laminin. (A,D,G) are 4x light microscope images at 4 days of incubation; (B,E,H) 4x light microscope images at 16 days of incubation; (C,F,I) photographs at 16 days of incubation.

8.4 Discussion

In this work we describe the use of an LC solution that can be extruded from two different additive manufacturing 3D printers. The first printer being a custom-built printer utilizing CNC milling motors along with a mounted syringe pump to create a 3D structure and second, a commercial Cellink BioX bioprinter.

Investigation of extrusion pressure was performed using the Cellink BioX bioprinter which provided a profile of extruded collagen fiber diameters.

Thermal stability analysis was also performed on various molar concentrations of the crosslinkers EDC/NHS and genipin. It was determined that printing the 3D scaffolds first in water and then crosslinking the scaffolds after printing created a more thermally stable structure. It is theorized that this two-step process created a more stable structure because the collagen fibrils are allowed to self-assemble naturally prior to chemical crosslinking. Printing directly into a crosslinking solution may cause immediate crosslinking of carboxyl to amino groups and thereby disrupting the natural fibrilization of the liquid collagen, leading to a less thermally stable structure. Genipin was also investigated as a potential crosslinker after printing the 3D scaffold. Genipin was able to create a more thermally stable scaffold relative to EDC/NHC crosslinking. However, both EDC/NHS and genipin crosslinkers created a scaffold that could survive thermal conditions in the body.

Both EDC/NHS and genipin were investigated as potential agents to crosslink AuNPs to the 3D scaffolds. AuNPs were able to be visualized on the surface of the 3D scaffolds through SEM analysis. The SEM micrographs provide evidence that EDC/NHS may have induced more clumping of the AuNPs on the surface of the 3D scaffold while the use of genipin provided evidence of more homogenous distribution of AuNPs over the 3D scaffold. NAA analysis was also then conducted to determine the mass percent of AuNPs on the 3D scaffolds. Doubling the amount of AuNPs during crosslinking correlated to an approximate

doubling in AuNPs conjugated to the 3D scaffolds in both cases of using EDC/NHS and genipin. Further work could be conducted to determine an approximate limit of conjugation with each concentration of EDC/NHS and genipin. Work with AuNPs has shown their potential as anti-inflammatory agents with a propensity toward cellular migration which are advantageous properties for potential in vivo scaffolds [12, 17, 18].

A 3-day WST-1 cell viability analysis was performed on the 3D printed collagen scaffolds that were crosslinked with EDC/NHS and genipin and conjugated with AuNPs. It was apparent that the cells were viable on the 3D printed scaffolds and there was a significant increase in cellularity at day 3 compared to the control. The genipin conjugated AuNP scaffolds demonstrated a reduction in the overall viability relative to the uncrosslinked scaffold but still demonstrated high cellularity. The EDC/NHS scaffolds demonstrated a slightly reduced cellular viability relative to cells with no scaffold. It was concluded that genipin demonstrated a more cell-friendly crosslinker, which is in agreement with published literature. Thus, for our experiments, we determined that genipin is favored over the use of EDC/NHS crosslinking for future studies.

A 7-day WST-1 cell viability analysis was also performed only using genipin to crosslink AuNPs to the 3D scaffolds. At this time point, the cells with no scaffold were the most metabolically active. Interestingly all samples crosslinked with genipin had an increased cellular viability relative to the uncrosslinked scaffold with 1x AuNP having the highest overall viability among

groups with a scaffold. Comparing these results with the 3-day results, over a longer-term study the genipin-AuNP scaffolds were favorable.

A 24-hour ROS assay assessing the intracellular ROS production was performed to determine if the use of known anti-inflammatory agents genipin and AuNPs could indeed reduce ROS production 24 hours after the addition of the scaffolds to the cells [16, 20, 21, 26]. Our results demonstrated that the genipin-AuNP scaffold has an increase in fluorescent intensity which directly correlates to an increased ROS production. These results conflict with other publications [16, 20, 21, 26]. The use of genipin enhanced ROS production and the conjugation of AuNPs to the scaffolds further enhanced ROS production relative to the uncrosslinked scaffold. It was expected that some amount of ROS would be produced by introducing a foreign 3D scaffold, but overall ROS was reduced with the introduction of the uncrosslinked scaffold relative to the cells with no scaffold. These results conflict with many other reports. It is possible that the remnants of the scaffold could have affected the fluorescent intensity results observed. More than likely, genipin's fluorescent excitation and emission are 510-560 nm and 590 nm respectively which could interfere with the ROS assay which is fluorescent based. Future studies would have to utilize a non-fluorescence based assay or fluorescent assays not within genipin's range to interfere with the results.

Printing in an agarose microparticle solution has the advantage of achieving enhanced reproducibility and 3D scaffold resolution [23]. The drawbacks incurred while printing our collagen solution into the agarose

microparticles were remnant agarose left on the scaffolds after washing which resulted in poor cellular adherence. There have been previous published reports that demonstrated low attachment of cells to agarose [27, 28]. Washing of the 3D printed scaffolds needs to be further investigated in order to efficiently remove remnant agarose left on the surface of the 3D printed scaffolds. The use of printing in an agarose microparticle solution has many advantages especially in reproducibility which necessitates further investigation of washing.

The seeding of stromal cells onto a 3D printed scaffold could lay the groundwork for tissue engineering of various functional in vitro organs. Song et al. developed a method of uterine horn regeneration in a rat model utilizing a collagen scaffold seeded with stomal cells [29]. Initial work was performed with stromal cells to determine if the 3D printed collagen scaffolds could remain structurally viable for long term use with stromal cells. Initially uncrosslinked 3D scaffolds were seeded with stromal cells and were observed after 9 days of incubation. At 9 days the stromal cells appeared to degrade the scaffold and appeared to prefer the bottom of the well plate. A revised scaffold was subsequently tested. The revised scaffold was crosslinked with genipin along with addition of laminin maintain the structural integrity and help adherence of the stromal cells on the scaffold. After 16 days, the samples crosslinked with genipin remained structurally viable and cells appeared to form a homogenous layer over the surface of the scaffold.

In conclusion, we demonstrated the ability to 3D print liquid collagen into structural tissue scaffolds. These scaffolds can be crosslinked and conjugated

with AuNPs. The resulting scaffolds appear to be stable and have cellular viability leading to the possibility of developing a plethora of different tissue engineered structures.

8.5 Acknowledgements

I would like to thank Chris Glover for performing the DSC, NAA, SEM, and 3-day cell viability studies. I would like to also thank Harriet Fitzgerald for culturing and imaging the 3D printed scaffolds with the stromal cells. Finally, I would like to thank Kylie Dahlgren and Mark Messler for their work on developing a structurally stable scaffold for stromal cell culture.

8.6 References

1. Uzman, A., *Molecular Cell Biology (4th edition) Harvey Lodish, Arnold Berk, S. Lawrence Zipursky, Paul Matsudaira, David Baltimore and James Darnell; Freeman & Co., New York, NY, 2000, 1084 pp., list price $102.25, ISBN 0-7167-3136-3.* Biochemistry and Molecular Biology Education, 2001. **29**(3): p. 126-128.

2. Glowacki, J. and S. Mizuno, *Collagen scaffolds for tissue engineering.* Biopolymers, 2008. **89**(5): p. 338-344.

3. Lin, K., et al., *Advanced Collagen-Based Biomaterials for Regenerative Biomedicine.* Advanced Functional Materials, 2019. **29**(3): p. 1804943.

4. Gould, L.J., *Topical collagen-based biomaterials for chronic wounds: rationale and clinical application.* Advances in wound care, 2016. **5**(1): p. 19-31.

5. Wahyudi, H., et al., *Targeting collagen for diagnostic imaging and therapeutic delivery.* Journal of Controlled Release, 2016. **240**: p. 323-331.

6. Lode, A., et al., *Additive manufacturing of collagen scaffolds by three-dimensional plotting of highly viscous dispersions.* Biofabrication, 2016. **8**(1): p. 015015.

7. Pacak, C.A., A.A. MacKay, and D.B. Cowan, *An improved method for the preparation of type I collagen from skin.* JoVE (Journal of Visualized Experiments), 2014(83): p. e51011.

8. Pacak, C.A., J.M. Powers, and D.B. Cowan, *Ultrarapid purification of collagen type I for tissue engineering applications.* Tissue Engineering Part C: Methods, 2011. **17**(9): p. 879-885.

9. Marques, C., et al., *Collagen-based bioinks for hard tissue engineering applications: a comprehensive review.* Journal of Materials Science: Materials in Medicine, 2019. **30**(3): p. 1-12.

10. Kim, Y.B., H. Lee, and G.H. Kim, *Strategy to achieve highly porous/biocompatible macroscale cell blocks, using a collagen/genipin-bioink and an optimal 3D printing process.* ACS applied materials & interfaces, 2016. **8**(47): p. 32230-32240.

11. Filardo, G., et al., *Patient-specific meniscus prototype based on 3D bioprinting of human cell-laden scaffold.* Bone & joint research, 2019. **8**(2): p. 101-106.

12. Smith, S.E., et al., *Homogenized porcine extracellular matrix derived injectable tissue construct with gold nanoparticles for musculoskeletal tissue engineering applications.* Journal of Biomaterials and Nanobiotechnology, 2017. **8**(02): p. 125.

13. Bax, D.V., et al., *Fundamental insight into the effect of carbodiimide crosslinking on cellular recognition of collagen-based scaffolds.* Acta Biomaterialia, 2017. **49**: p. 218-234.

14. Yoo, J.S., et al., *Study on genipin: a new alternative natural crosslinking agent for fixing heterograft tissue.* The Korean journal of thoracic and cardiovascular surgery, 2011. **44**(3): p. 197.

15. Koo, H.-J., et al., *Anti-inflammatory evaluation of gardenia extract, geniposide and genipin.* Journal of ethnopharmacology, 2006. **103**(3): p. 496-500.

16. Nam, K.N., et al., *Genipin inhibits the inflammatory response of rat brain microglial cells.* International immunopharmacology, 2010. **10**(4): p. 493-499.

17. Cozad, M.J., S.L. Bachman, and S.A. Grant, *Assessment of decellularized porcine diaphragm conjugated with gold nanomaterials as a tissue scaffold for wound healing.* Journal of Biomedical Materials Research Part A, 2011. **99**(3): p. 426-434.

18. Grant, S., et al., *A comparative study of the remodeling and integration of a novel AuNP-tissue scaffold and commercial tissue scaffolds in a porcine model.* Journal of Biomedical Materials Research Part A, 2013. **101**(10): p. 2778-2787.

19. Christenson, E.M., et al., *Nanobiomaterial applications in orthopedics.* Journal of Orthopaedic Research, 2007. **25**(1): p. 11-22.

20. Lima, E., et al., *Gold nanoparticles as efficient antimicrobial agents for Escherichia coli and Salmonella typhi.* Chemistry Central Journal, 2013. **7**(1): p. 11.

21. BarathManiKanth, S., et al., *Anti-oxidant effect of gold nanoparticles restrains hyperglycemic conditions in diabetic mice.* Journal of nanobiotechnology, 2010. **8**(1): p. 16.

22. Devore, D., et al., *Development and characterization of a rapid polymerizing collagen for soft tissue augmentation.* Journal of Biomedical Materials Research Part A, 2016. **104**(3): p. 758-767.

23. Senior, J.J., et al., *Fabrication of Complex Hydrogel Structures Using Suspended Layer Additive Manufacturing (SLAM).* Advanced Functional Materials, 2019. **29**(49): p. 1904845.

24. Deeken, C., et al., *Assessment of the biocompatibility of two novel, bionanocomposite scaffolds in a rodent model.* Journal of Biomedical Materials Research Part B: Applied Biomaterials, 2011. **96**(2): p. 351-359.

25. Fitzgerald, H.C., et al., *Self-renewing endometrial epithelial organoids of the human uterus.* Proceedings of the National Academy of Sciences, 2019. **116**(46): p. 23132-23142.

26. Hughes, R.H., et al., *Neuroprotection by genipin against reactive oxygen and reactive nitrogen species-mediated injury in organotypic hippocampal slice cultures.* Brain research, 2014. **1543**: p. 308-314.

27. Thomsen, A.R., et al., *A deep conical agarose microwell array for adhesion independent three-dimensional cell culture and dynamic volume measurement.* Lab on a chip, 2018. **18**(1): p. 179-189.

28. Carlsson, J., et al., *Protein-coated agarose surfaces for attachment of cells.* In vitro, 1979. **15**(11): p. 844-850.

29. Song, T., et al., *Regeneration of uterine horns in rats using collagen scaffolds loaded with human embryonic stem cell-derived endometrium-like cells.* Tissue Engineering Part A, 2015. **21**(1-2): p. 353-361.

Chapter Nine

FUTURE WORK

9.1 Future work

Posttraumatic osteoarthritis (PTOA) is a particular form of osteoarthritis where an acute injury leads to damage of the articular cartilage, subchondral bone, affects joint articulation, and can also create joint instability [1]. PTOA is commonly found in young, healthy, and typically more active patients due to PTOA occurring from factors like a meniscal tear, ACL rupture, ankle instability, shoulder dislocation, and patellar dislocation [2]. As of 2005, PTOA comes at a cost of $3 billion annually [3]. The work presented in this dissertation demonstrates a unique method to fabricate a liquid collagen solution that can easily fibrilize under increased thermal conditions or when immersed in ionic solutions. The liquid collagen was found to be useful for the fabrication of Collagen Microspheres (CM). The CMs have the potential to be an injectable material for mitigating the progression of PTOA and may have applications in tissue regeneration. The liquid collagen also has valuable applications in additive manufacturing techniques for the development of collagen-based scaffolds.

Initial studies examining ROS mitigating potential of curcumin loaded targeting CMs in IL-1β stimulated chondrocyte cells were performed in this work. Promising results showing a reduction in total ROS with curcumin loaded targeting CMs were obtained. To continue the development of PTOA therapeutic targeting CMs, further *in vitro* investigation of synthesized catabolic factors from

patient-derived osteoarthritic chondrocytes could be investigated. Potential catabolic markers like MMP 1, 2, 3, 8, 9, 13, TNF-α, IL-1β, IL-6, and IL-8 can all be investigated through enzyme-linked immunosorbent (ELISA) assays [4-8]. In vitro analysis of collagen synthesis from chondrocytes is another area of investigation. Increased expression of type I collagen is a characteristic of progression while expression of type II & X collagen is reduced [9, 10]. Chondrocyte apoptosis is another hallmark of the progression of the catabolic events of PTOA [11]. Chondrocyte apoptosis studies determining the chondroprotective ability of the therapeutic targeting CMs would also be useful for analysis.

Ex vivo work with patient-derived PTOA articular cartilage tissue would be pertinent for further investigation in pursuit of in vivo studies with CMs. This would not only provide insightful information on how efficient therapeutic/targeting CMs would be at binding to damaged cartilage but would also be useful in determining chondrocyte viability, apoptosis, membrane damage, matrix degeneration, and collagen deposition. Delco et al. performed work utilizing a method to harvest damaged cartilage to study these various pathologies on bovine articular cartilage which could be modified for human study [12]. The use of ex vivo cartilage would also be of interest to observe the effects of CMs delivering mesenchymal stem cells (MSCs). Prasadam et al. describes a method of harvesting cartilage from knee replacement surgery patients and using the cartilage to develop an *in vivo* cartilage defect model [13]. The harvested cartilage was defected using a dental bur to create a 2 mm

diameter by 2 mm deep hole defect. The defect was filled with bone marrow-derived stem cells and articular cartilage chondrocytes. The defects were then sealed with Matrigel and implanted subcutaneously in mice to determine the effects of cellular addition to the defect. Safranin-O staining, Bern scoring, and immunohistochemical staining (aggrecan, collagen type I, II, &X, VEGF, ChM-1, and MMP-13) were all performed to characterize the performance of the cellular addition of the defect. This technique could be modified for CMs delivering MSCs.

Animal model work should be conducted to determine in vivo effect in animal models. Large animal models such as sheep, goats, or dogs all provide anatomically similar knee joints to humans which provide solid evidence for translation into clinical trials given successful outcomes [14]. Dogs are the most commonly used model to study osteoarthritis with their ease of osteoarthritis development spontaneously among other successful inductions like ACL transection, meniscal release, and focal cartilage defect [15, 16]. The most clinically applicable scenario for use of therapeutic/targeting CMs may be in the case of focal cartilage defect models. Cartilage defects like these can arise from such events like car accidents or sporting injuries [17]. A defined event occurs leading to immediately sought out treatment. In a direct cartilage defect model by Frost-Christensen et al., grooves are cut into the articular cartilage on the lateral and medial femoral condyles at a depth of 0.5 mm [18]. Radiological evaluation, gait analysis, cartilage integrity was evaluated through macroscopic scoring, histologic scoring, and proteoglycan content. Chondrocyte activity was

determined by proteoglycan synthesis rate, and proteoglycan release. Synovial inflammation were assessed by macroscopic scoring and histologic scoring [18].

In conclusion, this dissertation has described the early-stage work towards the fabrication of biomaterials suitable for *in vivo* evaluation. Characterization and optimization of injectable homogenized extracellular matrix constructs, electrospun PCL/lecithin scaffolds, CMs, and 3D printed collagen scaffolds were all reported in this work. The fabrication of homogenized extracellular matrix constructs and therapeutic/targeting CMs shows their individual potentials as injectable therapeutics for PTOA applications. Work on improving PCL/lecithin electrospun scaffolds reproducibility was achieved. Finally, early-stage development of collagen-based additive manufacturing 3D printing was conducted with evidence provided for scaffolds integration with fibroblast cells and human stromal cells for potential future work in organ development. More analysis needs to be conducted with respect to each project for direction into *in vivo* evaluations. Each project is at the forefront of biomaterials innovation development and could provide therapeutic treatments for patients in the future.

9.2 References

1. Goldring, M.B. and S.R. Goldring, *Articular cartilage and subchondral bone in the pathogenesis of osteoarthritis.* Annals of the New York Academy of Sciences, 2010. **1192**(1): p. 230-237.

2. Carbone, A. and S. Rodeo, *Review of current understanding of post-traumatic osteoarthritis resulting from sports injuries.* Journal of orthopaedic research, 2017. **35**(3): p. 397-405.

3. Brown, T.D., et al., *Posttraumatic osteoarthritis: A first estimate of incidence, prevalence, and burden of disease.* Journal of Orthopaedic Trauma, 2006. **20**(10): p. 739-744+747-748.

4. Rigoglou, S. and A.G. Papavassiliou, *The NF-κB signalling pathway in osteoarthritis.* The International Journal of Biochemistry & Cell Biology, 2013. **45**(11): p. 2580-2584.

5. Goldring, M.B. and K.B. Marcu, *Cartilage homeostasis in health and rheumatic diseases.* Arthritis Research & Therapy, 2009. **11**(3): p. 224.

6. Sebastian, A., et al., *Comparative Transcriptomics Identifies Novel Genes and Pathways Involved in Post-Traumatic Osteoarthritis Development and Progression.* International journal of molecular sciences, 2018. **19**(9): p. 2657.

7. Ulivi, V., et al., *p38/NF-kB-dependent expression of COX-2 during differentiation and inflammatory response of chondrocytes.* Journal of Cellular Biochemistry, 2008. **104**(4): p. 1393-1406.

8. B Marcu, K., et al., *NF-κB signaling: multiple angles to target OA.* Current drug targets, 2010. **11**(5): p. 599-613.

9. Thomas, N.P., et al., *Attenuation of cartilage pathogenesis in post-traumatic osteoarthritis (PTOA) in mice by blocking the stromal derived factor 1 receptor (CXCR4) with the specific inhibitor, AMD3100.* Journal of Orthopaedic Research, 2015. **33**(7): p. 1071-1078.

10. Blaney Davidson, E., et al., *Correction: Increase in ALK1/ALK5 Ratio as a Cause for Elevated MMP-13 Expression in Osteoarthritis in Humans and Mice*. Vol. 182. 2009. 7937-45.

11. Rai, M.F., et al., *Post-traumatic osteoarthritis in mice following mechanical injury to the synovial joint.* Scientific reports, 2017. **7**(1): p. 1-13.

12. Delco, M.L., et al., *Mitoprotective therapy preserves chondrocyte viability and prevents cartilage degeneration in an ex vivo model of posttraumatic*

osteoarthritis. Journal of Orthopaedic Research®, 2018. **36**(8): p. 2147-2156.

13. Prasadam, I., et al., *Mixed cell therapy of bone marrow-derived mesenchymal stem cells and articular cartilage chondrocytes ameliorates osteoarthritis development.* Laboratory Investigation, 2018. **98**(1): p. 106-116.

14. Garner, B.C., et al., *Using animal models in osteoarthritis biomarker research.* The journal of knee surgery, 2011. **24**(04): p. 251-264.

15. Cook, J., et al., *The OARSI histopathology initiative–recommendations for histological assessments of osteoarthritis in the dog.* Osteoarthritis and cartilage, 2010. **18**: p. S66-S79.

16. Gregory, M.H., et al., *A review of translational animal models for knee osteoarthritis.* Arthritis, 2012. **2012**.

17. Buckwalter, J.A., *Sports, Joint Injury, and Posttraumatic Osteoarthritis.* Journal of Orthopaedic and Sports Physical Therapy, 2003. **33**(10): p. 578-588.

18. Frost-Christensen, L., et al., *Degeneration, inflammation, regeneration, and pain/disability in dogs following destabilization or articular cartilage grooving of the stifle joint.* Osteoarthritis and cartilage, 2008. **16**(11): p. 1327-1335.

VITA

Colten Lawrence Snider was born in Springfield, MO to Gregory Snider and Denise Hancock. He grew up in Rogersville, MO and attended Logan-Rogersville High School. He earned a Bachelor of Science in Bioengineering with an emphasis in Biomedical Engineering at the University of Missouri, Columbia, MO in December of 2015. In the spring of 2016, Colten began his pursuit of a Doctorate of Philosophy with Dr. Sheila Grant in the Bioengineering program. His research interests included naturally derived biomaterials for tissue engineering applications. He also spent one year in graduate school working in the university's technology transfer office where he reviewed patent disclosures in the health science field based on patentability and potential market capture of the technology.